UNIVERSITY OF CALIFORNIA, SAN DIEGO

Development of Multifunctional Nanoparticles Validated by an Intravital Tumor Model

A dissertation submitted in partial satisfaction of the

requirements for the degree Doctor of Philosophy

in

Electrical Engineering (Electronic Circuits and Systems)

by

Ahmet Can Erten

Committee in charge:

Sadik C. Esener, Chair
David Cheresh
Michael J. Heller
Yu-hwa Lo
Milan Makale
Robert Mattrey

2010

The Dissertation of Ahmet Can Erten is approved, and it is acceptable in quality and form for publication on microfilm and electronically:

_____

_____

_____

_____

_____

_____

Chair

University of California, San Diego

2010

DEDICATION

To those who will change the odds against cancer.

EPIGRAPH

ON LIVING

I

Living is no laughing matter:
you must live with great seriousness
like a squirrel, for example--
I mean without looking for something beyond and above living,
I mean living must be your whole occupation.
Living is no laughing matter:
you must take it seriously,
so much so and to such a degree
that, for example, your hands tied behind your back,
your back to the wall,
or else in a laboratory
in your white coat and safety glasses,
you can die for people--
even for people whose faces you've never seen,
even though you know living
is the most real, the most beautiful thing.
I mean, you must take living so seriously
that even at seventy, for example, you'll plant olive trees--
and not for your children, either,
but because although you fear death you don't believe it,
because living, I mean, weighs heavier.

1947

Nazim Hikmet

Translated by Randy Blasing and Mutlu Konuk (1993)

TABLE OF CONTENTS

LIST OF TABLES

LIST OF FIGURES

ACKNOWLEDGEMENTS

I would like to express my gratitude to my advisor, Prof. Sadik Esener, for his mentorship and guidance during my Ph.D. years. Prof. Esener presented me with unique opportunities as part of a multi-disciplinary research group at NanoTumor Center for tackling challenging problems of cancer therapy and finding my passion by exploring diverse fields, from nanotechnology to chemistry. I am also grateful for the opportunity to share bench space and collaborate with very bright people, which made this work possible.

I am also indebted to Dr. Milan Makale for his mentorship, guidance and support during my Ph.D. years. Dr. Makale's extensive experience in window chamber models and his guidance was invaluable in the realization of a new window chamber suitable for multimodal imaging as well as on the development of liposomal platforms. I deeply appreciate Dr. Makale's investment in me and will fondly remember my collaboration with him.

I also wish to thank Dr. Wolf Wrasidlo and Dr. Dmitri Simberg for their technical guidance, valuable feedbacks and especially their patience during my introduction to wet lab experiments. Dr. Wrasidlo's broad experience in medicinal chemistry and Dr. Simberg's expansive experience in membranes was instrumental in the development of liposomal platforms presented in this dissertation.

I also owe thanks to Prof. Robert Mattrey for his patience, support and technical guidance for the development of window chamber. Dr. Mattrey's feedbacks

based on his rich experience in MRI and ultrasound enabled me to realize a new window chamber suitable for multimodal imaging. I am also thankful to Mark Bydder and Olivier Girard for their help on the development of window chamber variant.

I would like to thank Prof. Yu-Hwa Lo, for his generosity for letting me access his lab while we were setting up our own microfluidics lab.

I would also like to express my appreciation to all committee members – Prof. Esener, Prof. Lo, Prof. Heller, Prof. Cheresh, Prof. Mattrey and Dr. Makale for taking the time to serve on my committee and for their technical feedback and advice.

I wish to thank some of my colleagues from the Esener research group. I closely worked with Michael Benchimol on microfluidic aspects of developing microbubble based theranostic platforms. His creativity and valuable discussions with him was invaluable to this work. I also closely collaborated with Inanc Ortac on developing PCR on lab-on-a-chip platform and I will always fondly remember my time spent working with him. Carolyn Schutt collaborated on the cell studies portions of my research, providing the macrophages as well as helpful technical insights and dinosaur muffins. I would also like to thank my colleagues Randy Chen and Sung Hwan Cho from Dr. Lo's research group for their friendship and valuable insights. I also thank Corbin Clawson, Mark Hsu, Suayb Arslan, Halil Basturk and Sergio Sandoval for their friendship and uplifting my spirit during my Ph.D. years. I wish them the best of luck on their future endeavors. I thank Mr. Ronnielo Pait for the administrative support, and for helping get supplies on time for the various experiments.

I thank Dr. Xuekun Lu for helping me get started on the cryogenic etching techniques. His expertise on nanofabrication and valuable insights was invaluable in the development of silicon nozzles. I also thank Nano3 staff, especially Larry Grissom, Ryan Anderson and Sean Parks for their patience during my trainings and their technical support for various instruments. Last but not least, I would like to thank Dr. Bernd Fruhberger for his assistance during the development of silicon nozzles.

Chapter 2 and Chapter 4, in part are a reprint of the material presented in: A. Erten, W. Wrasidlo, M. Scadeng, S. Esener, R. Hoffman, M. Bouvet and M. Makale, "Magnetic resonance and fluorescence imaging of doxorubicin-loaded nanoparticles using a novel in vivo model", submitted to Nanomedicine: Nanotechnology, Biology and Medicine. The dissertation/thesis author was the primary investigator and author of this paper.

VITA

2003	B. Sc. in Electrical Engineering, University of Southern California, Los Angeles, CA.
2005	M. Sc. in Electrical Engineering, University of California San Diego, La Jolla, CA.
2010	Ph.D., Electrical and Computer Engineering, University of California San Diego, La Jolla, CA.

PUBLICATIONS

A. Erten, X. Lu, S. Esener, "Fabrication of Silicon-SU8 Nozzles Using Cryogenic Deep Reactive Ion Etching" in preperation.

A. Erten, X. Lu, V. Serra, S. Esener, "Large-scale Monodisperse Micro Emulsion Fabrication via Silicon-SU8 Nozzles" in preperation.

A. Erten, D. Hall, C. Hoh, H. Cao, S. Kushual, S. Esener, R. Hoffman, M. Bouvet, S. Kesari, M. Makale, "Enhancing MRI Tumor Detection with Fluorescence Intensity and Lifetime Imaging", Journal of Biomedical Optics, 2010.

A. Erten, W. Wrasidlo, M. Scadeng, S. Esener, R. Hoffman, M. Bouvet, M. Makale, "Magnetic Resonance and Fluorescence Imaging of Doxorubicin-loaded Nanoparticles

Using a Novel In Vivo Model", Nanomedicine: Nanotechnology, Biology and Medicine, 2010.

C. H. Chen, S. H. Cho, F. Tsai, A. Erten, Y. H. Lo, "Microfluidic Cell Sorter with Integrated Piezoelectric Actuator", Biomedical Microdevices, vol. 11, no. 6, 2009.

O. Girard, A. Erten, M. Bydder, M. Makale, D. Cheresh, D. Gilderdale, R. Mattery "MRI Tissue Window Chamber System for Validation and Optimization of Dynamic Contrast Enhanced Tumor Imaging", *ISMRM*, Hawaii, 2009.

O. Girard, A. Erten, M. Bydder, M. Makale, D. Cheresh, S. Esener, R. Mattrey "Dual MR and Optical Imaging of Tumors to Support Molecular Imaging", *World Molecular Imaging Congress*, Montreal, Canada, 2009.

ABSTRACT OF THE DISSERTATION

Development of Multifunctional Nanoparticles Validated by an Intravital Tumor Model

by

Ahmet Can Erten

Doctor of Philosophy in

Electrical Engineering (Electronic Circuits and Systems)

University of California, San Diego, 2010

Professor Sadik C. Esener, Chair

Cancer is a major public health problem, and although significant therapeutic advances have been achieved for some types of malignancy, many tumors are still challenging to treat. The main therapeutic obstacles include tumor cell resistance to standard chemo-radiotherapy at clinically feasible doses, and treatment effects that are limiting due to normal tissue toxicity. Despite research spanning several decades, the goal of specifically destroying tumor cells, while sparing normal tissues, has remained difficult to attain. Recently however, the growth of the nanotechnology field offers new strategies and is promising in terms of early detection and the targeted therapy of

cancer. Separate nanoparticles can carry a drug payload, can be targeted to tumors, and can be bound to MRI and CT contrast agents. A recent concept is that of "theranostics", viz., the ability of one nanoplatform to integrate several functions so that these are co-localized. For instance, the imaging enhancement property can be used in conjunction with drug delivery for real-time monitoring of drug distribution and to follow the therapeutic effects. Moreover, imaging capability may facilitate activation of a pro-drug payload at an optimum time, for example at the point of maximum nanoplatform accumulation at the tumor. This dissertation describes the design, fabrication and testing of two novel multifunctional nanoplatforms; a liposome containing dextran hydrogel and iron oxide, and a liposome containing perfluorocarbon (PFC) gas microbubble.

A key limitation of nanoengineering in medicine is the lack of practical *in vivo* models, so that many nanoplatforms, while creatively engineered, are not biologically useful. This dissertation discusses and presents the development of an *in vivo* test-bed that allows optical and MRI imaging of nanoplatforms within a tumor and its blood vessels, and is a versatile system for guiding nanovehicle design.

1 INTRODUCTION

1.1 Cancer: The clinical problem

The Greek physician-scientist Hippocrates at around 400 BC named the tumor growths he observed in his patients "karkinos" or "the crab" because, according to Paul of Aegina, this disease "has the veins stretched on all sides as the animal crab has its feet, whence it derives its name"[1]. While Hippocrates only described outwardly visible tumors on the skin, nose and breasts, today according to American Cancer Society, cancer is defined as a group of diseases characterized by uncontrolled growth and spread of abnormal cells which can result in death if the spread is not controlled in time[2].

Currently, cancer is a massive public health problem and accounts for around one in every eight deaths worldwide[2]. Moreover, the World Health Organization projects that in 2010, cancer will surpass heart disease and stroke as the leading cause of death. According to the International Agency for Research on Cancer (IARC), for the year 2008, worldwide there were an estimated 12.4 million new cases of cancer diagnosed, 7.6 million deaths from cancer and 28 million people alive with cancer within five years from initial diagnosis. By the year 2030 cancer will account for about 17.0 million deaths and there will be 26.4 million new cases[2, 3]. Presently, American Cancer Society estimates 1 in 2 American men will develop cancer over his lifetime,

the leading cancer sites being prostate, lung and colon and rectum. Cancer will account for around 1 in 4 deaths among American men. Approximately 1 in 3 American women will develop cancer over her lifetime, the leading sites being breast, lung and colon and rectum and cancer will account for 1 in 5 deaths among American women (Table 1). Furthermore, the overall associated cost of cancer in 2010 is estimated at $263.8 billion: $102.8 billion for direct medical costs; $20.9 billion for loss of productivity due to illness and $140.1 billion for loss of productivity due to premature death by the National Institute of Health (NIH)[2]. Consequently, based on all these figures, cancer is and will be a major threat to public health.

Table 1 The Lifetime Probability of Developing and Dying from Cancer[4]

Site	Males Developing	Males Dying	Females Developing	Females Dying
All Sites	1 in 2	1 in 4	1 in 3	1 in 5
Breast	1 in 149	1 in 204	1 in 8	1 in 34
Colorectal	1 in 19	1 in 46	1 in 20	1 in 49
Lung & bronchus	1 in 13	1 in 16	1 in 16	1 in 21
Melanoma of skin	1 in 37	1 in 213	1 in 56	1 in 427
Non-Hodgkin lymphoma	1 in 44	1 in 111	1 in 52	1 in 132
Ovary	NA	NA	1 in 71	1 in 94
Prostate	1 in 6	1 in 34	NA	NA
Urinary bladder	1 in 26	1 in 117	1 in 84	1 in 296

1.2 Cancer: Challenges and Cancer Nanotechnology

Cancer has proven to be a stubborn foe, as the US, 5-year relative survival rate for all cancers diagnosed between 1999 and 2005 was only 68%, up from 54% between 1984 and 1986, and 50% between 1975 and 1977. This gradual improvement is largely a result of recent progress in diagnosing certain cancers at an earlier stage and improvements in treatment[2]. Currently, the major treatment options include surgery, radiotherapy and chemotherapy. The process of metastasis is largely responsible for the lethality of cancer, is extremely problematical, and confounds the surgical and radiotherapeutic approaches. Current protocols for systemic delivery of chemotherapeutics are seriously constrained in terms of maximum allowable doses of the therapeutic agents, in order to avoid life-threatening systemic toxicity and severe morbidity. However higher dosages of and/or more potent therapeutic agents are necessary to kill tumor cells to compensate for rapid elimination and the non-specific distribution of anticancer chemotherapeutics into organs and tissue[5]. Also, the genetic heterogeneity found between cancers of the same type, between the primary tumor and its metastatic foci, and even between the cells that constitute an individual tumor, together with tumor cell adaptive drug resistance pose significant obstacles in the treatment of cancer[6].

Over several decades a general recognition has evolved that current treatment strategies and agents are inadequate, especially for solid tumors, and the key to controlling cancer is early detection of tumors followed by targeted and localized delivery of the therapeutics. However in order to satisfy these goals new technologies

and paradigms have been needed but were not forthcoming. Recently, with the advent and explosive growth of the field of nanotechnology there is finally considerable promise for answering the crucial need for the sensitive early detection, diagnosis, monitoring, and treatment of cancer with minimal toxicity[6]. Cancer nanotechnology most commonly refers to injectable self-contained structures that are several hundred nanometers or less in size[5, 7]. Compared to conventional therapeutics, these targeted multifunctional nanoplatforms have several potential advantages for cancer therapy [5, 8, 9]:

1. The nanoplatform, which can itself have therapeutic and/or diagnostic properties, can carry an additional payload such as complementary drug or enzyme.
2. The payload does not affect the overall properties of the nanoplatform and do not participate in the control over pharmacokinetics and biodistribution.
3. Multiple chemotherapeutic and contrast agents can be accommodated as payload for combinatorial cancer therapy. Nanoplatforms can carry water insoluble therapeutic agents without toxic organic solvents.
4. Nanoplatforms can carry water insoluble therapeutic agents without toxic organic solvents.
5. Given the large surface area to volume ratio, the nanoplatforms can contain multiple targeting ligands which yield high affinity and specificity for target cells.

6. The nanoplatform can bypass multidrug resistance mechanisms that involve surface protein pumps.
7. Nanoplatforms that are sized to avoid accumulation in organs can nonetheless accumulate preferentially in tumors due to the enhanced permeation and retention (EPR) effect. Rapid and defected angiogenesis of tumors result in highly permeable blood vessels and dysfunctional lymphatic drainage helps the retention.

A controlled combination of these potential advantages of nanoplatforms can significantly improve drug efficacy and potentially overcome drug resistance while reducing systemic toxicity[9].

1.3 Theranostic Nanoplatforms for Cancer Nanotechnology

A wide variety of nanoplatforms are currently under development for application in cancer nanotechnology. These multifunctional structures are engineered to enable incorporation of a wide variety of chemotherapeutic agents and targeted delivery of these agents to the tumor site. Moreover, many nanoplatforms are being developed for improved diagnostic imaging of a variety of cancer types. Recently, the potential of cancer nanotechnology has become more evident with several examples of first generation nanocarriers approved by the FDA such as Abraxane[10],an albumin-bound nanoparticle of paclitaxel; Doxil[11], a liposomal formulation of doxorubicin;

Daunoxome[12], a liposomal formulation of daunorubicin citrate and Feridex[13] dextran coated SPIO (super paramagnetic iron oxide).

Imaging and therapeutic nanoplatforms have been independently used in humans, but in order to image and control events in a coordinated and effective manner it is necessary to co-localize imaging and therapeutics. Hence a unique subset of nanoplatforms called "theranostics" designed to do both imaging and therapeutic functions are the next most likely path for clinical applications[14]. For instance, the imaging enhancement property can be used in conjunction with drug delivery for real-time monitoring of drug distribution as well as to follow the therapeutic effects. This is especially important for cancer therapy as subtherapeutic dosage can cause tumor relapse and might lead to development of drug resistance[15]. Moreover, the accumulation kinetics of multifunctional nanoplatforms at a tumor may facilitate the clinical determination of the optimum time at which to activate a pro-drug by another nanoparticle, magnetic field, light energy, heat or ultrasound.

The most relevant nanoplatforms that can be functionalized with a targeting moiety, therapeutic and contrast agent include drug conjugates and complexes, dendrimers, vesicles, micelles, core-shell structures, microbubbles and carbon nanotubes (Figure 1). Theranostic nanoplatforms can be classified based on their core nanomaterial with theranostic potential including iron oxide based, quantum dot based, gold nanoparticle based and microbubble based.

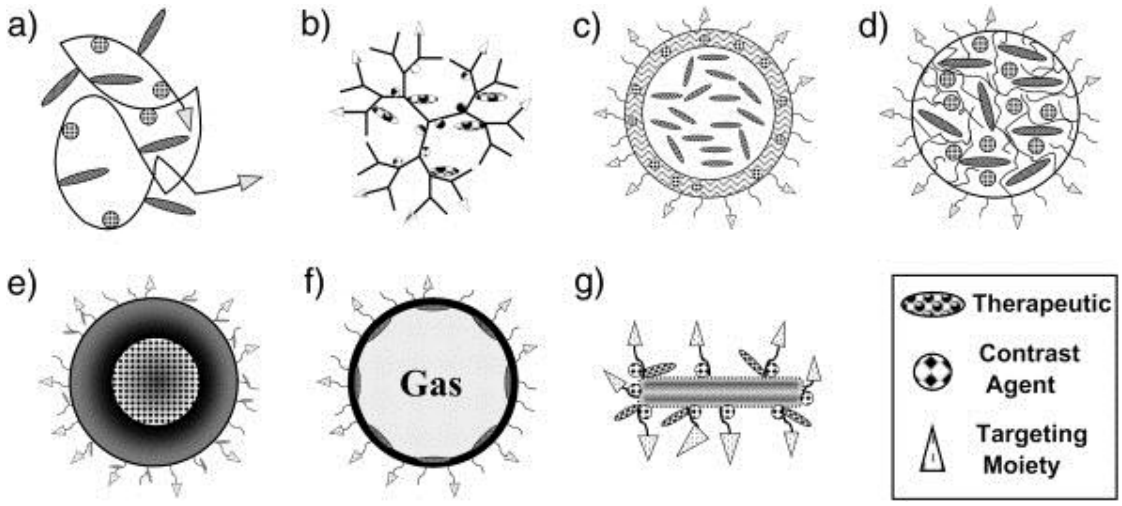

Figure 1 Structural representations of theranostic nanoplatforms

Schematics of a functionalized **a)** drug conjugate; **b)** dendrimer; **c)** vesicle; **d)** micelle; **e)** core-shell nanoparticle; **f)** microbubble; and **g)** carbon nanotube.

1.3.1 Iron Oxide Based Theranostic Nanoplatforms

Iron oxide nanoparticles have become the material of choice in many bioapplications for their biocompatibility, inexpensiveness and super paramagnetic properties. In particular, due to their magnetic properties they can be visualized in MRI, guided to target site by an external magnetic field and heated to provide hyperthermia for cancer therapy[16]. Traditionally super paramagnetic iron oxides (SPIOs) are made in aqueous solution by co-precipitating Fe (II) and Fe (III) precursors[17, 18] and typically hydrophilic polymers are added during the particle formation process to prevent particle aggregation and render SPIOs hydrophilic with dextran and its derivatives being the most studied. In fact, a number of dextran-SPIO

formulations are already approved as MRI contrast agents such as Feridex[19] particles and a number of them entered clinical trials such as Combidex[20]. Recently, pyrolysis synthesis in organic solvent has emerged as a useful strategy in nanoparticle preparation as well.

One group of SPIO based theranostic agents are prepared using covalent chemistry by coupling appropriately coated SPIOs with drug molecules such as methotrexate (MTX)[21] and paclitaxel (PTX)[22]. Similarly, bifunctional PEG polymer coated SPIOs functionalized with chlorotoxin (CTX), a peptide with high affinity for a variety of tumors as well as ability to inhibit tumor invasion, and Cy5.5, near-infrared fluorescing molecule, were developed[23]. The feasibility of conjugating aminated SPIOs by MTX was demonstrated and in vitro studies revealed that the particles were accumulated in the lysosomes, where the drug molecules are released due to cleavage of the amide bond at low pH and protease activity, after they were internalized into the cells[25]. Recently, siRNA delivery with aminated dextran coated SPIO based theranostic agents was also demonstrated[28, 29]. Moreover, these aminated dextran coatead SPIOs were also labeled with near-infrared dye and were modified with a membrane translocation peptide for intracellular delivery[29]. This approach requires the development of complex conjugation chemistries, which often results in limited drug association and quite rapid dissociation[31]. Besides, the associated drug might alter the biodistribution and imaging characteristics of the nanoplatform.

Aside from covalent coupling, SPIO based theranostic agents are prepared by coencapsulating drug molecules such as DOX and PTX with SPIOs into polymeric

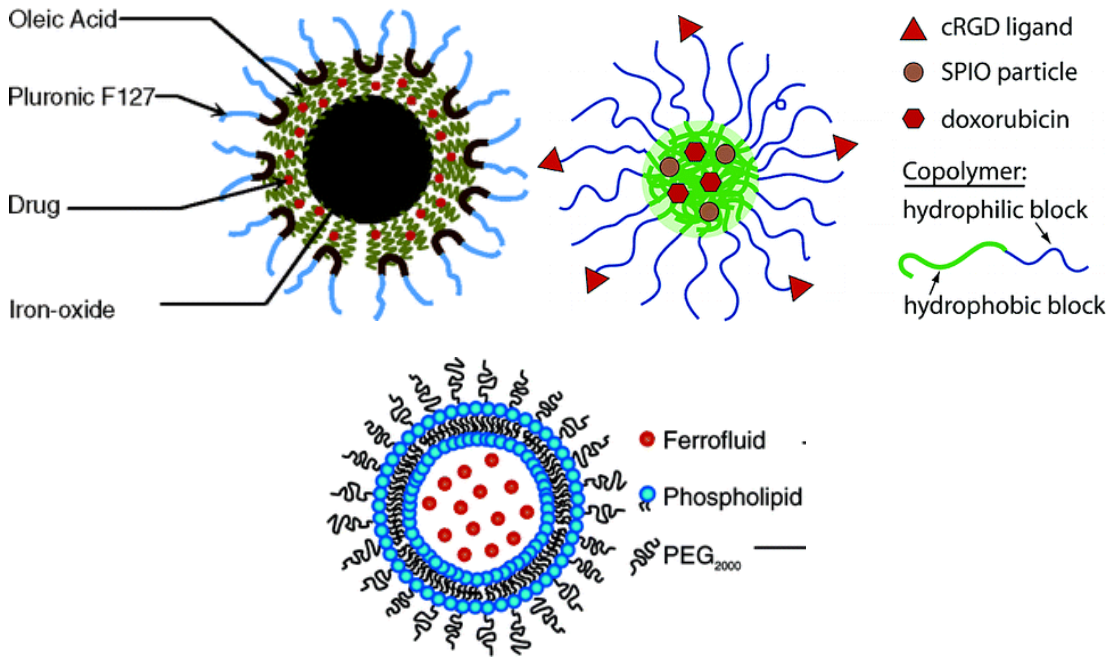

Figure 2 Cartoon showing structures of some Iron Oxide Based Theragnostic Agents.

a) Water-Dispersible Oleic Acid-Pluronic Coated Iron Oxide Magnetic Particle[24, 25]: SPIOs are coated with oleic acid and stabilized by pluronic F-127 and hydrophobic drug molecules are partitioned into oleic acid layer. **b)** Multifunctional Polymeric Micelles as Cancer-Targeted, MRI-Ultrasensitive Drug Delivery Systems[26] : SPIO nanoparticles and DOX are loaded inside the hydrophobic core of micelles with cRGD ligand attached for targeted delivery. **c)** Superparamagnetic Liposomes[27] : Aqueous solution of SPIO crystals and therapeutics are encapsulated within the large unilamellar vesicles.

matrices[16, 24, 25, 32, 33] through non-covalent hydrophobic/hydrophilic and electrostatic interactions. Iron oxide cores coated with oleic acid and stabilized by pluronic F-127 were loaded with PTX and DOX by partitioning into the oleic acid layer[24, 25, 33] (Figure 2). Similarly, carboxyl bearing thermally cross-linked SPIOs were loaded with DOX through electrostatic interactions[25, 34]. Polymeric micelles co-encapsulating SPIO and

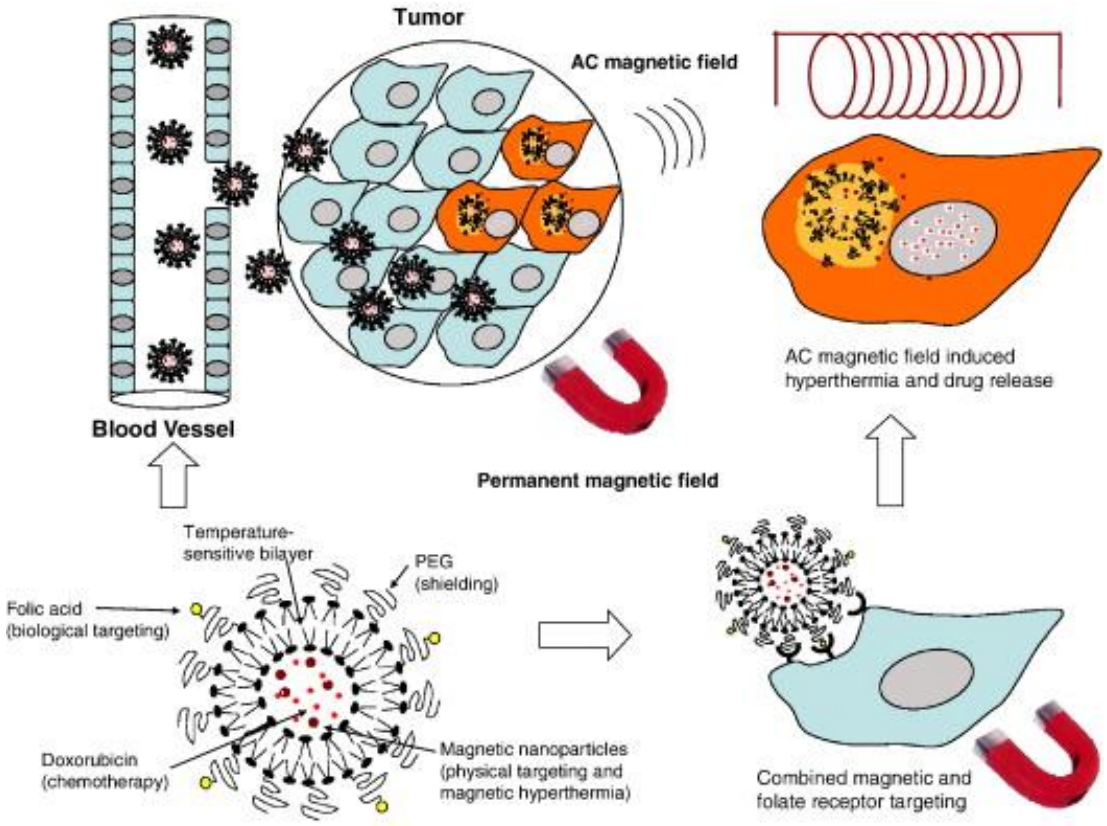

Figure 3 Targeted Temperature Sensitive Magnetic Liposome Carrying DOX[30]

The multifunctional temperature sensitive magnetic liposome can be targeted physically by external magnetic field and biologically by folic acid to tumor cells. Drug release can be triggered by hyperthermia upon local application of an alternating magnetic field (AMF) on the tumor tissue.

DOX with active targeting cRGD ligands attached were also demonstrated[26] (Figure 2). Using similar principles, liposomal iron oxide based theranostic agents were also developed[17, 35, 36]. As a platform, liposomes can incorporate particles and molecules with different functionalities without significantly compromising their stability in the body, which makes them suitable nanoparticles for theranostics.

Another group of SPIO based theranostic agents are prepared by loading porous nanostructures via physical absorption such as Cisplatin loaded hollow SPIOs[37]. Besides their imaging functionality, the magnetic properties of SPIO based theranostic agents also allow them to be accumulated at the target site via application of external magnetic field[38]. Moreover, their potential in hyperthermia in an external alternating magnetic field was exploited in tumor therapy for tumor cells that are more susceptible to elevated temperatures than normal cells[39, 40]. A recent approach demonstrated the feasibility of thermo-chemotherapy using temperature sensitive magnetic liposomes[30]. Temperature sensitive liposomes carrying DOX can be targeted to the tumor tissue physically by external magnetic field and biologically by folic acid. Once the vesicle reaches the tumor tissue, drug release could be triggered by hyperthermia upon local application of an alternating magnetic field (AMF) on the tumor tissue as shown in Figure 3.

In summary, iron oxide based theranostic agents have been receiving a lot of attention due to their unique magnetic properties and the associated imaging and therapeutic applications. However, in general long term in vivo data on pharmacokinetics of these novel theranostic formulations are lacking in the field which needs to be addressed.

1.3.2 Quantum Dot Based Theranostic Nanoplatforms

Quantum dots (QDs) are becoming an important class of biomaterials for their superior optical properties such as being brighter, more photo-stable and having

narrow emission spectra and broad absorption spectra compared to organic dyes and fluorescent proteins. While first generation of QDs was emitting in visible spectrum, the next generation of QDs with emission in infrared spectrum are designed for deeper tissue penetration. Typically, QDs are prepared by appropriate organometallic precursors being heated in high boiling point organic solvents with thiolated species added to confer water solubility.

One group of QD based theranostic agents are prepared by loading QDs via physical adsorption such as MTX loaded QDs[41]. Another group of QD based theranostic agents are prepared by coencapsulation of QDs and drug into lipid micelles such as QD, SPIO and DOX loaded phospholipid micelles[42]. Recently, application of QDs as siRNA delivery vehicles was also demonstrated[43, 44].

Besides their imaging functionality, QDs also have great potential in photodynamic therapy where they act as photosensitizers by transferring triplet state energy to nearby oxygen molecules to cause cell damage when they are activated by light[45]. However, the application of QDs as theranostic agents is greatly limited due to the heavy metal related toxicity issues. For QDs to become a real contender in the field of theranostic agents, the heavy metal related toxicity issues and their metabolism in the body need to be investigated thoroughly.

1.3.3 Gold Nanoparticle Based Theranostic Nanoplatforms

Gold nanoparticles has long been the material of choice for building up agents for both imaging and therapy applications due to their strong surface plasmon

absorption, stability, biocompatibility and ease of modification. Synthesis of gold nanoparticles has been well established and those in the forms of spheres[46], cubes[47], rods[48], cages[48] and wires[49] can now be acquired in large quantity with accurate control on quality and size. Due to strong interaction between thiol and gold, the gold nanoparticle based theranostic nanoplatforms are generally prepared using thiolated species.

One group of gold nanoparticle based theranostic nanoplatforms are prepared by conjugation of PTX to phenol terminated gold nanocrystals[50]. Another group of gold nanoparticle based theranostic nanoplatforms are prepared by coencapsulating gold and drug into polymeric matrices such as DOX loaded into amphiphilic-block-copolymer[51]. Recently, the potential of gold nanoshells as siRNA carriers was also demonstrated[52].

Besides their imaging applications, gold based theranostic nanoplatforms that can absorb in the near infrared region are used in photothermal therapy; gold nanoplatforms concentrated in tumor area convert light into heat and kill adjacent cancerous cells via hyperthermia[53]. However, the high production costs and the stability of thiol-Au chemistry at reducing environments are the major obstacles in front of its wide applicability as a theranostic agent.

1.3.4 Microbubble Based Theranostic Platforms

Colloidal microbubbles are becoming as an important platform as contrast agents for imaging and as carriers for targeted drug delivery with ultrasound being the imaging modality and the external trigger for targeted drug delivery. In general, microbubbles are composed of a gas core stabilized by a shell comprised of proteins, lipids or polymers and are prepared by sonication, which involves the application of high intensity ultrasound to disperse a portion of the perfluorocarbon (PFC) gas within the aqueous phase of the shell constituents. Cartoon of a typical microbubble with different shell compositions is shown in Figure 4 . Typically, the diameter of a microbubble is kept to less than 10 μm for it to display rheology similar to red blood cells in the microvessels and capillaries throughout the body[54].

Microbubbles display a range of behaviors when they are insonified by ultrasound which depend not only on the US parameters but also on the microbubble size and physicochemical properties[55]. Violent effects such as cavitation can be used for active targeted drug delivery - cavitation of bubbles can induce sonoporation, increase in the permeability of an endothelial vasculature, allowing small molecules to enter into tissue from the blood stream - while more subtle effects such as backscattering are used for imaging. A cartoon of some US-mediated effects of microbubbles for biomedical applications is shown in Figure 5.

While there are already FDA approved contrast agents with perfluorocarbon (PFC) gas cores such as Optison, an albumin microbubble formulation and Definity, a phospholipid microbubble formulation, microbubbles with theranostic capabilities are

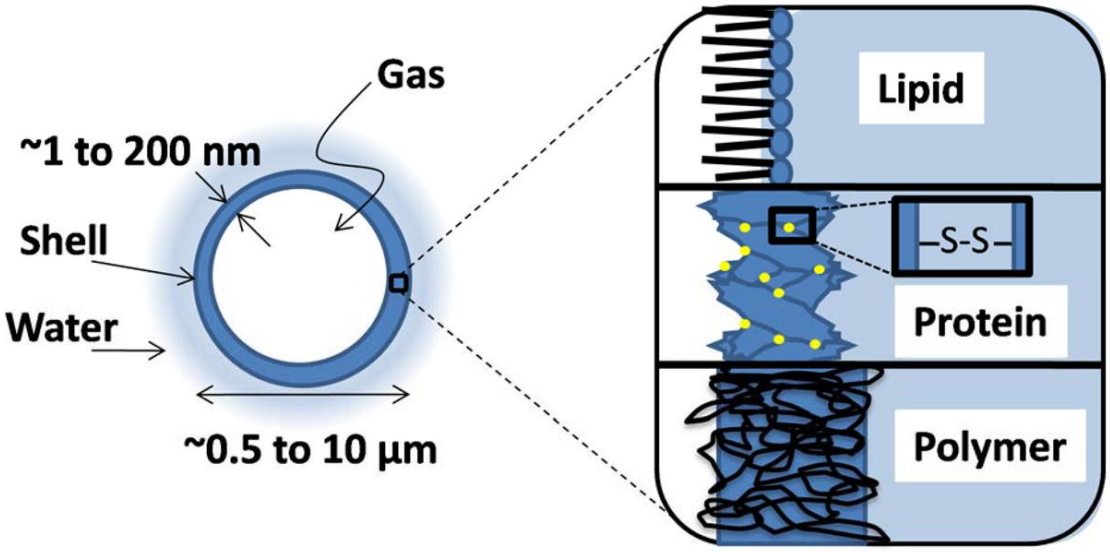

Figure 4 Cartoon showing structure of a typical microbubble with different shell compositions[56].

Microbubbles used for biomedical purposes are typically between 0.5 and 10 µm in diameter (the upper limit for passage through the lung capillaries). The gas core is a single chamber and comprises a large majority of the total particle volume. The shell acts as a barrier between the encapsulated gas and the surrounding aqueous medium. Different shell materials may be used, including lipid (~3 nm thick), protein (15-20 nm thick) and polymer (100-200 nm thick). The lipid molecules are held together through physical force fields, such as hydrophobic and Van der Waals interactions. The protein is cross-linked and/or entangled to form a bulk-like material.

still in development. As a theranostic platform, microbubbles can be activated by external ultrasound as cavitation nuclei for treating vascular thrombosis and drug delivery combined with their active and passive targeting capabilities. Because the gas core is a poor solvent for drug molecules, several loading strategies are employed within or onto the shell to accomplish as shown in Figure 6. Several shell compositions and their effects on theranostic properties of the particles are listed in Table 2.

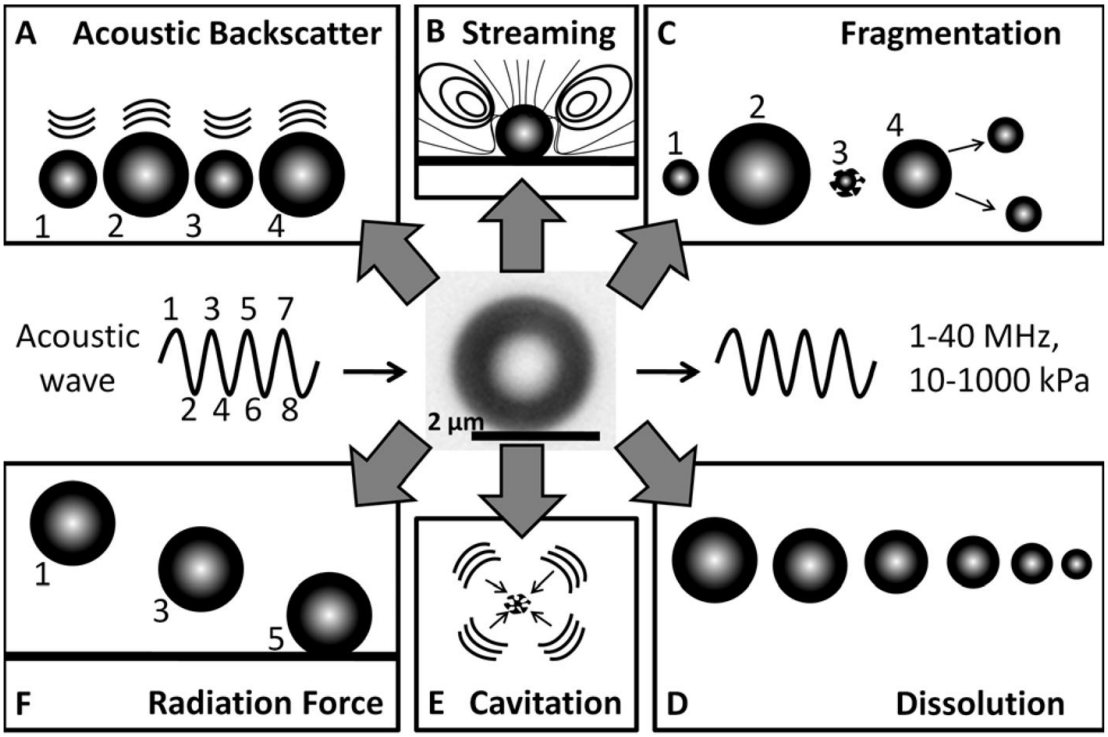

Figure 5 US-mediated effects of microbubbles for biomedical applications[55]

Microbubbles insonified at MHz frequencies produce a variety of effects which may be beneficial for US imaging or drug delivery. **A)** Oscillation of the gas core at moderate pressures produces a detectable backscatter. **B)** Streaming of the fluid around the oscillating microbubble creates shear forces that may facilitate drug release and uptake by nearby cells. **C)** Insonation at high pressures results in microbubble fragmentation. **D)** Insonation at moderate pressures below the fragmentation threshold results in dissolution of the gas core. **E)** Insonation at lower frequencies and higher pressures results in inertial cavitation, which can produce shock waves and involuted jets (water hammer). **F)** Insonation at low pressures near microbubbles resonance results in radiation force, which displaces the microbubble away from transducer.

One group of microbubble based theranostic agents are acoustically active lipospheres (AALs)[57-59]. AALs are similar to microbubbles with lipid shell, but they contain a thick oil layer, for hydrophobic drug molecule loading, separating the lipid shell from the gas core. Cartoon showing structure of a typical AAL is shown in

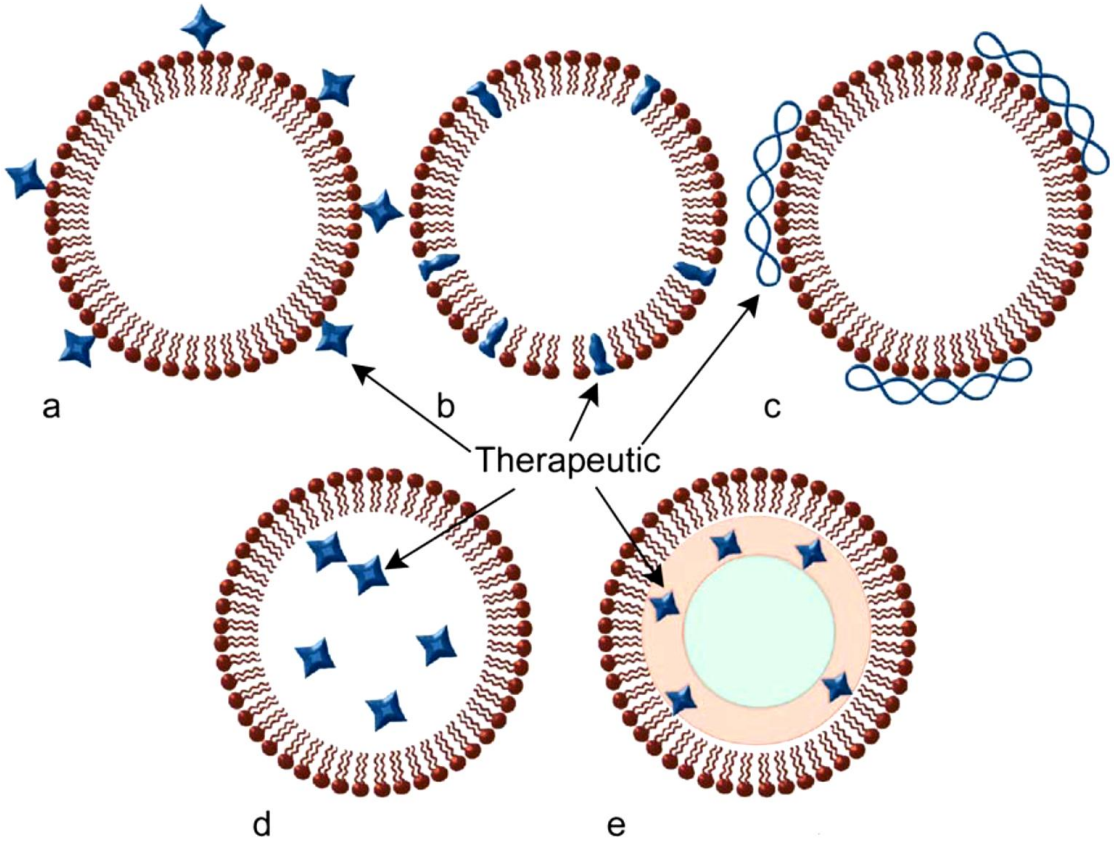

Figure 6 Cartoon showing structure of some microbubble based theranostic agents[60, 61]

Drugs may be **a)** attached to the membrane surrounding the microbubble, **b)** imbedded within the membrane itself, **c)** bound non-covalently to the surface of the microbubbles **d)** coencapsulated with the gas **e)** incorporated into a layer of oily material that forms a film around the gas core (AAL).

Figure 6. First AALs developed for targeted drug delivery applications was loaded with PTX and had a mean diameter of 2.9 μm[57]. A more recent work on AALs included RGD; integrin binding peptide for targeting tumor vasculature, bearing PTX loaded AALs with a mean diameter of 1.4 μm[58]. Another recent study on AALs utilized microfluidic techniques to generate DOX loaded AALs with diameters within 7-20 μm range determined by constituent flow rates[59].

Table 2 Shell compositions, properties and ultrasound effects[55]

Shell Type	Thickness	Compliance	Stability	Drug Payload	US Effects
Protein	15-20 nm	Medium	Medium	Medium	High echogenicity; Shell doesn't reseal after rupture
Lipid	3 nm	High	Low to Medium	Low to Medium	High echogenicity; Shell reseals after rupture
Polymer	100-200 nm	Low	High	High	Low echogenicity; Shell doesn't reseal after rupture

An alternative group of microbubble based theranostic agents utilized liposomes covalently attached to lipid shelled microbubbles using biotin-avidin linker system as drug loading site[62]. 100-200 nm liposomes loaded with fluorescent cholesterol as a model hydrophobic drug are attached to microbubbles with mean diameter of 1.8 μm. Similarly, in 2008, pegylated liposomes containing siRNA were attached to the surface of avidinylated lipid microbubbles using biotin-avidin linker[63].

One group of microbubble based theranostic agents encapsulated the therapeutic agent within the shell using double emulsion preparation. Using this method plasmid DNA was encapsulated within PLGA microbubbles[64, 65]. Another group of microbubble based theranostic agents benefited from adsorption of therapeutic agents to the microbubble shell due to electrostatic and hydrophobic interactions. Using this approach, in 2006, plasmid DNA was bound to albumin

microbubbles coated with cationic polymer poly(allylamine hydrochloride) (PAH)[66]. Similarly, in 2003, plasmid DNA and in 2006 tumor growth suppressing antisense oligodeoxynucleotides was bound to lipid shelled microbubbles having cationic lipids introduced into the shell composition[67, 68]. Another strategy for therapeutic loading has been to incorporate macromolecules within the cross-linked shell during microbubble formation. In a recent study, the feasibility of entrapping plasmid DNA into the albumin shell of microbubbles was demonstrated[69, 70]. Using a similar approach, in the feasibility of entrapping luciferase enzyme into the lipid shell of microbubbles was also demonstrated[71].

Besides their applications in imaging and targeted drug delivery, microbubbles are also used for increasing the effects of high intensity focused ultrasound (HIFU) for hyperthermia and thermo-ablation of cancerous cells. Microbubbles may shorten the HIFU treatment procedure by increasing the rate of heating from HIFU[72].

In summary, microbubble based theranostic agents have great potential in simultaneous active and passive targeted drug delivery and imaging. However, more effective microbubble formulations or loading schemes are needed in order to improve drug carrying capacity and targeted release[55].

1.4 Theranostic Nanoplatforms: Challenges for Moving Forward

Theranostic nanoplatforms are emerging as a strong contender in the field of cancer therapy with their unique capability for simultaneous monitoring and treatment.

However, there are formidable challenges that confront the developers of theranostic nanoplatforms before they can be translated into clinic. These challenges are diverse and they are all in part difficult due to the lack of physiologically relevant test-beds available to designers. It is critical that the engineering of these nanoplatforms be guided by biological considerations if they are to be translated into clinical use. The biological issues are complex and can only be duplicated by an *in vivo* system. Some of the technical challenges in nanoplatform design that could be addressed in a suitable in vivo test-bed include surface opsonization[73], nanoparticle (platform) uptake and retention in reticuloendothelial organs, difficulties in targeting and penetration in solid tumors[74], the long-term fate and toxicity concerns of nanoparticles, especially nonbiodegradable nanomaterials containing toxic elements[75], upscaling, streamlining and standardizing synthesis of nanoparticles; and some of these challenges are unique to theranostic nanoplatforms due to their multifunctional nature such as achieving theranostic effect within the allowable dosage.

Opsonization is the process of nanoparticles becoming covered with nonspecific proteins (opsonins) that might act as binding enhancers for phagocytosis by phagocytic cells such as monocytes, macrophages, neutrophils and dendritic cells. In general, the primary forces for opsonization are the hydrophobic and electrostatic interactions together with conformational changes and associated changes in entropy[76, 77]. After opsonization, phagocytosis can occur. One method that has been developed to reduce opsonization is incorporation of shielding groups such as poly(ethylene glycol) (PEG) and polysaccharide (dextran) to block the electrostatic and hydrophobic

interactions[76, 78, 79]. Recently, it has been shown that the hydrodynamic size is a key factor in predicting the interaction of nanoparticles with plasma proteins and smaller hydrodynamic size reduces the opsonization probability as well[80].

Nanoparticles are usually taken up by the liver, spleen and other parts of reticuloendothelial system (RES) which is part of the immune system that consists of phagocytic cells such as monocytes and macrophages. Surface modification such as PEGylation was shown to reduce the opsonization and as a result minimize the clearance by the RES, resulting in longer blood circulation times and improved pharmacokinetic properties. Amphiphilic polymer chain coatings such as PEG combined with reduced particle size are shown to be the most promising strategies for reducing RES uptake. However, there is no method available for complete avoidance of the RES to escape from eventual uptake.

Nanoparticles can be delivered to tumors by both active and passive targeting mechanisms. In the passive mode, nanoparticles with sizes less than 100 nm often accumulate at the tumors due to EPR effect. In active mode, ligand molecules such as antibodies and peptides are utilized to recognize specific tumor antigens. The accumulation due to EPR effect depends on various factors such as nanoparticle size, the leaky vascular pore size, the blood circulation half-life, the degree of tumor vascularization and the degree of angiogenesis and it has been widely exploited as a targeting scheme[81]. On the other hand, the benefits of active targeting are more controversial and more systematic work involving in vivo experiments is needed in this area.

While a plethora of nanoparticles have been reported with various properties, relatively few have been investigated for in vivo efficacy, toxicity not to mention their long term effects and eventual fate. The toxicity studies of nanoparticles are one of the weakest points of current research. Their unique properties at this scale (mechanical, optical, chemical electrical, magnetic) combined with their composite nature makes it difficult to predict their long term effects based on our knowledge of the interactions between small molecules. Unlike traditional therapy involving molecular therapeutics, the toxicity of not only the composite multifunctional nanoparticles themselves but the secondary products composing the nanoparticles needs to be investigated. Moreover, although advances have been made in some aspects, such as avoiding RES and enhanced site-specific accumulation, greater insight into the mechanisms dictating the fate of nanoparticles especially of non-biodegradable nanoparticles in vivo is needed. Most important, lack of studies including nanoparticle distribution, pharmacokinetics and pharmacodynamics using relevant animal models leads to a gap between the synthetic aspect of nanomaterial design and their potential utility in vivo[82] and even the synthetic aspect of nanomaterial design is hindered by the lack of in vivo studies as the results will be essential in future iterations of future nanomaterial designs.

One immediate dilemma unique to theranostic nanoplatforms is in the formulation of these theranostic nanoplatforms due to the mismatch between doses required for imaging and therapy. For instance, the imaging dose of ^{18}F fluorodeoxyglucose is 05-1 μg/kg bodyweight with a maximum of 9.3 μg/kg and of gadolinium based Magnevist is 100 mg/kg whereas the average therapeutic dose of

DOX is 2 mg/kg[83]. If these were used as payload for a theranostic platform, it wouldn't be possible to deliver therapeutic dose of DOX even at the maximum allowable dose of ^{18}F. One straightforward solution to this problem is using nanoplatforms that are inherently theranostic such as gold nanoshells, which can be detected by optical coherence tomography and can be used for thermo-ablation or SPIOs, which are excellent MRI contrast agents and also can be used for thermo-ablation or microbubbles which can be detected by US and can be used for thermo-ablation as well. Another alternative answer involves careful selection and pairing of therapeutic agents and imaging agents in order to achieve the theranostic effect within the allowable dosage. One further strategy is inclusion of prodrugs, therapeutics that are only active in the presence of certain stimuli such as particular enzymes, light, magnetic field or ultrasound, to further reduce the systemic toxicity and increase specificity.

In summary, a better understanding of desired nanostructure properties, better methods involving relevant in vivo studies to test and validate the new nanoparticles in their development and accepted and established strategies for the efficient translation of new nanostructures into the clinic are necessary for moving forward.

1.5 Dissertation Outline

Following the motivation outlined for cancer nanotechnology and theranostic nanoplatforms in this chapter, the strategy for designing, fabricating and testing of

theranostics based around an *in vivo* model of cancer is discussed. The development and implementation of an in vivo test-bed was deemed necessary because an important limitation in the development of nanoplatforms for cancer is the lack of suitable *in vivo* test systems. Most new nanoplatforms are tested in cell culture, if at all, so that insufficient information is gathered concerning their *in vivo* applicability. The testing of nanoplatforms using orthotopic models in which the animal subjects must be euthanized, dissected, and the tissues subjected to histology is tedious and inefficient, and provides endpoint data only. Such a system does not provide information on the *in vivo* dynamics and kinetics of the nanoplatform. This general scenario in the nano-cancer field results in many design errors and the creation nanoplatforms that are innovative from an engineering perspective, but are not biologically useful.

The model described in this dissertation was adapted for noninvasive serial observation of theranostic agents both optically and using the main imaging modality the theranostic agent is designed for, i.e., MRI or ultrasound. Useful information about the nanoplatform was obtained using this *in vivo* model, and was then used to further modify the nanoparticles which were subsequently retested using the model and then evaluated in orthotopic xenograft models. Apart from the main imaging modality component, viz., deep tissue imaging, all theranostic platforms we sought to develop had an optical marker for preclinical cross-validation. This strategy took advantage of the high sensitivity and subcellular spatial resolution of optical systems to assess different targeting strategies and the pharmacokinetics and pharmacodynamics of the nanoplatform.

In Chapter 2 the dissertation goes on to describe the development of two new, innovative multifunctional nanoplatforms. The first platform is microbubble based and the second is an SPIO based theranostic. The design, preparation and characterization together with the motivation behind the development of these two different theranostic platforms is explained. In Chapter 3, the development and fabrication of an *in vivo model* – MRI compatible rodent dorsal skinfold chamber – and the motivation behind developing this *in vivo* model is presented together with imaging results. Testing was performed on the nanoparticle platform that was deemed the closest to preclinical studies, the SPIO theranostic. In Chapter 4, intravital imaging of theranostic agents (multifunctional nanoplatforms) using both the dorsal skinfold chamber test-bed and orthotopic xenograft models is discussed. The dissertation concludes with a brief summary and an outlook on future research directions stemming from the work described herein.

2 THERANOSTIC PLATFORMS FOR CANCER

2.1 Introduction

Recently, with the development of a variety of highly integrated nanotechnology platforms that incorporate multiple functions such as imaging and therapy, these nanoplatforms including polymer-drug conjugates, liposomes, polymeric micelles, dendrimers, polymersomes and gold, silicon and polymer shells hold considerable promise in early detection and simultaneous monitoring and treatment of cancer with minimal toxicity[6]. The general subsets of integrated nanoplatforms which incorporate combination of therapeutic and diagnostic moieties are also known as theranostic nanoplatforms[6, 84]. From a clinical perspective, theranostic nanoplatforms offer a plethora of advantages compared to traditional treatments including simultaneous diagnosis, monitoring and treatment of disease. They also provide feedback mechanisms for release, biodistribution and efficacy of the incorporated therapeutic agent[84].

This chapter will focus on two different theranostic nanoplatforms. The design rationale for each theranostic, which is based around their potential use in cancer therapy, will be described. The preparation methods used for each type theranostic will be delineated. Finally, the results, problems and limitations with the design and fabrication of each nanoplatform will be addressed.

2.2 Super Paramagnetic Iron Oxide (SPIO) Based Theranostic Nanoplatform

Currently, a wide range of medical imaging techniques such as ultrasound (US), computed tomography (CT), positron emission tomography (PET), single photon emission computed tomography (SPECT) and magnetic resonance imaging (MRI) are commonly employed for clinical diagnostics. Among these imaging methods PET and SPECT offer greater sensitivity compared with other modalities, such as CT, MRI and US. However, CT and especially MRI provide higher-resolution images with anatomical resolution and soft-tissue contrast[6]. Therefore, multimodality imaging is desirable to combine complimentary information from different imaging modalities. Especially, MRI is proving to be the better technique for certain medical cases such as diagnosis of breast cancer[85], brain tumors[86] and hepatocellular carcinoma[87] for its superior soft tissue contrast and anatomical resolution, nearly unlimited tissue penetration and its ability to acquire whole body images noninvasively within reasonable time frame. Besides with MRI, subjects are not exposed to ionizing radiation like X-rays of CT during imaging. Moreover, with the use of contrast agents, better contrast and signal amplification can be achieved in order to improve MRI sensitivity. Although paramagnetic gadolinium diethylenetriaminopentaacetic acid (Gd-DTPA) is widely used for its strong T_1 shortening affect, it has relatively low contrast enhancement and a very short retention time in vivo. On the other hand, super paramagnetic iron oxide (SPIO) nanoparticles are much more efficient as relaxation promoters, have long circulation time, low

toxicity and biodegrability[24, 88-92]. In addition SPIO based contrast agents are currently approved for clinical use[93, 94]. Therefore development of a liposomal formulation that incorporates SPIO and therapeutic agent is investigated.

2.2.1 Nanoplatform Design and Composition

Traditionally SPIOs are made in aqueous solution by co-precipitating Fe (II) and Fe (III) precursors[17, 18] and typically hydrophilic polymers are added during the

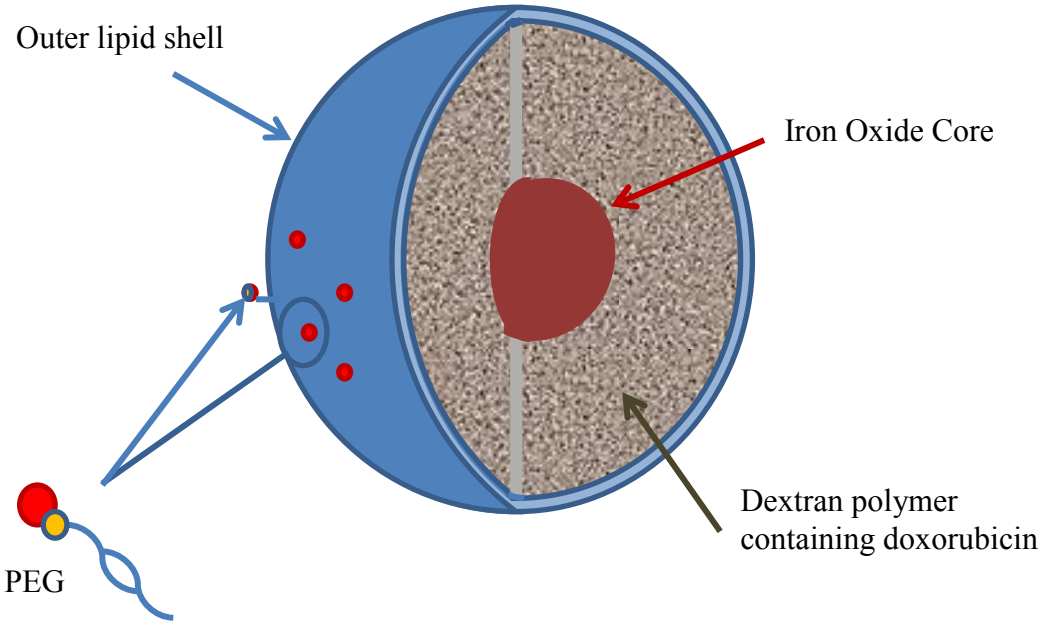

Figure 7 Schematic of the developed liposomal SPIO based theranostic nanoparticle

The inner is composed of SPIO encapsulated by cross-linked dextran, which is the site for drug loading. The outer lipid bilayer shell composition included poly(ethylene glycol) (PEG) and can be covalently attached to targeting moieties.

particle formation process to prevent particle aggregation and render SPIOs hydrophilic with dextran and its derivatives being the most studied. Several dextran-

SPIO formulations have entered or already passed the clinical trials as MRI contrast agents[19] and dextran-core nanoparticles loading both hydrophilic and hydrophobic drugs have been described previously[95, 96]. Therefore, we sought to develop liposomal theranostic nanoparticles having a dextran core, a coating material typically used to render iron oxide hydrophilic, with payload of Doxorubicin (DOX), an effective anticancer drug, as the therapeutic agent, SPIO as the MRI contrast agent. A schematic representation of the theranostic nanoparticles is shown in Figure 7. The developed liposomal nanoparticles can potentially carry both hydrophilic and hydrophobic drugs and be detected with MRI. Moreover, outer shell constituents such as poly (ethylene glycol) (PEG), targeting moieties and fluorophores can be added without affecting the payload.

The lipid shell composition of liposomal nanoparticles includes three types of lipids, poly (ethylene glycol) (PEG) to improve circulation time[78, 79], boron-dipyrromethene (BODIPY) 630/650-DOPE fluorophore to allow fluorescent imaging and photopolymerizable acetylene groups for improved stability[97, 98] as tabulated in Table 3.

2.2.2 Nanoplatform Preparation

In general, a typical procedure involves mixing of lipids in an organic phase followed by drying, hydration during agitation, and sizing down to get the desired homogeneous population as shown schematically in Figure 8. Usually, the lipids are first dissolved in chloroform or chloroform/methanol mixtures and the solvent is

Table 3 SPIO Based Nanoplatform Outer Lipid Shell Constituents

Constituent	Synonyms	Fatty Acid	Percent of Outer Shell
DOPE dioleoylphosphatidylethanolamine	1,2-di-(9Z-octadecenoyl)-*sn*-glycero-3-Phosphoethanolamine	18:1	30
DSPC distearoylphosphatidylcholine	1,2-dioctadecanoyl-*sn*-glycero-3-phosphocholine	18:0	28
Cholesterol			20
DSPE-mPEG2000 Distearoylphosphatidylethanolamine-N-monomethoxy polyethyleneglycol	1,2-distearoyl-*sn*-glycero-3-phosphoethanolamine-N-[methoxy(polyethylene glycol)-2000]	18:0	15
BODIPY 630/650-DOPE boron-dipyrromethene		18:1	2
Photopolymerizable Acetylated DOPE	6-(4,4-difluoro-5-(2-thienyl-4-bora-3a,4a-diaza-s-indacene-3-yl)styryloxy-acetyl)aminohexamido-DOPE	18:1	5

evaporated by rotary evaporation or using a dry nitrogen or argon stream. Then the dry film is thoroughly dried by placing the vial or flask under vacuum pump overnight and lyophilized until dry. Next, the dry lipid film is hydrated by adding an aqueous medium at a temperature above the gel-liquid transition temperature (Tc or Tm) of the lipid with the highest Tc to the container and agitated. Hydration time may differ slightly depending on the application and constituents of the lipid mixture but a hydration time of 1 hour with vigorous shaking, mixing is recommended. The hydration step produces large, multilamellar vesicles (LMVs) with each lipid bilayer separated by an aqueous layer. Finally, sonication or extrusion is used to size down the

LMVs. Typically, sonication produces small, unilamellar vesicles (SUVs) with diameters in the range of 15-50 nm and extrusion through membranes with 100 nm pores produces large, unilamellar vesicles (LUVs) with diameters in the range of 100-140nm. While extrusion is more laborious, it produces more homogeneous liposomes and can be scaled up for large-batch preparations.

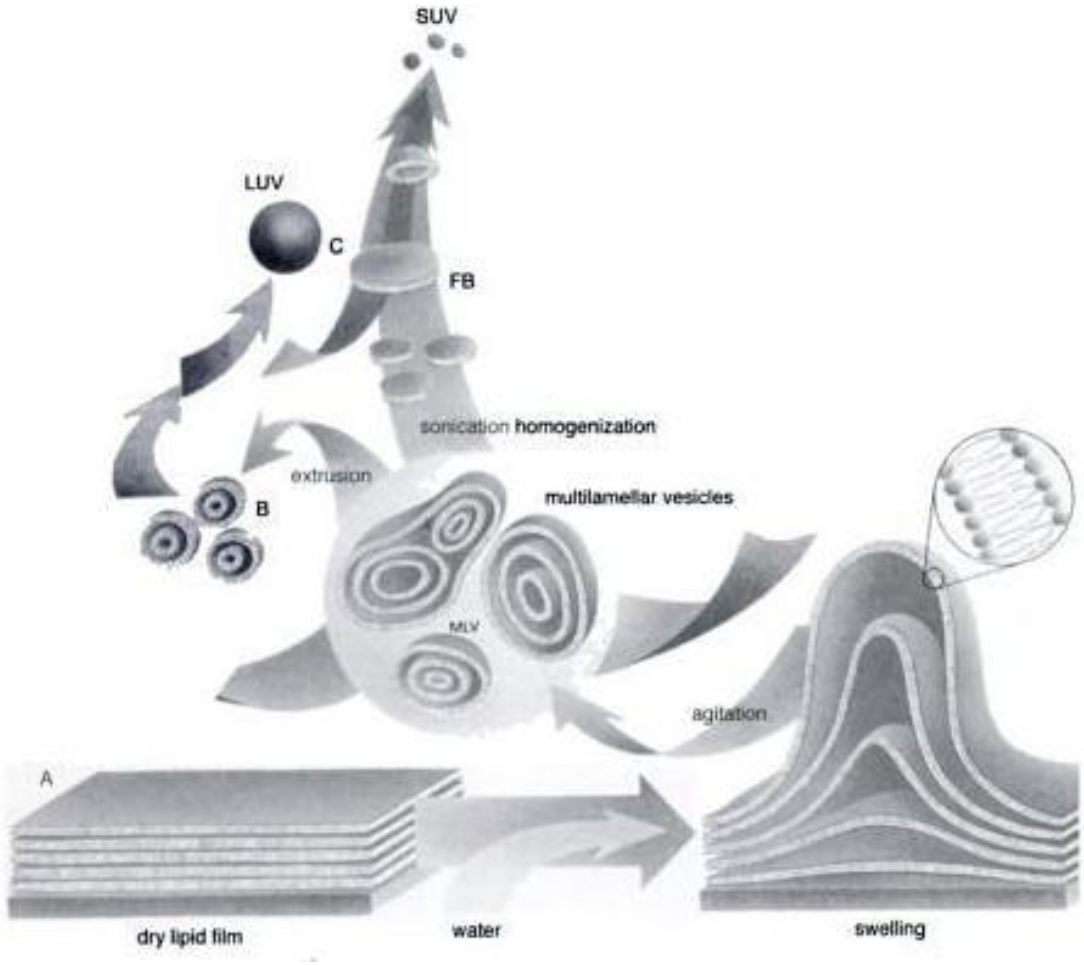

Figure 8 Schematic of Liposome Preparation[99]

2.2.2.1 Liposomal SPIO Based Theranostic Nanoplatform Preparation

Dextran coated SPIO particles are treated with doxorubicin hydrochloride dissolved in phosphate buffered saline (PBS) for 24 hours and are purified using G25 size exclusion chromatography. Followed by DOX treatment of dextran core, the shell formulation of DOPE/DSPC/cholesterol/DPSE-mPEG2000/BODIPY-DOPE/ Photopolymerizable Acetylated DOPE (listed in Table 3) in chloroform is evaporated in a Buchi Rotavapor system and the dried film is hydrated with 1-5 mg/mL of DOX loaded purified dextran core suspension. Liposomes are sonicated in bath sonicator for 2-3 minutes at room temperature to produce multilamellar vesicles (MLVs) and then are sonicated with a high-energy probe sonicator for 1-2 minutes to produce small unilamellar vesicles (SUVs). To reduce the size of the liposomes, stepwise extrusion is performed through 400-nm, 200-nm and 100-nm polycarbonate membranes sequentially. After extrusion through polycarbonate membranes, the liposome suspension is irradiated for 3-5 minutes under a mercury arc lamp. The size distribution of the final liposome suspension is verified with Malvern Zetasizer using dynamic light scattering and stored at 4ºC.

2.2.3 Results

2.2.3.1 Size

10µL of the nanoparticle suspension was diluted to 100µL in PBS and the size distribution of the sample was measured using a Malvern Zetasizer via dynamic light

scattering and the resulting graph is shown in Figure 9. The average diameter of the nanoparticles was about 100 nm and the measured polydispersity index (PDI) of the sample was approximately 0.25.

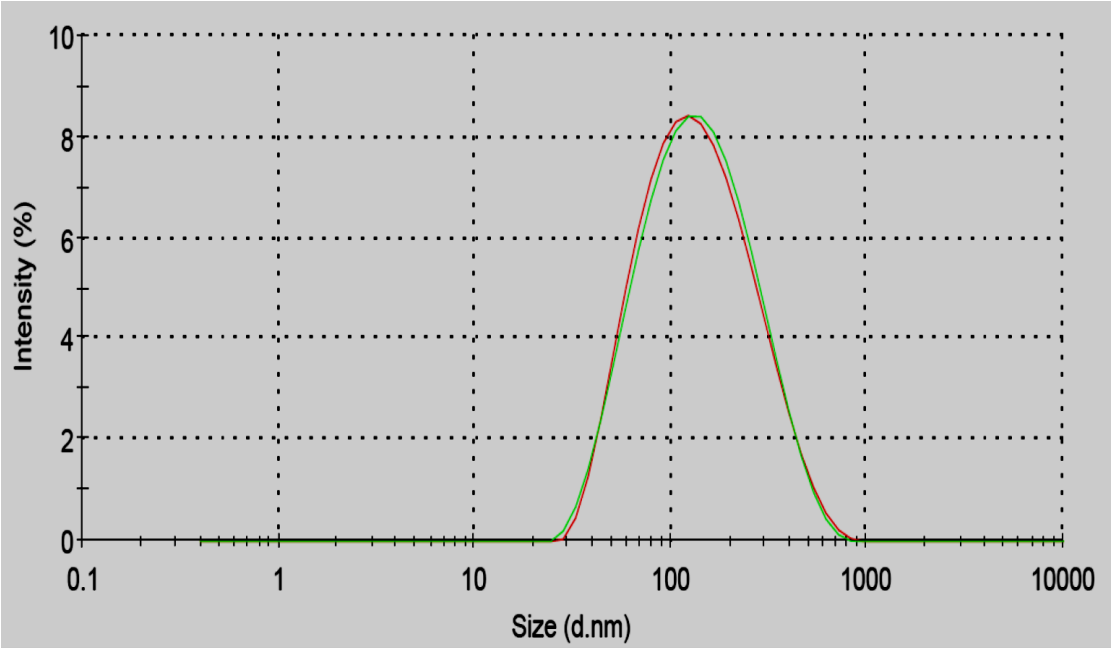

Figure 9 Liposomal theranostic nanoparticle size distribution

The mean diameter of the liposomal theranostic nanoparticles is measured to be 113 nm by a Malvern Zetasizer via dynamic light scattering. The graph above shows intensity versus particle size in nm.

2.2.3.2 Particle Structure

In order to verify the BODIPY 630/650 incorporation into the lipid membrane, two batches of nanoparticle suspensions, fluorescently labeled and unlabeled, were prepared and then were subjected to magnetic field. The particles concentrate to a location closest to the magnetic field in the vial and the vial solution was then

aspirated carefully and replaced. This washing procedure was repeated five times. A control solution of unlabeled nanoparticle suspension with free BODIPY fluorophore added to the suspension was subjected to the same washing procedure. Then the fluorescence of the vial containing fluorescently labeled nanoparticles and the control were measured. Fluorescence measurements confirmed that the control vial contained no fluorescence whereas the fluorescently labeled nanoparticle suspension was fluorescent after five washes, indicating that it contained intact fluorescent nanoparticles with a magnetic payload.

Subsequently, in order to demonstrate dextran encapsulation, rhodamine PE (excitation peak 557/ emission peak 571) labeled liposomes with Fluoresceinisothiocyanato-dextran 2000 (FITC-Dextran 2000 – 2 Million Daltons excitation peak 490/ emission peak 520) payload and a second batch with no payload as control were prepared. Then each batch was run through Sepharose 4B size exclusion column and fractions were collected. The fluorescence of fractions from both batches was measured with TECAN and normalized values are graphed in Figure 10. Both control and sample had a single peak with control having an earlier peak. The absence of a second peak for liposomes with FITC-Dextran 2000 payload shows that the FITC-Dextran 2000 was not dissociated into free smaller fragments.

In order to further verify the nanoparticle structure, theranostic nanoparticle suspension was prepared as described previously. Then, nanoparticle suspension was diluted ten folds in filtered water, dried onto silicon wafer pieces, and then scanning electron microscope (SEM) images were acquired with a Philips XL-30 scanning

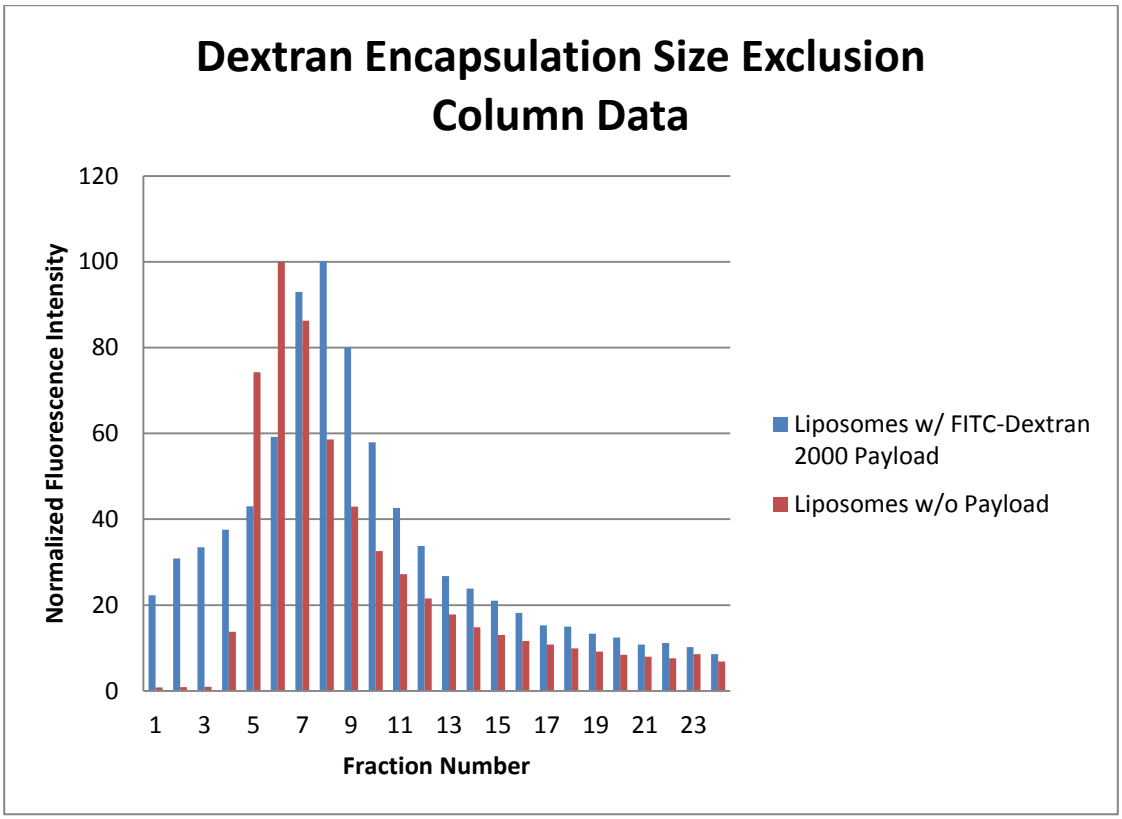

Figure 10 Dextran Encapsulation Experiment Normalized Fluorescence Data

There is a single early peak for empty liposomes. Liposomes with FITC-Dextran 2000 payload show a single peak as well. The absence of a second peak shows that there was no free FITC-Dextran 2000.

electron microscope equipped with an Energy Dispersive Spectrometer (EDS). The scale bar at the bottom of SEM image of nanoparticles shown in the right panel of Figure 11 indicated the particles were indeed around 100 nm in diameter. The dark centers of visible spheres represent the SPIO core and the chemical composition analyzed with EDS also confirmed the presence of SPIO within the nanoparticles.

In order to quantify DOX loading, DOX loaded purified dextran core suspension was methanol extracted. Then different amounts of DOX was diluted in

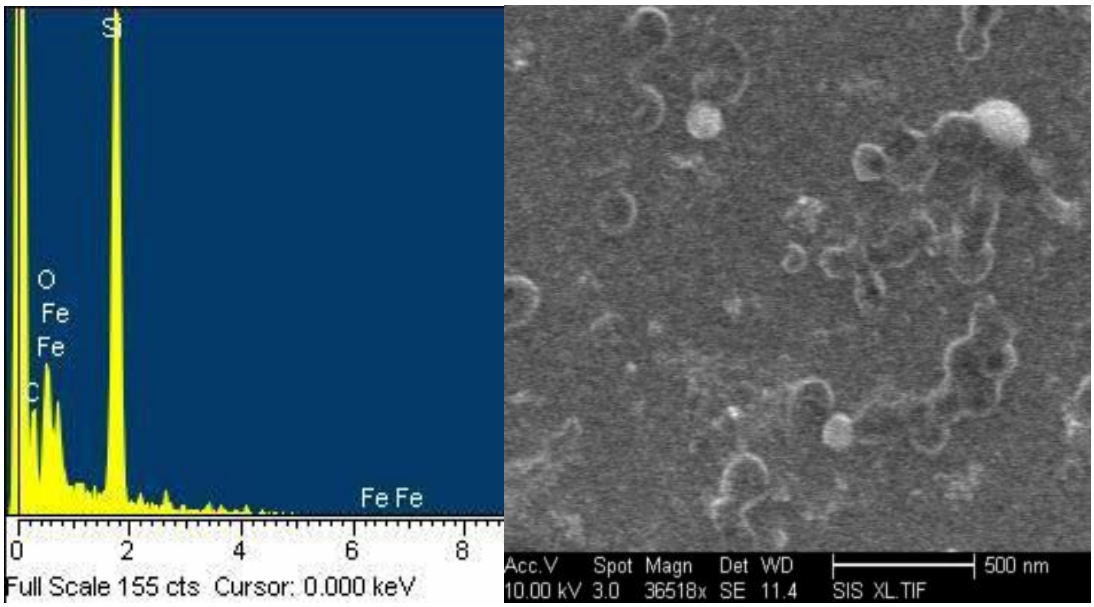

Figure 11 SEM image and composition of theranostic nanoparticles

Right panel is scanning electron microscope (SEM) image of theranostic nanoparticles. The spherical lipid shell can be seen in many of the particles. The scale bar at the bottom indicates that the particles are around 100 nm in diameter. The left panel is the chemical compositional mapping of the nanoparticles analyzed with Energy Dispersive Spectrometer (EDS). The chemical composition indicates the presence of iron within the nanoparticles.

methanol as reference and the fluorescence of the sample and DOX references with known amounts of DOX was measured using TECAN fluorescence spectrophotometer at 484 nm excitation and 584 nm emission. The fluorescent measurements shown in Figure 12 indicated that the theranostic nanoparticles indeed carried a DOX payload and the DOX uptake of the dextran core was at least 60 μg/mL of particle suspension.

2.2.3.3 MR Relaxivity

In order to determine the effectiveness of liposomal theranostic nanoparticles as MR contrast agents, the liposomal nanoparticle suspensions and dextran coated

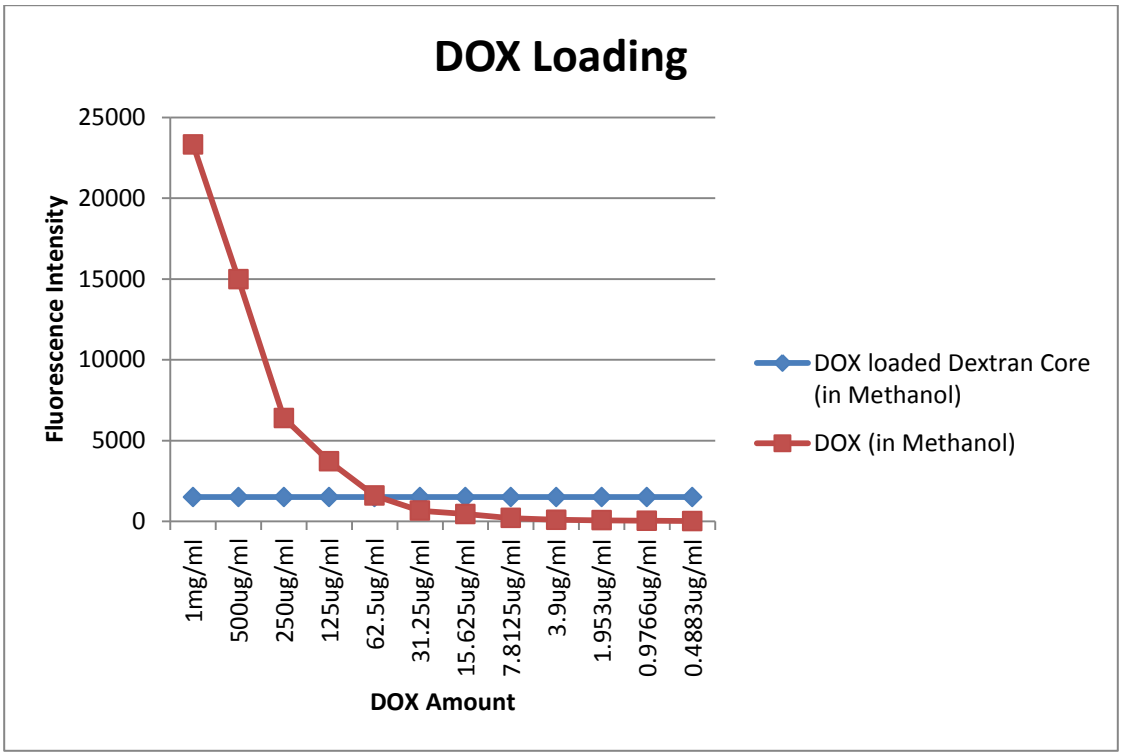

Figure 12 DOX loading

DOX uptake of the dextran core is determined by comparing the fluorescence intensity of the methanol-extracted core with reference DOX dilutions in methanol. The fluorescence intensity was measured at 484 nm excitation and 584 nm excitation with TECAN fluorescence spectrophotometer.

SPIO core suspensions were subjected to relaxivity measurements. Initially, the iron concentrations of dextran coated SPIO core suspension and liposomal theranostic nanoparticle suspension were measured using a Perkin-Elmer 3700 Optical Emission Plasma Spectrometer as 172 µg/mL and 167 µg/mL respectively before dilution and 12.7 µg/mL and 12.9 µg/mL after dilution. Subsequently, the diluted suspensions and tap water were subjected to multi-echo spin echo (SE) protocols (TE = 11, 22, 44, 88, 120 ms, TR = 2000 ms) using a 3T GE Excite MRI system and T_2 values of diluted

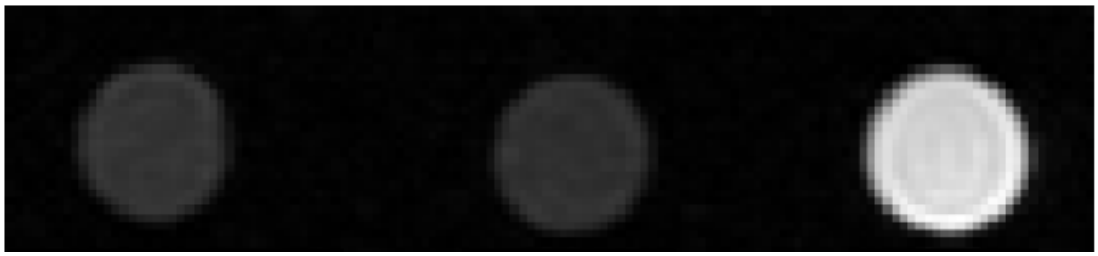

Dextran-SPIO Core | **Liposomal Theranostic Nanoparticles** | **Tap Water**

Figure 13 T_2 Weighted MR Image of Samples

T_2 weighted spin echo image of the samples and tap water in different vials (TE = 88 ms, TR = 2000 ms) were acquired with 3T GE Excite. The images of samples exhibit signal dropout compared to tap water due to T_2 shortening effects of SPIO particles.

samples were measured. R_2 relaxivity values were calculated using the measured T_2 values and concentrations according to the following formula:

$$\left(\frac{1}{T_2(Sample)} - \frac{1}{T_2(tap\ water)}\right) = R_2 \times [CM]$$

Acquired MR image of sample suspensions and tap water is shown in Figure 13 and the calculated R_2 values are listed in Table 4 together with the R_2 values of two commercial products[100]. The T_2 weighted MR image revealed darkening in both sample vials due to T_2 shortening effect of SPIO particles. The calculated value of R_2 for Dextran-SPIO core was very close to the R_2 value of liposomal theranostic nanoparticles indicating that the lipid shell encapsulation didn't affect the T_2 reducing effect of SPIO particles. Moreover, the R_2 value of both liposomal nanoparticles and Dextran-SPIO core were comparable to the two commercially available iron oxide

based contrast agents (ferumoxide based Feridex/Endorem, AMAG Pharmaceuticals and ferrixan based Resovist, Bayer Schering Pharma).

Table 4 Comparison of R_2 values of Liposomal Theranostic Nanoparticles, Dextran-SPIO Core and Commercial Contrast Agents

Vial Constituent	T_2 (ms) 3T	R_2 (1/mM . s) 3T
Tap water	1374	N/A
Dextran-SPIO Core	39	109.55
Liposomal Theranostic Nanoparticles	41	102.44
Feridex (Endorem)[100]		93
Resovist[100]		143

2.2.4 Conclusion

A novel SPIO based liposomal theranostic nanoparticle that can be imaged by MRI and fluorescence microscopy and capable of carrying at least 60 μg/mL of DOX as therapeutic agent is demonstrated. Acetylated lipids were incorporated into the lipid shell in order to improve in vivo stability and PEG was incorporated to improve circulation time. The proposed structures of the nanoparticles were verified with various experiments and their MR contrast agent effectiveness was shown to be comparable or better than commercially available contrast agents currently in use.

2.3 Microbubble Based Theranostic Platform

Ultrasound (US) has become one of the most common clinical imaging modalities due to its low cost, fast image acquisitions, simplicity, portability and safety especially for the diagnosis and monitoring of pregnant women and their unborn babies. US imaging involves exposing region of interest to high frequency (1 to 50 MHz) sound waves emitted from a transducer placed against the skin to produce images based on the sound waves reflected back. Similar to MRI, the sensitivity of the US can be improved as well by administration of contrast agents that exploit the echogenicity, the ability of an object to reflect the US waves, difference between the contrast agent and the soft tissue surrounding of the body. Typically, US contrast agents such as clinically used Definity® (2001) and Imagent® (2002) are encapsulated microbubbles (1-10 μm in diameter) and work by resonating strongly at the high-frequency used for US imaging. Microbubble based contrast agents have proven clinical value as a diagnostic tool in cardiology[101], radiology[102] and oncology. More important, microbubbles can aid in site-specific drug delivery by sonoporation, creation of perforations in cell-membrane using ultrasound[103]. In general, sonoporation requires high acoustic power, but microbubbles greatly reduce the power needed by lowering the amount of energy necessary for cavitation, the process of microbubble collapse by extreme oscillations induced by US[104, 105]. The circulation of these microbubbles can be followed with US, and when they reach the target area, they can be disrupted to release the therapeutic agents to the surrounding tissue[106]. Therefore

development of a liposomal formulation that incorporates microbubble and therapeutic agent is investigated.

2.3.1 Platform Design and Composition

One of the biggest limitations with the current cancer therapy with chemotherapeutics is the systemic toxicity and lack of selectivity to tumor tissue[107]. Therefore several targeted chemotherapeutics delivery schemes have been proposed in order to reduce morbidity associated with systemic toxicity and increase the drug efficacy. Currently, several microbubble based US contrast agents (Optison®, Definity® and Imagent®) are already in clinical use and their therapeutic potential has recently begun to attract attention[108]. These microbubble based US contrast agents can be followed with US, and when they reach the target area, they can be disrupted to release the chemotherapeutic agents to the surrounding tissue[106]. Consequently, we sought to develop liposomal theranostic particles having a payload of Doxorubicin (DOX), an effective anticancer drug, as the therapeutic agent and microbubble as the US contrast agent for US imaging and remote disruption of the liposomal particle at the tumor site. A schematic representation of the theranostic particles is shown in Figure 7. The developed liposomal particles can potentially carry both hydrophilic and hydrophobic drugs, be detected with US and can be remotely disrupted to deliver chemotherapeutic payload at the tumor site, hence reduce systemic toxicity and improve the delivery and cellular uptake of DOX. Moreover, outer shell constituents such as poly (ethylene glycol) (PEG), targeting moieties and fluorophores can be

added without affecting the payload. A schematic representation of the theranostic particles is shown in Figure 14.

The lipid shell composition of liposomal nanoparticles includes three types of lipids, poly (ethylene glycol) (PEG) to improve circulation time[78, 79], boron-dipyrromethene (BODIPY) 630/650-DOPE fluorophore to allow fluorescent imaging and photopolymerizable acetylene groups for improved stability[97, 98] as tabulated in Table 3. Three types of lipids form the lipid shell of the microbubbles as tabulated in Table 5 and perfluoropropane (aka octafluoropropane C_3H_8) forms the gas core for its low solubility in water.

Table 5 Microbubble Lipid Shell Constituents

Constituent	Synonyms	Fatty Acid	Molar Ratio of Outer Shell
DPPC dipalmitoylphosphatidylcholine	1,2-dipalmitoyl-*sn*-glycero-3-phosphocholine	16:0	81
DPPA dipalmitoylphosphatidic acid	(1,2-dipalmitoyl-*sn*-glycero-3-phosphate	16:0	8
DPPE-mPEG5000 dipalmitolyphosphatidylethanolamine–polyethyleneglycol	1,2-dipalmitoyl-*sn*-glycero-3-phosphoethanolamine-*N*-[methoxypoly(ethylene glycol)-5000]	16:0	10

2.3.2 Platform Preperation

In general, the lipid coated microbubbles are prepared by sonication, which involves the application of high intensity ultrasound to disperse a portion of the gas

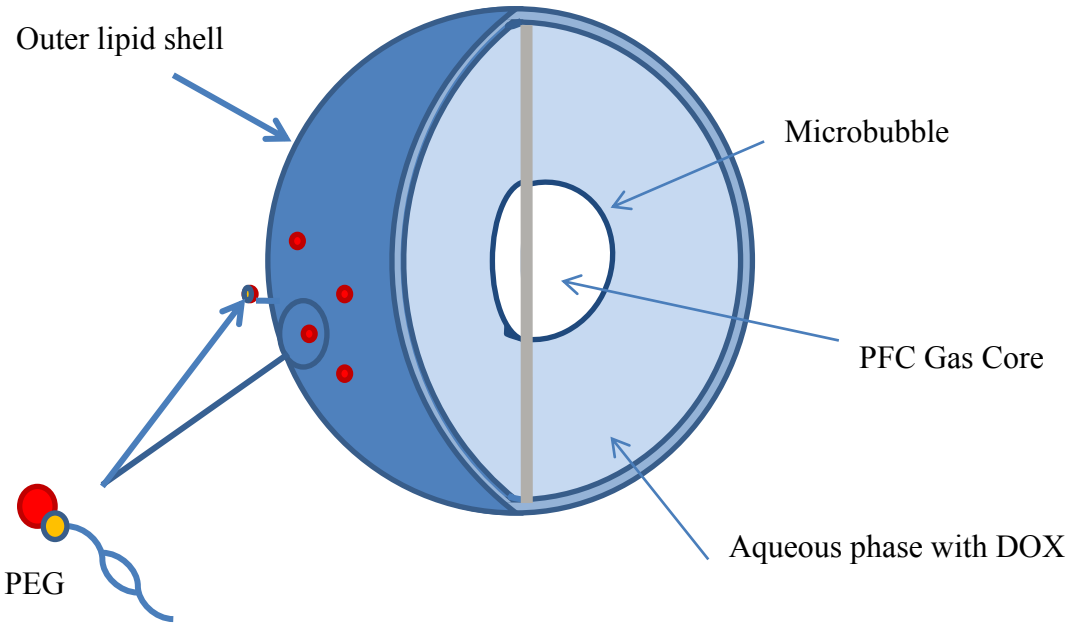

Figure 14 Schematic of the developed liposomal microbubble based theranostic particle

The inner is composed of microbubble and aqueous phase for hydrophilic drug loading. The microbubble is composed of PFC gas core and lipid monolayer shell. The outer lipid bilayer shell composition included poly(ethylene glycol) (PEG) and can be covalently attached to targeting moieties.

phase within the aqueous phase of the lipid shell constituents. However, the sonication method results in microbubbles with broad size distribution which depends upon the frequency, power and pulse regime of the ultrasound protocol applied[109, 110]. Since the resonance frequency of a microbubble depends on its diameter, only a small portion of the microbubble population can respond to the limited bandwidth of ultrasound transducer which results in reduced sensitivity of the imaging system. Similarly, traditional liposome preparation method of lipid film hydration, agitation followed by

extrusion results in limited loading efficiencies. In recent years, generations of highly controlled droplet dispersions[111-113] and microbubbles[111, 114, 115] using microfluidic techniques have already been demonstrated. Therefore we sought to use preparation methods based on microfluidic techniques.

Microfluidic systems deal with precise control and manipulation of fluids that are geometrically constrained to a small scale. To generate microbubble based theranostic particles, flow-focusing technique, forcing a central stream and two side sheath flows of a liquid mixture through a narrow orifice, is utilized. The devices are fabricated following standard soft lithography techniques[116]. First, the channel pattern is drawn using a CAD tool and then printed on a transparency using high-resolution plotter to be used as a mask for photolithography. Next, a silicon wafer is spin coated with a layer of photoresist, UV-curable epoxy, and the mask is placed between a UV light source and the silicon wafer that has been coated with photoresist. Exposure to UV light transfers the pattern from the mask to the photoresist and unexposed photoresist is removed using an organic solvent. Then, the wafer with the channel pattern is treated with perfluoralkyl trichlorosilane to prevent the poly(dimethylsiloxane) (PDMS) from sticking. Next, liquid prepolymer of PDMS is mixed with curing agent at a weight ratio of 10:1, degassed and poured on the wafer with the channel pattern. After thermal curing at 65ºC, the PDMS layer is peeled away; inlets and outlets are punched and bonded to clean soda lime glass after oxygen plasma treatment in order to seal the channels. Typical soft lithography process is described schematically in Figure 15. Once the device fabrication is complete, the

liquid phases are pumped at a constant rate using digitally controlled syringe pumps and the gas phase is supplied from a pressurized tank through a digital gas flow controller into the corresponding punched inlets. The generation process is observed using high-speed camera attached to a conventional bright field microscope and the particle size estimation is done by using image analysis software for the acquired video images.

Subsequently, in order to overcome the volume production limitation and scalability of microfluidic flow-focusing systems, we sought to develop preparation methods based on silicon nozzles. Monodisperse droplets are generated by dispersing one phase into a second immiscible phase through a precise silicon nozzle fabricated in the cleanroom using cryogenic etching techniques.

First, the nozzle pattern is drawn using a CAD tool and then printed on a transparency using high-resolution plotter to be used as a mask for photolithography. Next, a silicon wafer is spin coated with a layer of photoresist, UV-curable epoxy, and the mask is placed between a UV light source and the silicon wafer that has been coated with photoresist. Exposure to UV light transfers the pattern from the mask to the photoresist and unexposed photoresist is removed using an organic solvent. Next, depending on the process, a metal layer is deposited as well to act as etching mask. The desired nozzle patterns are etched through using cryogenic deep reactive ion etching (cryo-DRIE). While anisotropic etching is possible by wet etching techniques as well, the etching is dependent on the crystalline structure of the silicon and only

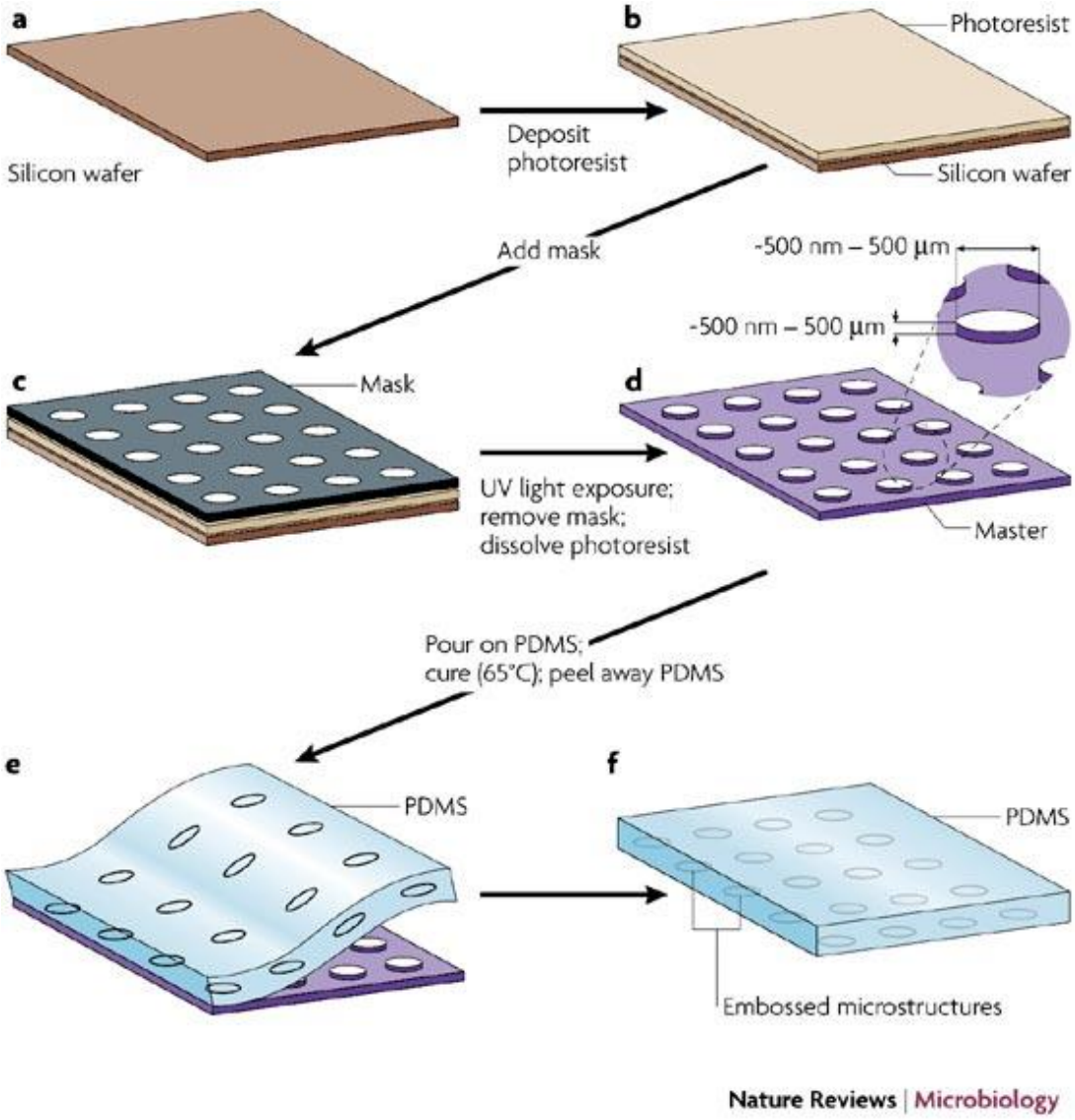

Figure 15 The fabrication of micropatterned slabs of PDMS[117]

a-b Photoresist is spin coated on silicon wafer. **c** A mask is placed in contact with the layer of photoresist. **d** The photoresist is illuminated with ultraviolet (UV) light through the mask. An organic solvent dissolves and removes photoresist that is not crosslinked. The master consists of a silicon wafer with features of photoresist in bas-relief. An expanded view of one of the microfabricated structures with its characteristic critical dimension is shown. **e** PDMS is poured on the master, cured thermally and peeled away. **f** The resulting layer of PDMS has microstructures embossed in its surface

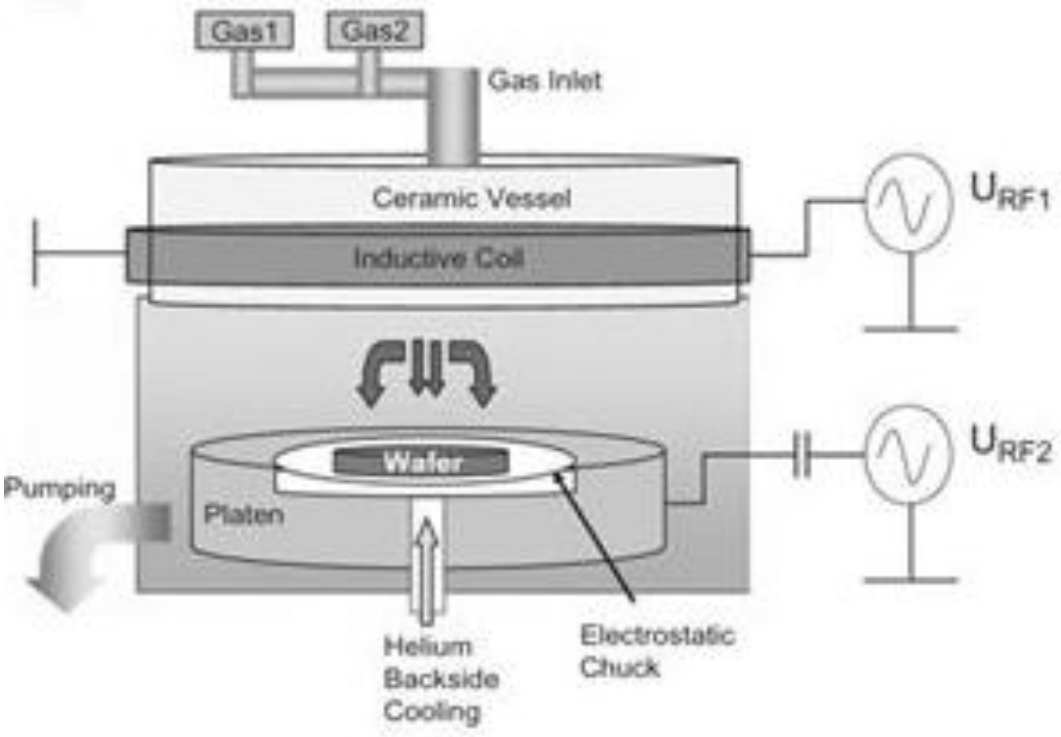

Figure 16 Schematic of cryo-DRIE Reactor

Schematic of cryo-DRIE reactor with inductively coupled plasma (ICP) source with excitation coil wound around large dielectric vessel[118]

certain features can be etched using this technique. On the other hand, reactive ion etching is also capable of anisotropic etching but high aspect ratio structures are not feasible with this method. Bosch process is also capable of anisotropic etching with high aspect ratio but produces scalloping patterns on the sidewalls due to its alternating etching/polymer deposition steps[119]. In cryo-DRIE, etching takes place in SF_6/O_2 plasma according to the chemical reaction:

$$3Si\ (s) + 2SF_6\ (g) + 2O_2\ (g) \rightarrow 3SiF_4\ (g) + 2SO_2\ (g) + SiO_xF_y$$

At cryogenic temperatures (T < -100 ºC), a passivating SiO_xF_y layer forms on top of the silicon surface and directional ion bombardment removes mainly the passivation layer on horizontal surfaces while sidewalls are protected with mostly intact

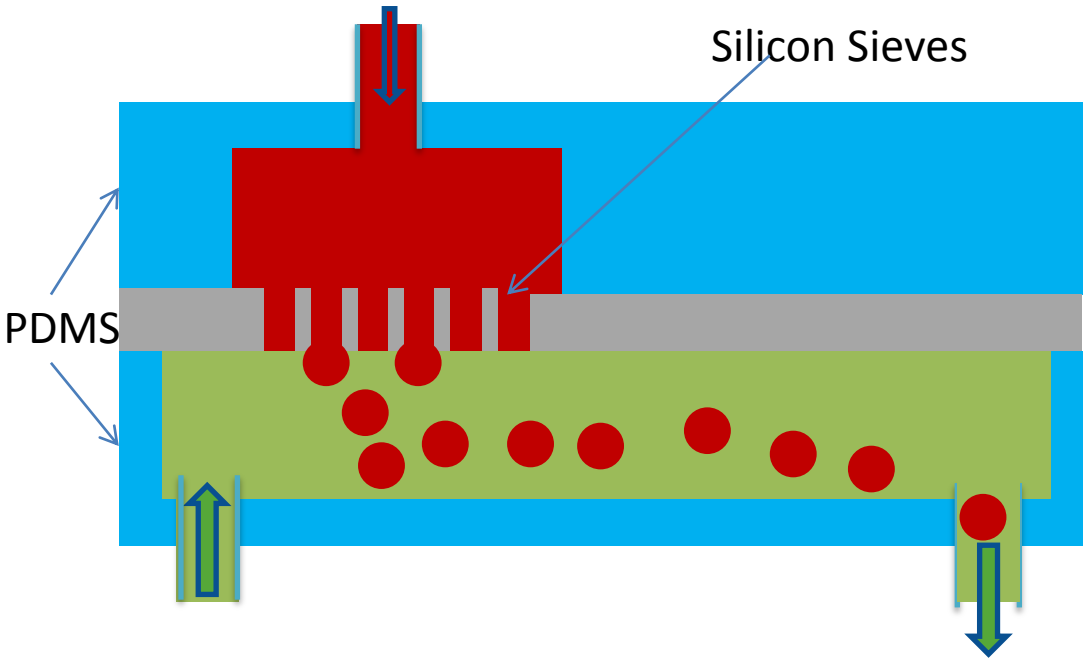

Figure 17 Schematic of droplet generation via Silicon nozzles

Monodisperse droplets are generated by dispersing one phase into a second immiscible phase through a precise silicon nozzle fabricated in the cleanroom using cryogenic etching techniques.

passivation layer[120, 121]. A typical cryo-DRIE reactor with two RF generators and Helium backside cooling stage is shown in Figure 16. The desired etching rate and profile is acquired by adjusting the flow rate of the gases, ICP power, bias voltage, process pressure and temperature. Typically, too low O_2 flow results in isotropic etching profiles while too high oxygen content leads to over passivation, a reduction in

etching rate, formation of black silicon [122] and/or sidewalls with positive slope. Higher SF_6 flow rate and ICP power results in higher etch rate but might result in negative sidewalls. Usually, higher temperatures results in higher etch rates but results in thinner passivation layers and more isotropic etching profiles.

Once the nozzles are etched through, the nozzles are sandwiched between two PDMS channels with inlets and outlets are punched and the gas or liquid phases are introduced using digitally controlled syringe pumps or pressured gas tanks via clear tygon tubes. The schematic of the droplet generation via Si nozzles is shown in Figure 17. The generation process is observed using conventional bright field microscope and the particle size estimation is done by using image analysis software for the acquired images.

2.3.2.1 Liposomal Microbubble Based Theranostic Particle Platform Preparation using Microfluidic Flow-Focusing PDMS Devices

The microbubbles need to be smaller than 10 μm in diameter in order to pass through the capillaries of the lungs without causing obstruction[123]. On the other hand, the echogenicity of microbubbles is a function of the sixth power of its radius, meaning smaller microbubbles have poor US contrast agent properties[115]. Therefore, microbubbles with 2-5 μm in diameter were generated. In order to achieve this, perfluoropropane was supplied from a pressurized tank through a digital gas flow controller into the gas inlet of the microfluidic flow-focusing device with 7 μm orifice. The microfluidic device channel design is shown in Figure 18 with two liquid inlets

and one gas inlet and two orifices with 7 μm and 20 μm in width. All channels have a rectangular cross section and a height of 25 μm. A close up view of the two orifices of the microfluidic device channels is shown in bottom frame of Figure 18. The diamond shape expansion after the nozzle was used to focus the bubble break-off location to one single point located at the orifice[115]; the narrowest point incurs the highest shear force, and allow the generation of a velocity gradient after bubble formation to reduce the shear force experienced by the microbubbles generated.

Two side sheath flows of liquid phase was prepared using microbubble shell formulation of DPPC/DPPA/DPPE-mPEG5000 in chloroform hydrated/sonicated with GPW (10% glycerin, 10% propylene glycol, 80% water) after evaporation and was pumped at a constant rate using digitally controlled syringe pumps into the liquid inlet of the device. The second side sheath flows of liquid phase was prepared using liposome formulation of DOPE/DSPC/cholesterol/DPSE-mPEG2000/BODIPY-DOPE/ Photopolymerizable Acetylated DOPE (listed in Table 3) in chloroform and was pumped at a constant rate using digitally controlled syringe pumps into the second liquid inlet of the device. Then a third side sheath flows of liquid phase was planned using the same liposome formulation of DOPE/DSPC/cholesterol/DPSE-mPEG2000/BODIPY-DOPE/ Photopolymerizable Acetylated DOPE (listed in Table 3) in chloroform hydrated/sonicated with GPW after evaporation in order to form outer lipid bilayer shell with the removal of chloroform via evaporation. The generated microbubbles in chloroform emulsion were collected at the outlet and stored in glass vials.

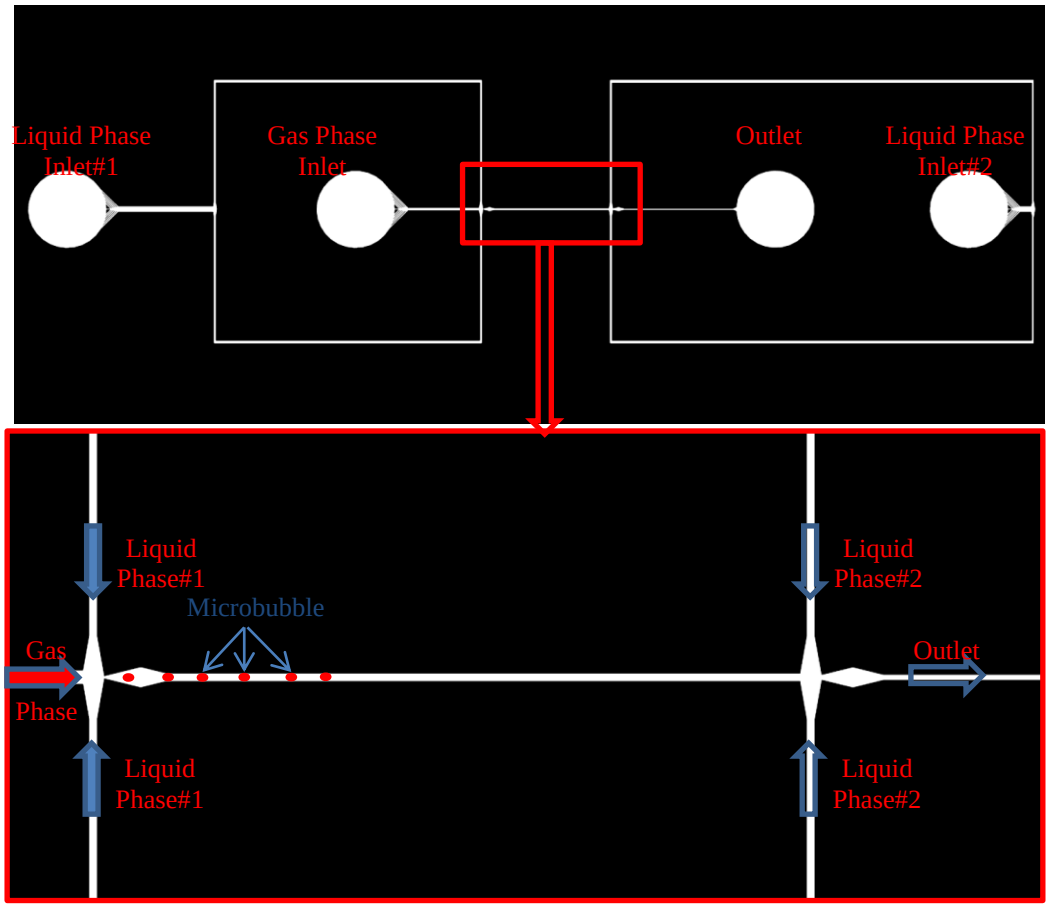

Figure 18 Schematic view of the microfluidic flow-focusing device

Schematic view of the microfluidic flow-focusing device is shown at the top frame. All channels have a rectangular cross section and a height of 25 µm. There are two liquid inlets, one gas inlet and one outlet. The device has two nozzles with 7 µm and 20 µm in width. The bottom frame shows the close-up view of the two nozzles with 7 µm nozzle being the one on the left. The diamond shaped expanding nozzle focuses the generation of microbubbles to orifice and reduces the shear forces on the generated microbubbles by allowing the generation of a velocity gradient.

2.3.2.2 Large-Scale Monodisperse Liposomal Microbubble Based Theranostic Particle Platform Preparation using Silicon-SU8 Nozzles

In order to generate microbubles around 5μm, silicon-SU8 nozzles were fabricated using cryo-DRIE in SF_6/O_2 plasma. Once the nozzles were etched through, a thin SiO_2 film was deposited on and the nozzles were sandwiched between two PDMS channels bonded on after oxygen plasma treatment. Later gas phase was supplied from a pressurized tank through a digital gas flow controller into the gas inlet of the PDMS channel and the liquid phase composed of microbubble shell formulation of DPPC/DPPA/DPPE-mPEG5000 in chloroform hydrated/sonicated with GPW (10% glycerin, 10% propylene glycol, 80% water) after evaporation was introduced with digitally controlled syringe filters into the liquid inlet and the generated microbubbles were collected at the outlet.

2.3.3 Results with Microfluidic Flow-Focusing Devices

2.3.3.1 Size

A regular bright field microscope and high-speed camera was used to acquire images of the generated microbubbles and image analysis software was used to estime the size of the microbubbles generated. A typical image of monodisperse microbubbles generated using flow-focusing microfluidic is shown in Figure 19.

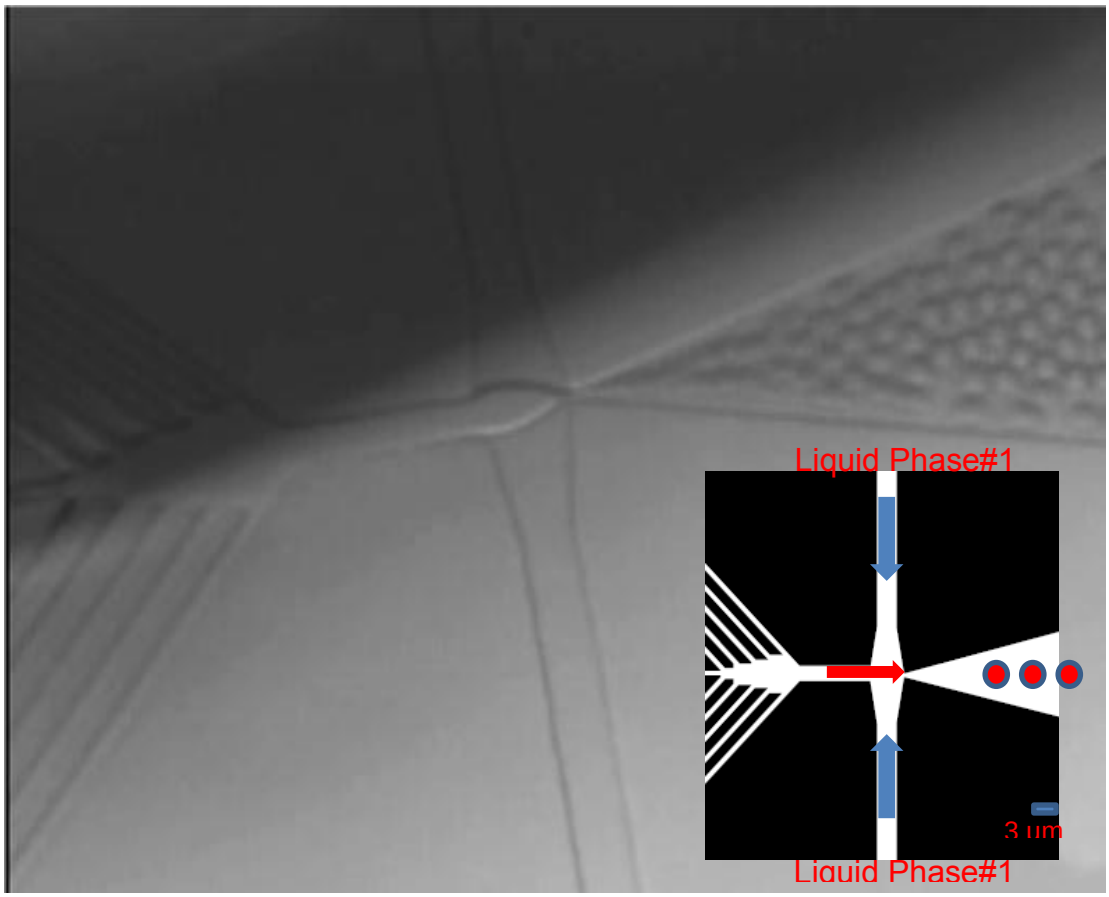

Figure 19 Picture of the microbubbles generated with flow-focusing microfluidic device

Picture of the monodisperse microbubbles generated with flow-focusing microfluidic device at 7 μm orifice. The schematic view of the microfluidic flow-focusing device with flow directions is shown at the right corner.

A sequence of high-speed images of generated microbubbles being encapsulated in second liquid phase at 20 μm orifice is shown in Figure 20. The diameters of the microbubbles were estimated to be around 10 μm and of emulsions with microbubbles encapsulated were around 30 μm. Since the bubble size is proportional with orifice diameter according to the equation[115] $d_b/D \propto (Q_g/Q_l)^{0.4}$ where d_b is bubble diameter,

D is orifice diameter and Q_g and Q_l are the gas and liquid flow rates, smaller orifice diameter is required to generate smaller bubble at the same flow rate ratios. However, the orifice diameter that can be fabricated was limited with the transparency mask resolution to 7 μm. Therefore, bubble splitting microfluidic devices were designed as well to reduce the diameter of the microbubbles generated by splitting each bubble. Each splitting reduces the diameter of each bubble only 20% and therefore at least two consecutive splittings were required to reduce the bubble diameter of 7 μm below 5 μm.

2.3.3.1 Stability and Yield

While the encapsulation efficiency of the bubbles was acceptable at around 50%, there can be seen some emulsions without any microbubbles within in Figure 20. Production rates as high as $6x10^7$ microbubbles per minute were achieved compared to commercial production of about 10^{10} bubbles per minute.

The choice of microbubble lipid shell membrane greatly affected the microbubble stability and generation. Also, trying to increase the microbubble generation by increasing the flow rate of liquid phase and/or gas phase increased the polydispersity of microbubbles by increasing the probability of coalescence and limiting lipid membrane formation. Moreover, the stability of the emulsions with microbubbles encapsulated was limited to a few hours and the number of emulsions with microbubbles encapsulated decreased significantly within an hour. In order to improve the stability of emulsions with microbubbles encapsulated different lipid shell

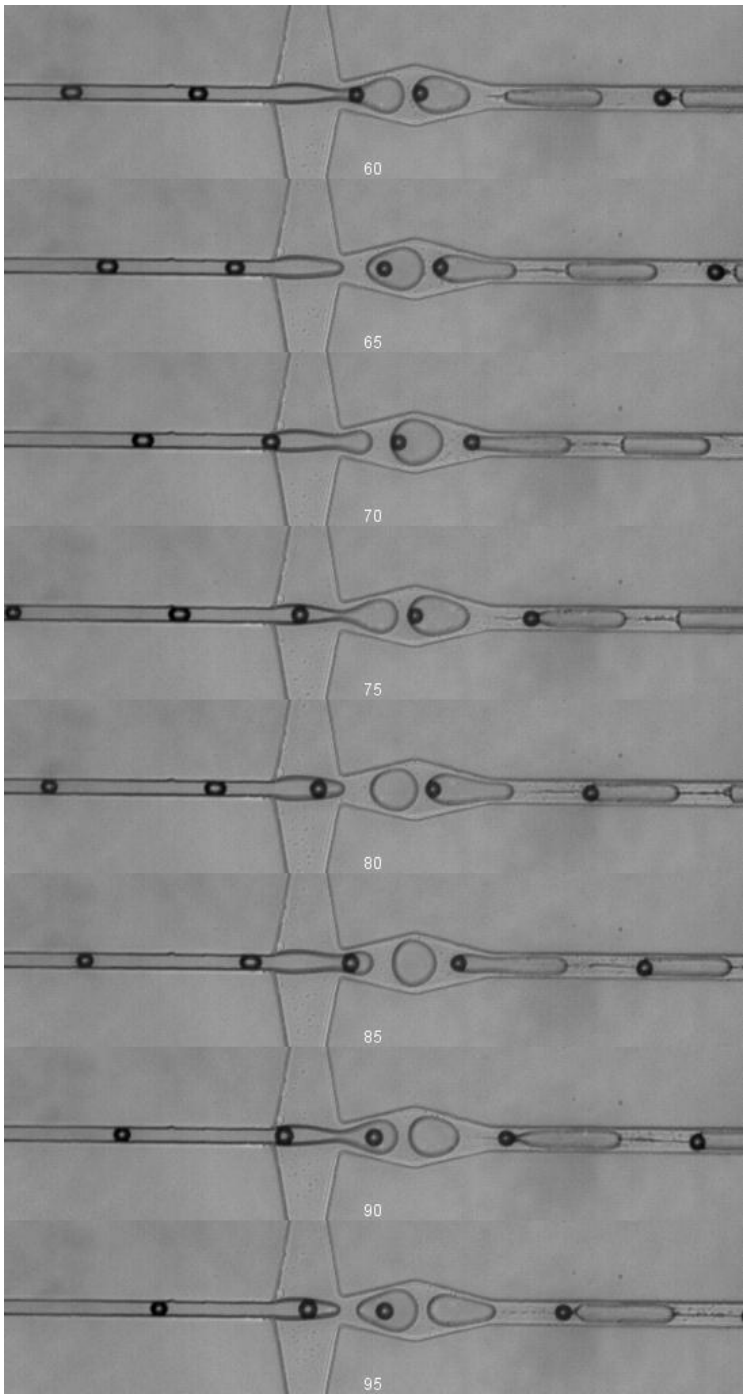

Figure 20 Sequence of high-speed images showing microbubble encapsulation

Sequence of high-speed images showing microbubbles being encapsulated in second liquid phase at the 20 μm orifice.

mixtures were tested but the overall stability of the emulsions with microbubbles didn't change much compared to the original formulation.

2.3.4 Results with Silicon-SU8 Nozzles

Initially, regular 550 μm thick wafers were etched through with 50 μm nozzle pattern. However, the etch rate was too slow at the desired anisotropic sidewall profile. Therefore, 250 μm thick wafers were etched through with 50 μm nozzle pattern. Later, it was observed that the patterns were too close to each other (Figure 21) resulting in side channels connecting, In order to improve etch rate, a new mask with 200 μm patterns separated further was used with regular 550 thick wafers and etch rates above 2.75 μm/min were achieved. However, surface roughness observed at the top of the channels was still observed even with oxygen flow rates as high as 7 Sccm. To further investigate the effect of mask materials on surface roughness 50 μm thick SU8 was patterned and used as etch mask and the result of etching is shown in Figure 22. Unlike other photoresists, the SU8 was strong enough to act as etch mask and no cracking was observed for thicknesses less than 70 μm. For thick photoresists, SU8 hard baking was observed to be essential where without hardbaking at elevated temperatures (150-200 ºC for at least 30 minutes), cracks were observed and the mismatch between the SU8 and silicon caused the detachment of SU8 from silicon wafer surface. In order to achieve nozzles with smaller holes, SU8 was used as well on the other side of the wafer, by back aligning the 200 μm patterns on the top of the wafer with the 8 μm patterns at the bottom of the wafer. The sidewall profile of the

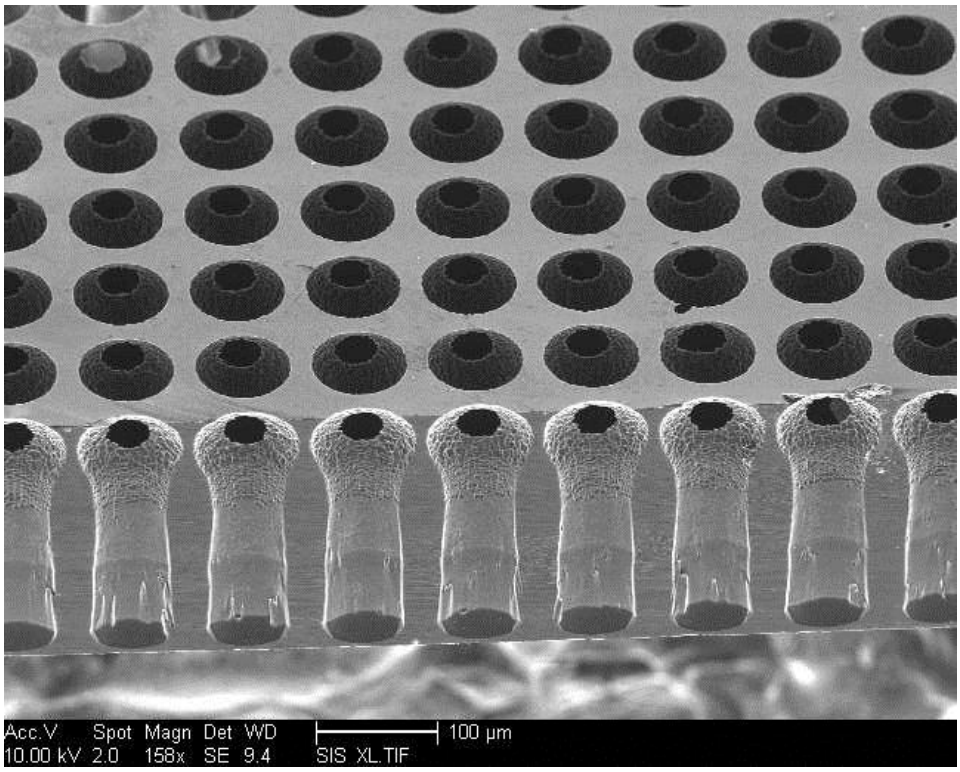

Figure 21 Silicon Nozzles with 50 µm pattern

250 µm wafers with Ti/Ni etch mask were etched through using SF_6/O_2 plasma (SF_6 = 50 Sccm, O_2 = 5.5 Sccm, Pressure = 12 mTorr, RF Power = 6 W, ICP Power = 1500 W, Temperature = -115 ºC, He = 4.5 Sccm, Time = 110 minutes)

silicon nozzles with SU8 layers on both side of the wafer is shown in the top left panel of Figure 23 and a close up with measurement is shown in the bottom left panel of the same figure. On top of improving the surface roughness, using SU8 as etch mask simplified the number of steps required to make the desired silicon nozzles in couple of ways. First, metal deposition layer and lift-off was no longer required. Second, a second etching wasn't required in order to etch through smaller patterns at the bottom of the wafer. Third, SU8 acted as etch stop layer as well and improved the etching uniformity. After the nozzle etching was completed, a thin layer of SiO_2 was deposited

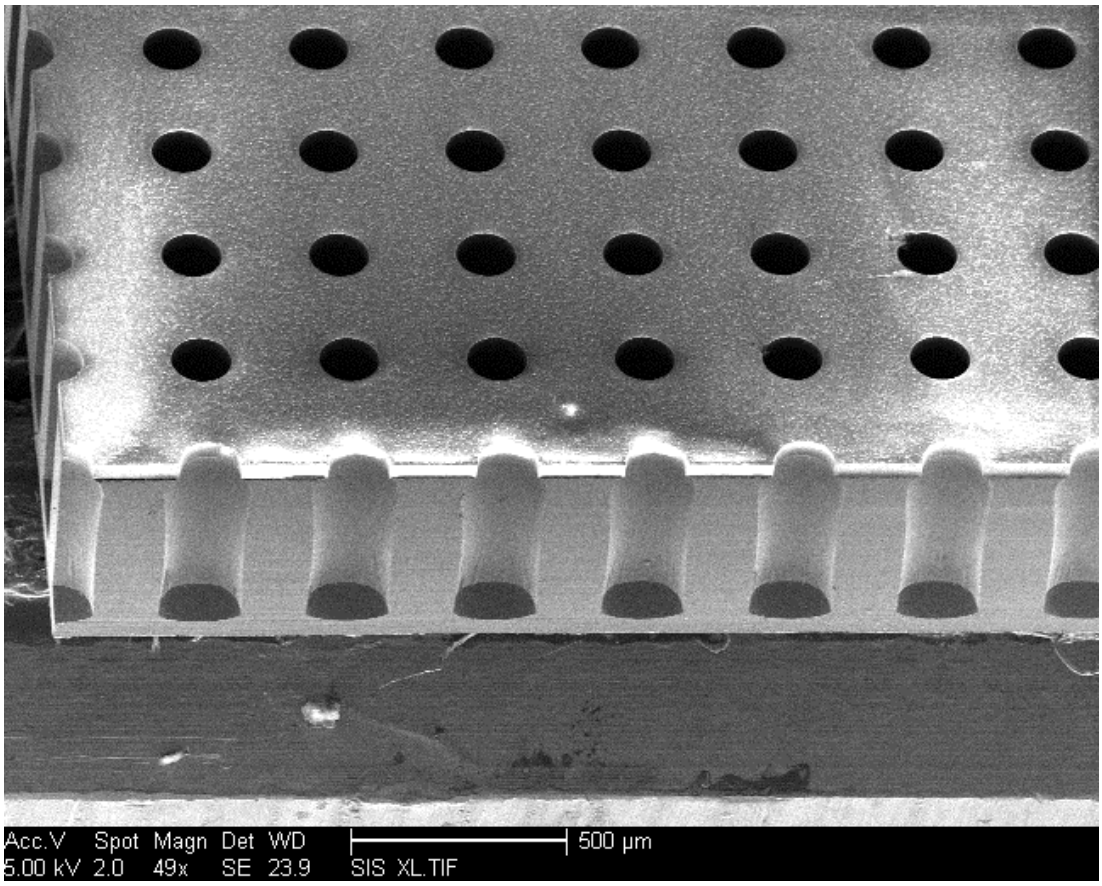

Figure 22 Silicon-SU8 nozzles with 200 µm pattern

550 µm wafers with 50 µm thick SU8 etch mask were etched through using SF_6/O_2 plasma (SF_6 = 50 Sccm, O_2 = 6 Sccm, Pressure = 12 mTorr, RF Power = 6 W, ICP Power = 1500 W, Temperature = -115 ºC, He = 3 Sccm, Time = 180 minutes)

on SU8 layers and, the nozzle was sandwiched between PDMS channels with inlets and outles punched after oxygen plasma treatment. Afterwards, the liquid and gas phases were supplied into corresponding inlets.

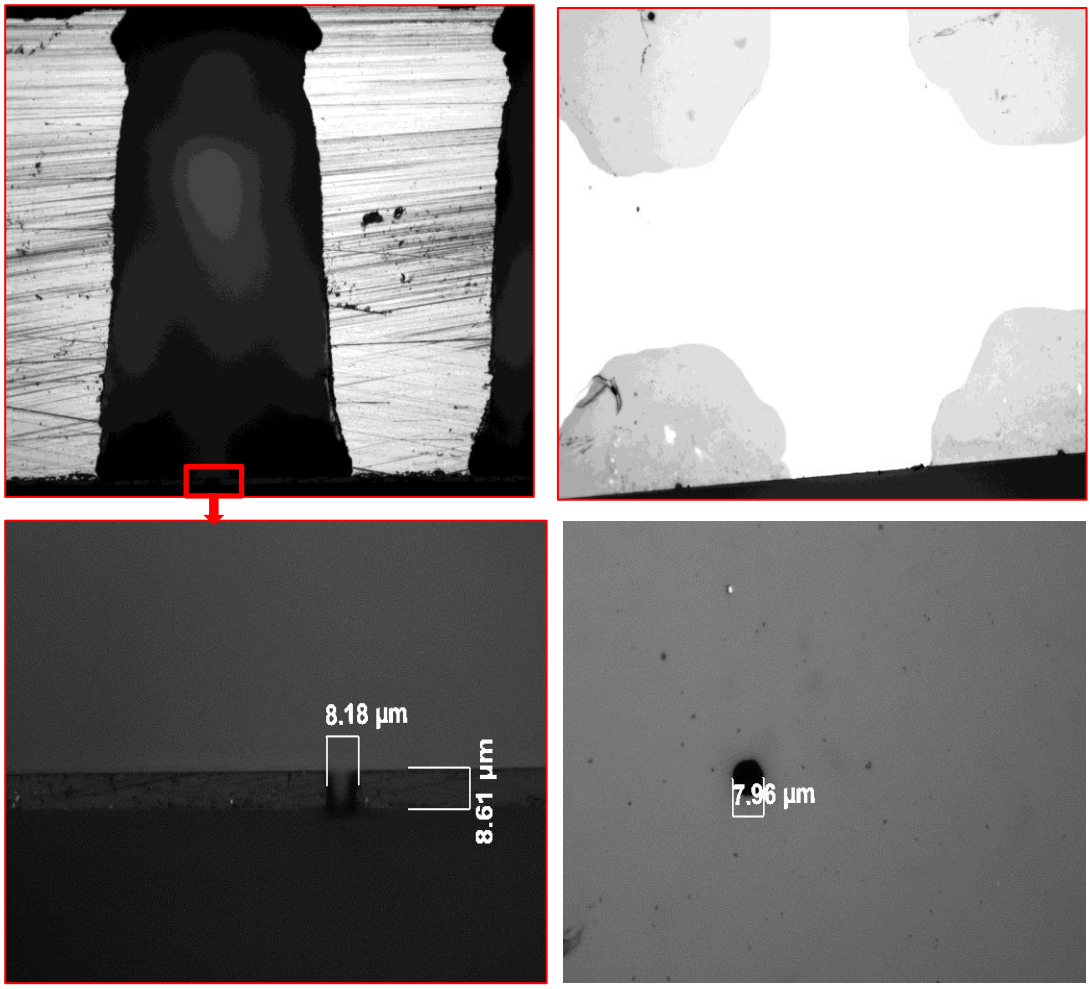

Figure 23 Silicon-SU8 Nozzles with 200 µm top pattern and 8 µm bottom pattern

550 µm wafers with 21 µm thick SU8 etch mask were etched through using SF6/O2 plasma (SF6 = 50 Sccm, O2 = 6 Sccm, Pressure = 12 mTorr, RF Power = 6 W, ICP Power = 1500 W, Temperature = -115 ºC, He = 6 Sccm, Time = 180 minutes) Top left panel shows the side profile of the channels and bottom left panel shows the close-up view of the small SU8 hole. Top right panel shows the bottom of the wafer and bottom right panel shows close-up view of the small SU8 hole at the same plane of view.

2.4 Conclusion

In this chapter, first we demonstrated the feasibility of producing SPIO based liposomal theranostic nanoplatform that can be imaged by MRI and fluorescence

microscopy. The particles were prepared using conventional liposomal preparation techniques based on lipid film formation dehydration/rehydration/sonication and extrusion. Acetylated lipids were incorporated into the lipid shell composition and UV cross-linked to enhance in vivo stability. The proposed design of the theranostic nanoplatforms were verified by various in vitro experiments. These SPIO based liposomal nanoplatforms also exhibited good loading of DOX. Moreover, their effectiveness as an MRI contrast agent was comparable or better compared to commercially available iron oxide based contrast agents. The particles were also stable at least two weeks after preparation when stored at 4 ºC.

Secondly, we demonstrated the feasibility of producing microbubble based acoustically active liposomal theranostic platforms that can be imaged by US and fluorescence microscopy. More important, these acoustically active liposomal theranostic platforms can be used for site-specific delivery of their chemotherapeutic payload by sonoporation. The particles were first prepared using microfluidic flow-focusing techniques with PDMS devices prepared using soft lithography techniques. Microbubbles with tight size distribution were generated and then were encapsulated within another liquid phase with lipid shell constituents dissolved in. Another encapsulation was planned in order to get lipid bilayer shell. Microfluidic based techniques provided good control over particle size and encapsulation. However, the stability of the emulsions with microbubbles encapsulated were limited to a few hours and the production was limited to $6x10^7$ particles per minute compared to 10^{10} microbubbles per minute achievable in typical bulk preparation methods. In order to

meet volume production requirements, another preparation method based on silicon nozzles prepared using cryogenic techniques was pursued. Silicon nozzles were prepared in the cleanroom and then were sandwiched between two PDMS channels. Next, the gas or liquid phases were introduced into the corresponding inlets and the generated particles were collected at the outlet. This particle preparation method offered good control of particle size and tight size distribution, straightforward scalability to increase production volume as well as highly efficient encapsulation.

In summary, developments of two different theranostic platforms based on different imaging modalities are investigated and their feasibility and preparation is demonstrated. These theranostic platforms have great clinical potential in cancer treatment and they can provide new opportunities in fight against cancer.

Acknowledgement:

This chapter, in part, is a reprint of the material as it appears in : A. Erten, W. Wrasidlo, M. Scadeng, S. Esener, R. Hoffman, M. Bouvet and M. Makale, “Magnetic resonance and fluorescence imaging of doxorubicin-loaded nanoparticles using a novel in vivo model”, submitted to Nanomedicine: Nanotechnology, Biology and Medicine. The dissertation/thesis author was the primary investigator and author of this paper.

3 MAGNETIC RESONANCE IMAGING (MRI) COMPATIBLE RODENT DORSAL SKINFOLD CHAMBER TEST-BED

3.1 Introduction

In 1924, the desire to study the growth and the behavior of living mammalian tissues microscopically led Sandison[124] to devise the first observation chamber implantation in the rabbit's ear. Since then, various chambers have been developed and implanted in mice[125], hamsters[126, 127], rats[128], rabbits[129] and human subjects[130] for chronic studies of the microcirculation. Specifically, the rodent dorsal skinfold window chamber, first developed in 1940s, recently has become especially useful in discovering and evaluating novel cancer therapeutics with the expansion of its implantation in nude mice[131], deficient in cell-mediated immunity, acting as hosts for human tumor cells.

With the advancements in imaging systems such as confocal and multiphoton microscopy together with the incorporation of new fluorescent cellular and intracellular markers and fluorescent probes, rodent dorsal skinfold window chambers implanted in nude mice allow repeated high-resolution imaging and study of tumor growth, angiogenesis and dynamics of interaction between tumor and therapeutic agents in a single animal over a prolonged period of time[132]. However, the window

chamber is significantly limited by the fact that it is not orthotopic for many tumors and although melanomas are, the tumors still grow in a more confined configuration than they normally would do.

Orthotopic xenograft models address the concerns about tumor's microenvironment at a cost of low-resolution imaging and/or at only one time point in the duration of the treatment or observation. Therefore, it is desirable to use orthotopic xenograft models for observing the dynamics of interaction between tumor and therapeutic agent in a single animal to avoid systematic errors if a noninvasive high resolution imaging modality could be found. One possible solution is Magnetic Resonance Imaging (MRI) of orthotopic xenograft model throughout the treatment. However, MRI relies on contrast between healthy tissues and tumor and the difference is not as obvious especially in the early stages of the tumor. The contrast can be enhanced by using contrast agents but regardless the validity of the MR and Functional MR images needs to be evaluated and verified usually by invasive surgical procedures followed by histology[133].

In this chapter, we describe a novel MR- compatible rodent dorsal skinfold window chamber test-bed which is used to provide chronic high-resolution optical imaging of tumor and therapeutic agent interaction and validate MR images in a single animal. First, we visit the history of the dorsal skinfold chamber models and its applications followed by the description of choice of material and design considerations for MRI compatible rodent dorsal skinfold window chamber test-bed.

Then we proceed with describing the implantation of chambers on subjects. Finally, we explain imaging with MRI compatible rodent dorsal skinfold chamber.

3.2 History of Dorsal Skinfold Chamber Models

The first observation chamber was implanted into the rabbit ear by Sandison in 1924 for microscopic study of living growing tissues[124]. Since then, various chambers have been developed and implanted in mice[125], hamsters[126, 127], rats[128], rabbits[129] and human subjects[130] for chronic studies of the microcirculation. Specifically in 1943, Algire was first to adapt observation chamber technique to mice for direct observation of the subcutaneous tissues and microcirculation using the longitudinal fold of dorsal skin of mice as chamber implantation site[125]. In 1969, the dorsal skinfold chamber technique was adapted to the skin folds of rats for studying microcirculation in cancer tissues[134]. In 1978, the dorsal skinfold chamber technique for the rat was further modified[135]. Later in 1980, the dorsal skinfold chamber technique was applied to hamsters for microvascular studies[127]. In 1993 the dorsal skinfold chamber was implanted on nude mice for the intravital microscopic investigation of striated skin muscle[131]. The technique comprised two metal plates supporting the dorsal skin fold, within which a circular area of skin is removed entirely and sealed by a thin cover glass kept in place by retaining rings. While the early chambers were fabricated from stainless steel, aluminum was preferred as the material used for the fabrication of chambers for its light weight. Later titanium was adapted as the material of choice for

its durability, light weight, biocompatibility and low thermal conductivity[136]. In terms of design, improvements of the dorsal skinfold chambers included the modification of the chamber design to reduce weight and enhance optical clarity.

3.3 MRI Compatible Rodent Dorsal Skinfold Chamber

Traditional rodent dorsal skinfold chambers allows high resolution noninvasive serial observation of tumor angiogenesis and interaction of tumor and therapeutic agent in single animal. However, the rodent dorsal skinfold window chamber is significantly limited with the observation of non-orthotopic tumors and this hinders the successful translation of results acquired with chamber into clinical trials. On the other hand, intravital imaging using orthotopic xenograft models lacks the chronic high resolution observation of tumor and therapeutic agent interaction. Magnetic resonance imaging can allow chronic observation in orthotopic xenograft models though the results need to be validated with invasive surgical procedures and the procedures required to validate the MR results often limits the observations to only one time point in the duration of treatment. It would be desirable to have an orthotopic xenograft model that allows noninvasive high resolution serial observation of treatment. While there is no such alternative, here we describe a MRI compatible rodent dorsal skinfold chamber, which can be used to observe the tumor and therapeutic agent interaction over a prolonged period of time using both optical imaging and MRI modalities, to bridge and cross validate the results from optical

microscopy and MRI. Once the results from both optical microscopy and MRI acquired using MRI compatible rodent dorsal skinfold chamber are cross validated, the results can be translated into orthotopic xenograft models. The early investigation and optimization of the therapeutic agent can be performed in MRI compatible rodent dorsal skinfold chamber and the MRI parameters used in the chamber can be translated into imaging of orthotopic xenograft models. In the next phase of experiments, further serial observations of treatment can be carried out in orthotopic xenograft models with MR only.

3.3.1 Material

While the early chamber were fabricated from stainless steel, later chambers were fabricated using aluminum[134], Teflon coated aluminum[127] and titanium[137] for their durability, light weight, biocompatibility and low thermal conductivity[136]. Aluminum was used in order to reduce weight and Teflon coating was used to reduce thermal conductivity and increase biocompatibility. The disadvantage of the aluminum frames was they bent out of shape, and the Teflon coating got damaged and detached over time, limiting the possibility of repeated use[138]. The use of titanium frames[137] solved all these problems associated with Teflon coated aluminum frames. However, for the chamber to be MRI compatible, a non-metal material with comparable properties needed to be used. Also the material needed to be inexpensive, readily machinable and remain rigid when machined to the necessary small thicknesses. These requirements are satisfied by a commercially available acetal resin, Delrin® also

commonly referred to as polyoxymethlyene (POM). The comparison of Delrin® with other materials used for chamber fabrication is shown in Table 6. Delrin® can be used for injection molding as well to mass produce the MR compatible dorsal skinfold chambers.

Table 6 Properties of Various Materials Used for Chamber Fabrication

Parameter	Delrin D100P[139]	Titanium 6AI-4V-ELI[140]	Aluminum 6061-T6[141]
Material Composition	Polyoxymethylene	Titanium, Aluminum,Vanadium	Al, Cr, Cu, Si, Fe
Thermal Conductivity (W/m.K)	0.29	7.3	167
Tensile Strength @ 23 ºC (MPa)	66	862	310
Tensile Strength/Density ($psi/lb/in^3$)	194.2×10^3	862.5×10^3	461.5×10^3
Biocompatible	Yes	Yes	No

3.3.2 Design and Fabrication

The MRI compatible rodent dorsal skinfold chamber is designed using SolidWorks 3D CAD Design Software to minimize local tissue trauma and extend the life of chamber for acquiring clear images while being compatible with a custom surface coil with high sensitivity to the thin tissue layer within the chamber. It consists of two complementary Delrin® frames – front frame and back frame -, each with a 12 mm diameter opening, 8 plastic screws, a Delrin® retaining ring and two Delrin®

fastening clips (Campus Research Machine Shop at University of California, San Diego). Unlike previous dorsal skinfold chamber designs shown in Figure 24 [135], the two complimentary frames are not identical and there is no ring for attachment of the glass coverslip. Diagrammatic view of front frame of MRI compatible rodent dorsal skinfold chamber is shown in Figure 25 and the back frame is shown in Figure 26. The chamber assembly with fastening clips inserted is shown in Figure 27. The bottom of the both front and back frame is angled to prevent the implanted chamber from tilting aside and permit the chamber rest comfortably on the subject's back. The three big holes in the angled flanges serve to reduce the weight and allow air circulation. The rectangular grooves on left and right side of each frame are for fastening clips to secure the chamber on the subject. The three wings on the top border of each frame are

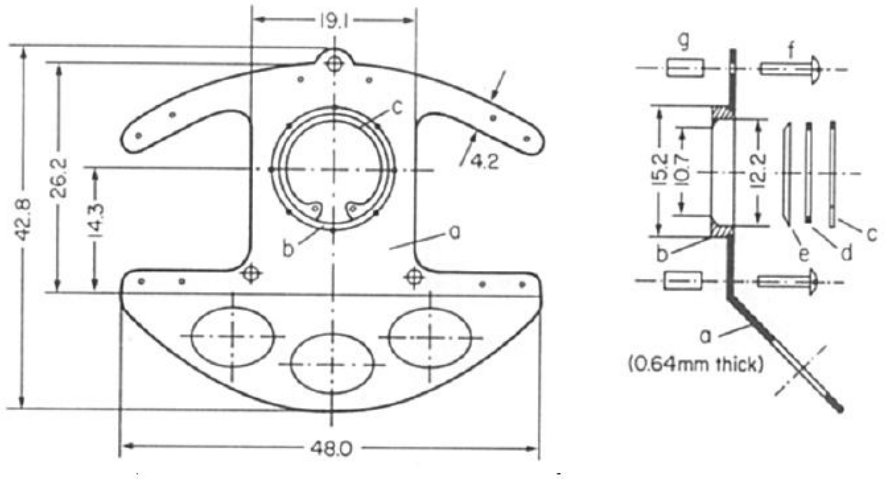

Figure 24 Diagrammatic view of aluminum chamber for the rat dorsal skinfold

Dimensions are in millimeters. a = plate (aluminum); b = collar (aluminum); c = retaining ring (stainless steel); d = spacer (Teflon); e = cover glass; f = threaded bolt (stainless steel); g = threaded spacer (stainless steel)[135].

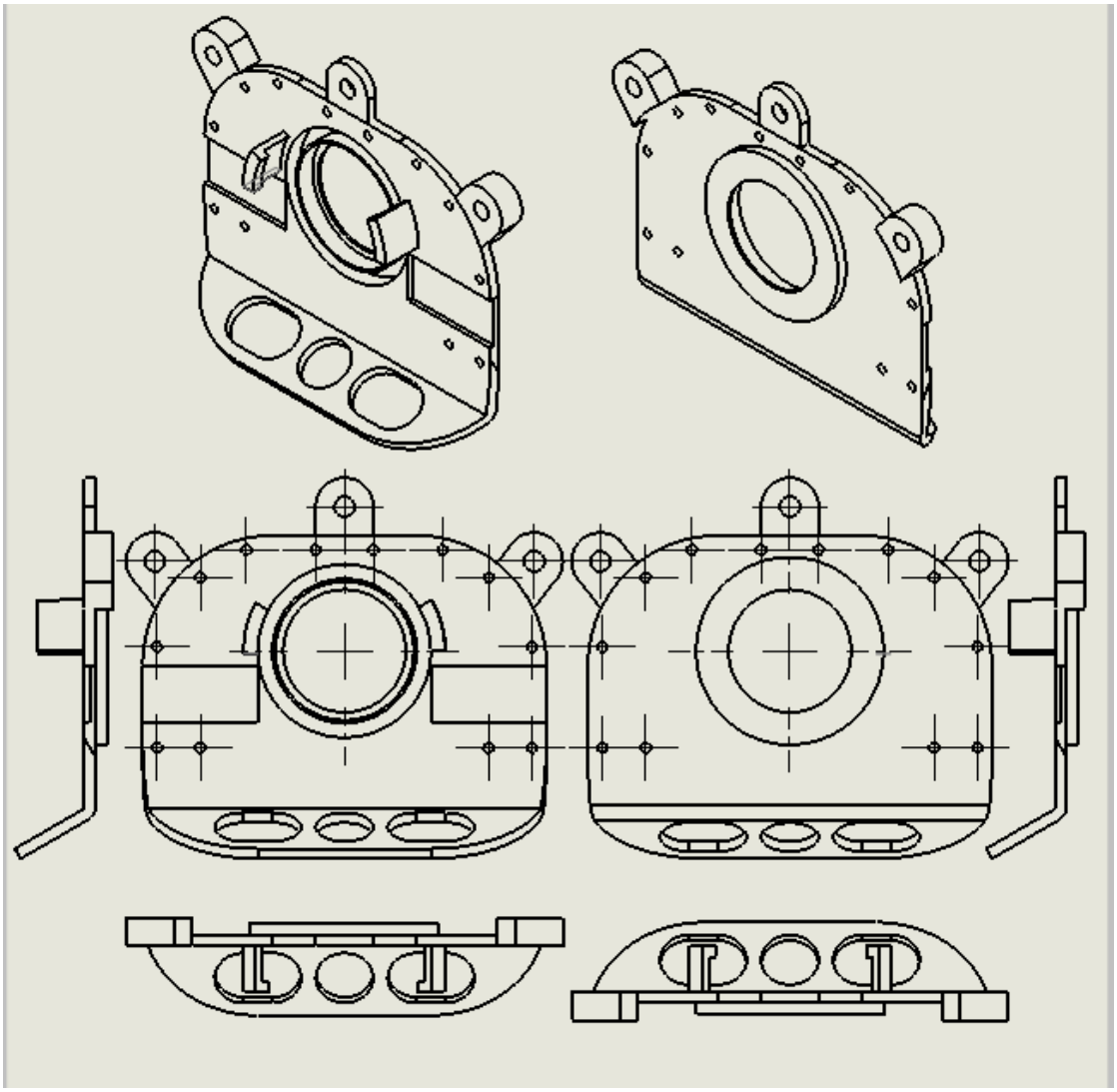

Figure 25 Diagrammatic view of front frame of MRI compatible Delrin chamber for nude mice dorsal skinfold

Side facing the skin is shown from different viewpoints on the right half and side facing away from skin is shown from different viewpoints on the left half.

Threaded for matching plastic screws and together they hold the frames together and supplement the fastening clips. The two side wings of the front frame are 2.54 mm thick and serve as spacer as well which is adapted to the thickness of the skin of nude

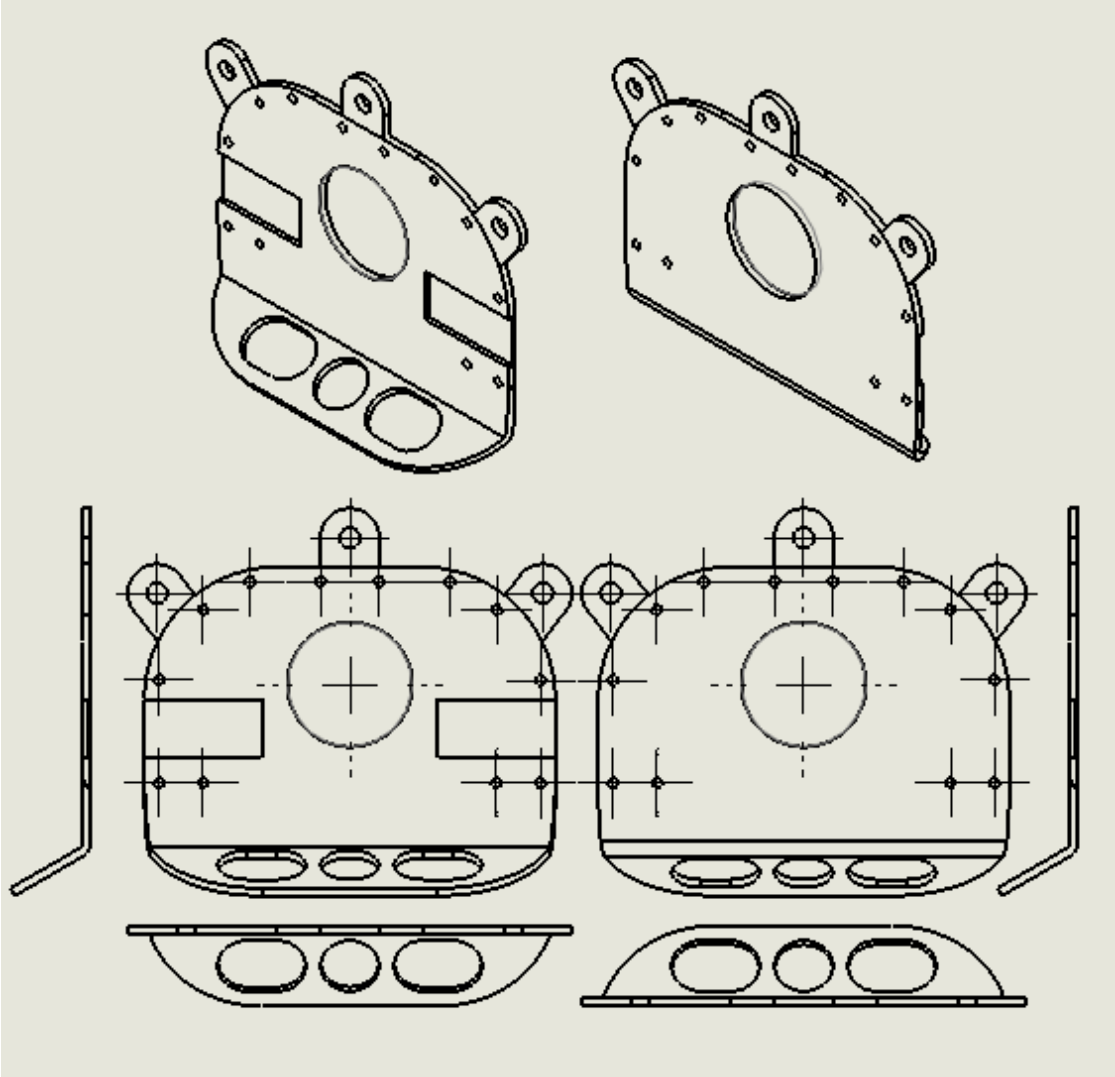

Figure 26 Diagrammatic view of back frame of MRI compatible Delrin chamber for nude mice dorsal skinfold

Side facing the skin is shown from different viewpoints on the right half and side facing away from skin is shown from different viewpoints on the left half.

mice. 12 suture holes are provided on the border of each frame as well to attach the outer margin of the skinfold to the top edge of the chamber frames. The three wings coupled with screws and two fastening clips together replace the bolts penetrating the

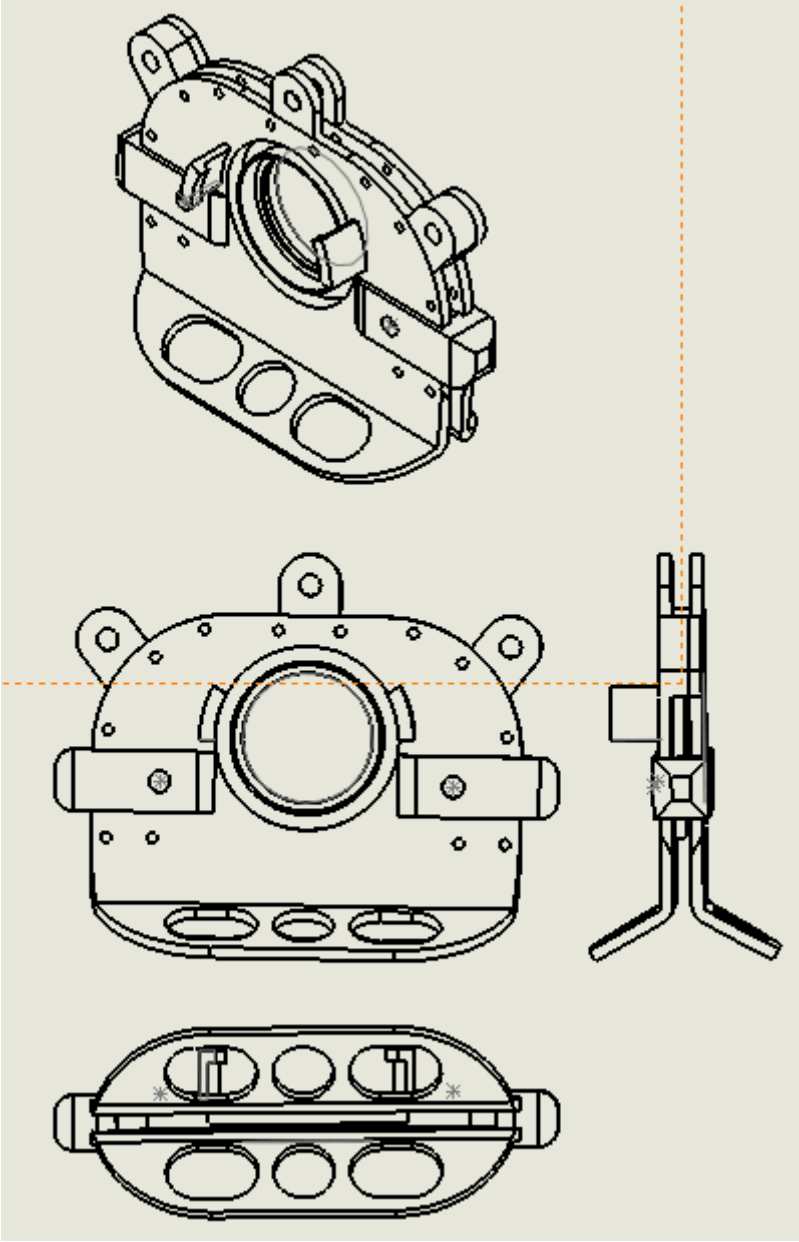

Figure 27 Diagrammatic view of MRI compatible Delrin chamber assembly for nude mice dorsal skinfold

The MRI compatible Delrin chamber assembly with fastening clips inserted is shown from different viewpoints.

skin used in old chamber designs[135] to minimize local tissue trauma, a key feature to extend the life of chamber for getting clear images. The wings are also used to secure the chamber to a holder that restrained the subject, and fixed the chamber to the holder for light microscope imaging.

The front frame itself is 1mm thick except for the 16.5 mm wide round bed in the center designed to house glass coverslip and custom surface coil. This round bed is designed to replace the collar used in previous dorsal skinfold chambers is 2.03 mm thick and the glass coverslip rests on a 0.25 mm thick lip. The glass coverslip is retained inside this inner groove with a 1 mm thick Delrin® ring. The outer groove inside the round bed is separated from the glass coverslip with a 0.50 mm thick wall and has a diameter of 15.24 mm and has a width of 2.54 mm. This outer groove together with two 4.06 mm tall prongs keeps the custom surface coil close and secure on top of the tissue of interest within the chamber. The back frame itself is only 0.76 mm thick and is plain except the center opening and the rectangular grooves on the left and right side of the frame.

The fastening clips are designed to have a built in spacer as well to avoid tissue compression and restriction of blood flow and are kept in place with a pair of screws inside the rectangular grooves on left and right side of the frames. The custom surface coil is designed to fit into the outer groove on the front frame snugly and it locks in place in only one direction to improve the repeatability of the results and imaging.

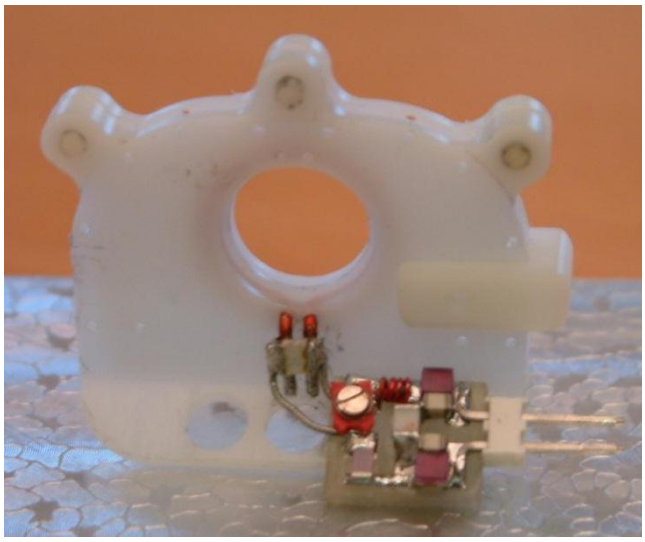

Figure 28 Front frame of MRI compatible Delrin chamber for nude mice dorsal skinfold with built in surface coil

In the early versions of our MRI compatible rodent dorsal skinfold chamber shown in Figure 28, a built in surface coil was used. However, the exposure of the circuitry to the bodily fluids and cleaning chemicals affected the MR imaging results adversely. On top of these aforementioned problems, the imaging of multiple subjects required the design and installation of individual surface coils for each chamber and added another variable into the imaging results. In the current design of our MRI compatible rodent dorsal skinfold chamber shown in Figure 29, the surface coil is removable and is attached on the chamber only during the MR imaging. With this new approach, it is possible to image multiple subjects with the same surface coil allowing multiple experiments being carried out in parallel while reducing the weight of chamber carried by mice.

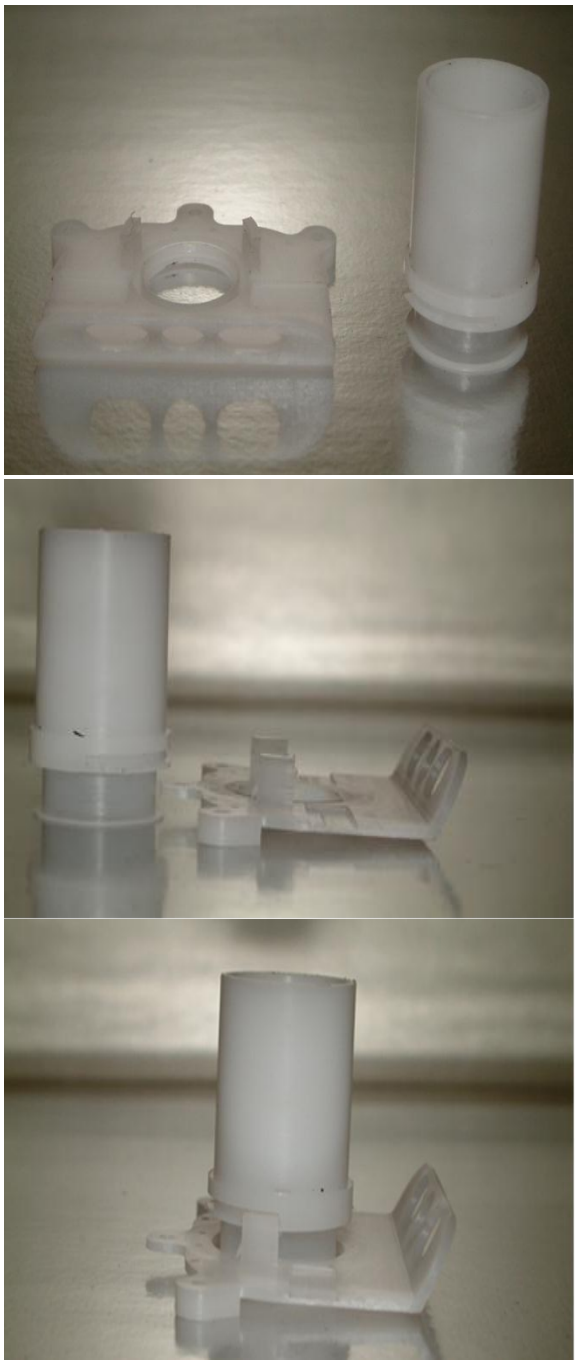

Figure 29 Front frame of MRI compatible Delrin chamber for nude mice dorsal skinfold with Delrin custom surface coil holder

Front frame next to custom surface coil holder is pictured next to each other on top and middle images from different viewpoints. Front frame attached to the custom surface coil holder is pictured in the bottom image.

3.3.3 Surgery

The entire dorsal skinfold chamber assembly is disassembled and placed in a solution of ethanol for about 24h. The glass coverslip is discarded, and the chamber is carefully scrubbed in distilled water and laboratory-grade soap. The chamber frames and associated parts are rinsed in double-distilled water and then placed in an ultrasonic cleaner with double-distilled water and laboratory-grade soap for 45 minutes. After ultrasonic cleaning, the parts are rinsed in double-distilled water and then placed in a sterile biological hood under the ultraviolet light for about 24h. Glass coverslips are soaked in 0.23% peracetic acid and 7.35% hydrogen peroxide for 2h, rinsed in 70% ethanol. Finally the dorsal skinfold chamber is assembled without coverslip and retaining rings, and then placed in autoclave pouches. The coverslips, Teflon screws and retaining rings are wrapped in cotton gauze and placed in separate autoclave pouches. All the chamber materials are then autoclaved.

All animal protocols used in this study were evaluated and approved by the University of California San Diego IACUC committee. All protocols were strictly followed, aseptic surgical techniques were used, and the mice treated humanely according to the NIH guidelines for the care and use of laboratory animals. Every effort was made to ensure that the mice were as comfortable as possible.

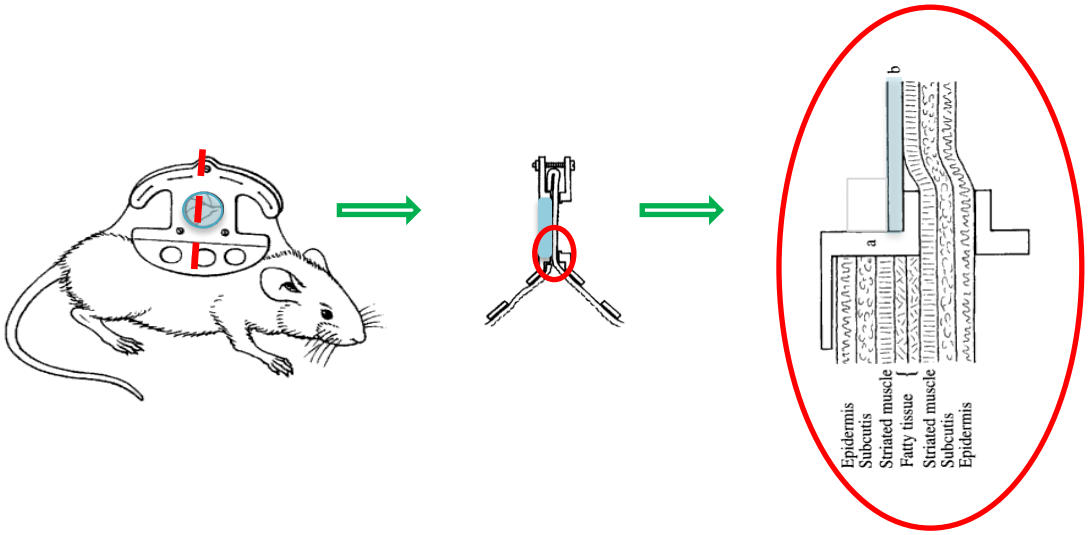

Figure 30 Schematic of a mouse fitted with a dorsal skinfold chamber

Schematic of a mouse fitted with dorsal skinfold chamber is shown on the left. Cross-sectional view of a mounted skinfold chamber is shown in the middle. High magnification cross-sectional view of a mounted skinfold chamber is shown on the right.[142]

Before the surgery, the nude mice are checked for overall health status and then are anesthetized by subcutaneous injections of 100mg/kg of ketamine and 250 to 500 mcg/kg of medetomidine. The dorsum is then washed with saline and Betadine antiseptic is applied. The back is then cleaned with 70% ethanol swabs. Then the animal placed on heated pad covered by a clean surgical drape is placed on a Plexiglas surgery stand. The dorsal skin is elevated into a longitudinal fold and transilluminated to allow mirror-imaged positioning of the major blood vessels of the sandwiched skinfold. The back frame is sutured on the back side of the sandwiched skinfold. Although the diameter of the observation window is about 12 mm, a disc of skin about 14 mm in diameter is removed in order to avoid compression of tissue after

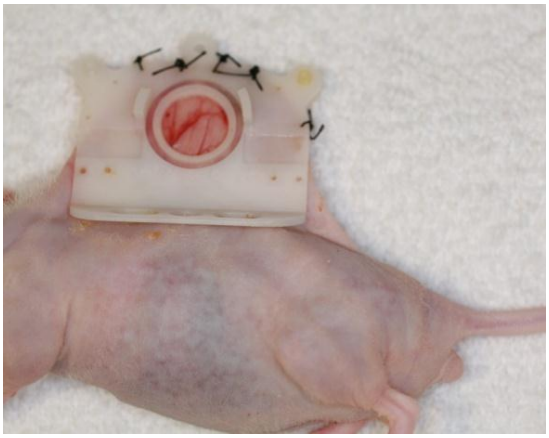

Figure 31 Picture of MRI compatible dorsal skinfold chamber implanted on nude mouse

MR compatible dorsal skinfold chamber without fastening clips is shown implanted on nude mouse. The fastening clips are removed to show the skinfold more clearly.

implantation of the front frame. This also limits the development of granulation tissue during the post-surgery observation period[138]. Then underlying fat, fascia is removed. The exposed retractor muscle is cut back and reflected over the external skin and glued to the skin using small drops of veterinary bonding cement. The skin surrounding the exposed tissue is coated with topical antibiotic ointment. The front frame is sutured on the exposed side of the skinfold and a sterile 12 mm diameter glass coverslip is placed over the exposed tissue. The fastening clips are attached and screwed on to keep the frame-to-frame distance of 1.5 mm. This distance guarantees the healthy circulation in supplying arterioles and the draining venules.

The schematic of mouse fitted with a dorsal skinfold chamber is shown on the left in Figure 30 and a cross sectional view of a mounted skinfold and a high

magnification cross sectional view of mounted skin fold chamber is shown in the middle and on the right of Figure 30 respectively. The picture of MR compatible dorsal skinfold chamber without fastening clips implanted on nude mouse at the end of the surgery is shown in Figure 31.

3.3.4 Post-Surgery

After the surgery, the mice are kept in separate autoclaved microisolator cages gently warmed to prevent other animals from damaging window chambers and allowed to recover under direct supervision, received buprenorphine subcutaneously for analgesia, and were provided sulfamethazine antibiotic in their drinking water. The animals are monitored daily and chamber implantation sites are checked for inflammation and infection.

The following criteria is used for determination of successful dorsal skinfold chamber implantations: The rodent skinfold chamber should remain clear and free of discoloration, microhemorrhages and opacity for it to be suitable for observation[143]. There shouldn't be any air bubbles in the observation window, and the tissue should appear to be very close to the glass coverslip[136]. When examined at 10x optical objective, the perfusion of the microvasculature should be apparent and uniform.

An occasional problem of a dark-green color along the chamber tissue periphery in nude mice dorsal skinfold implantation is a sign of fungal infection and should be addressed with controlling the sterility of conditions and proper use of antibiotics. The tilting of the chamber implantation on one side is expected and does

not pose a problem. In cases of successful dorsal skinfold chamber implantation, the animals tolerated the chambers well and didn't show any sign of discomfort evidenced by no effect on their sleeping and feeding habits.

3.3.5 Preparation and Implantation of Tumor Cells

Typically Lewis Lung Carcinoma (LLC) cell lines and human pancreatic carcinoma cell lines (FG) are cultured in 5% CO_2 at 37ºC in 100 mm tissue culture dishes. FG cell lines are cultured in Minimal Eagles Medium (MEM) to which 10% fetal bovine serum (FBS), L-glutamine 1:100 (200 mM stock), antibiotics (10,000 IU penicillin, 10,000 μg/ml streptomycin, 25 μg/ml amphotericin) is added[136]. LLC cell lines are cultured using Dulbecco modified Eagle medium (DMEM) with 10% fetal calf serum (FCS), 1% penicillin and streptomycin[144, 145]. The tumor cell lines are transfected to express Discosoma sp. Red fluorescent protein (DsRed) or green fluorescent protein (GFP). Once the cells reach 80% confluency, they are prepared for implantation. First, they are washed with sterile phosphate buffered saline (PBS), and then are treated with trypsin for about 2 minutes at 37ºC. Following the trypsin treatment, they are washed off the dishes with medium, and then are centrifuged for about 5 minutes at 3000 rpm. The resultant pellet is resuspended in PBS, and the cell density is counted with a hemocytometer. The final pellet is resuspended in PBS at a concentration of 200,000 cells/μl.

After 1 to 2 days of recovery time, subject with successful chamber implantation is secured in transparent mouse cylinder and then attached to the custom

mouse holder shown in Figure 35. Next, the subject is lightly anesthetized by subcutaneous injections of 100mg/kg of ketamine and 250 to 500 mcg/kg of medetomidine. The glass coverslip is removed from the chamber, and an autoclaved 25 µl glass gas-tight syringe is used to inject 5 µl of tumor cell suspension (about 1,000,000 cells) prepared as described in the previous section into the outer portion of the retractor muscle, between two major vessels near the top of the window. The chamber is sealed with a fresh, sterile glass coverslip and attention is paid to avoid and expel air bubbles within the chamber. The subject is removed from the mouse cylinder and returned to its cage to recover.

3.3.6 Imaging

Magnetic resonance (MR) images of rodent dorsal skinfold chamber implantations are acquired on a 3T clinical system (General Electric) or a 7T 21 cm bore small animal system (Bruker Avance II). Before acquiring MR images on 3T clinical system, the animals are anesthetized with 50 mg/kg ketamine plus 125 mcg/kg medetomidine in order to minimize motion artifacts during the acquisition of the images. The MR image of the tissue within the rodent dorsal skinfold chamber implantation acquired using a T_1 weighted 2D Fast Spin Echo sequence (field of view = 2.6 cm, Mx = 256x256, TR = 550 ms, TE = 17 ms, ETL = 2, BW = 31.25 kHz, Slice Thickness = 1 mm, Acquisition Time = 4 min 42 sec) with custom removable RF coil on this 3T clinical system is shown in Figure 32 next to corresponding optical image of the same chamber implantation. The MR image of the chamber with pancreatic

cancer (FG) tumor grown within acquired using 3D TRICKS pulse sequence (field of view = 2.6 cm, Mx = 126x96, TR = 16.6 ms, TE = 4.3 μs, BW = 10.7 kHz, Slice Thickness = 0.8 mm) before and after contrast agent Gadolinium injection via tail-vein with custom removable RF coil on 3T clinical system is shown in Figure 33 next to the optical

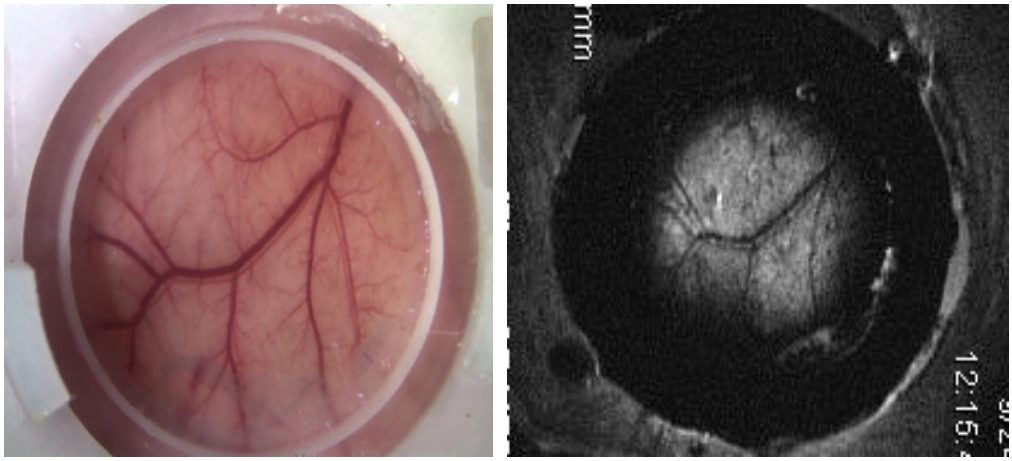

Figure 32 Comparison of MR images acquired on 3T clinical system (General Electric) vs. Optical image

The optical image acquired with epi-illumination is shown on the left. The MR image acquired on 3T clinical system (General Elecric) using T1 weighted 2D Fast Spin Echo sequence (FOV = 2.6 cm, Mx = 256x256, TR = 550 ms, TE = 17 ms, ETL = 2, BW = 31.25 kHz, Slice Thickness = 1 mm, Acquisition Time = 4 min 42 sec) is shown on the right.

image of the same chamber. For acquiring MR images on 7T small animal scanner, the animals are anesthetized with 1.5% isoflurane and placed within the holding cradle shown in Figure 34. The MR image of the tissue within the rodent dorsal skinfold chamber implantation is acquired using T2 weighted RARE sequence (field of view =

2.5 mm, Mx = 256x256, TR = 7151 ms, TE = 56.7 ms, Slice Thickness = 1.5 mm) with surface coil on 7T small animal imaging system.

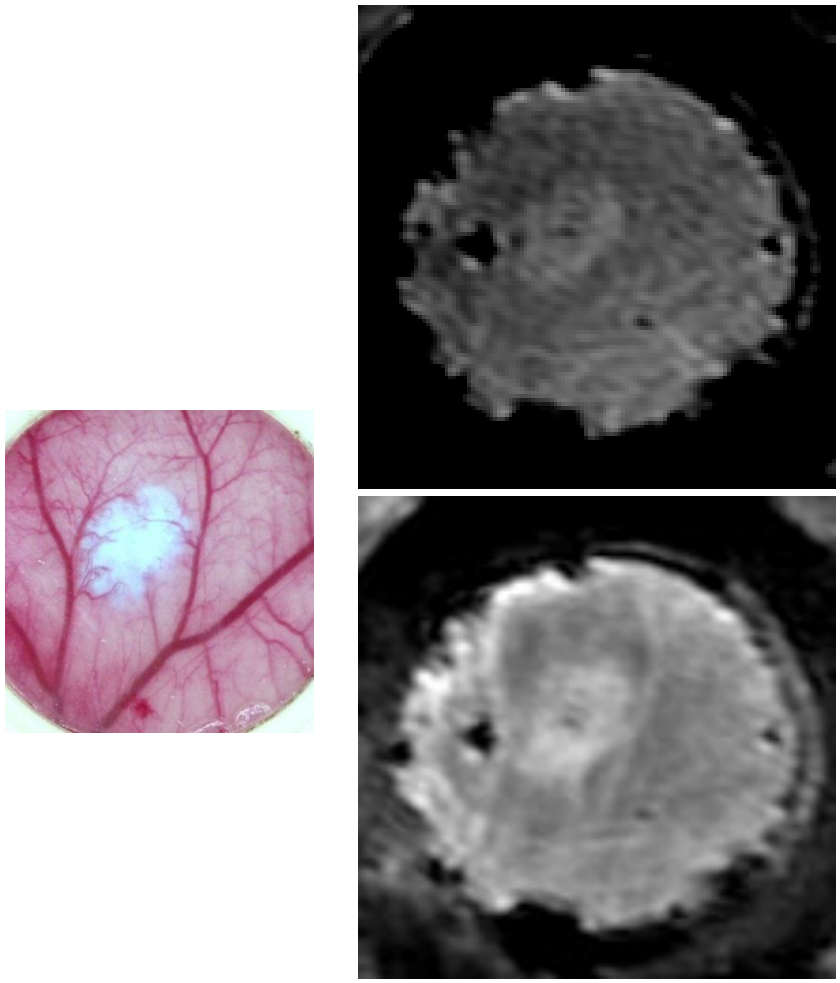

Figure 33 Comparison of MR images of chamber with tumor acquired on 3T clinical system (General Electric) vs. Optical image

The optical image blended with fluorescence image acquired with epi-illumination is shown on the left. The MR image acquired on 3T clinical system (General Electric) using 3D TRICKS pulse sequence (field of view = 2.6 cm, Mx = 126x96, TR = 16.6 ms, TE = 4.3 μs, BW = 10.7 kHz, Slice Thickness = 0.8 mm) before contrast agent Gadolinium injection is shown on top right and after contrast agent injection is shown on the bottom right.

In order to validate the MRI findings, animals are injected intramuscularly with 20 mg/kg Nembutal alone, 20 mg/kg Nembutal plus 125 mcg/kg medetomidine or 50 mg/kg ketamine plus 125 mcg/kg medetomidine in order to minimize movement of the animal during the imaging and imaged with standard brightfield – fluorescence microscope and laser scanning two-photon microscope. For imaging the mouse is

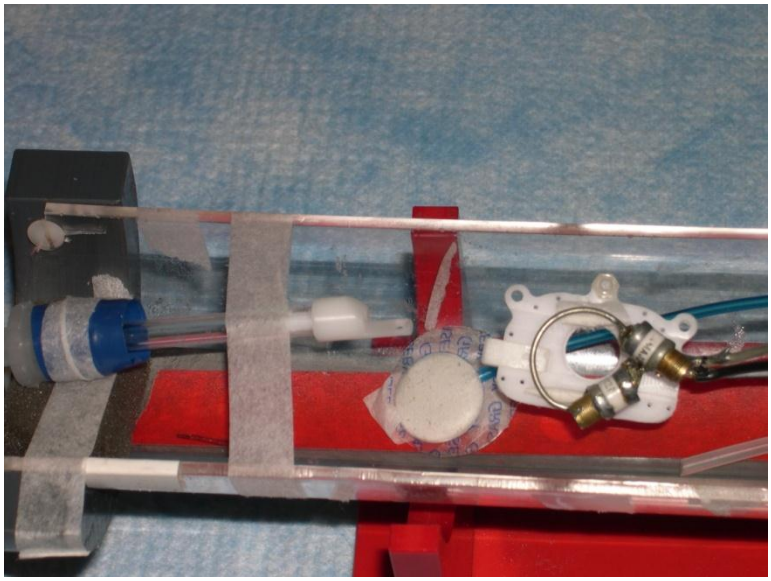

Figure 34 Surface coil and mouse holder used for 7T small animal system (Bruker Biospin)

The tunable RF coil is placed against the window chamber as depicted in the photograph. The tubing bundle at the left contains lines for delivery of isoflurane and evacuation of exhaled gases. The sensor right beneath the chamber permits respiration to be monitored during the image acquisition.

secured within a clear, perforated Plexiglass cylinder with a slit to accommodate the window chamber assembly. Next, the cylinder with the mouse is placed within a custom made Plexiglass holder that rests within the stage frame of the microscope.

The mouse cylinder fits into a trench and the chamber screw that is going through the middle wing of the frame is secured to the steel plate on the Plexiglass holder with nut in order to minimize breathing-induced movement. Mouse holder with mouse cylinder attached within stage frame is shown in Figure 35. For contrast enhancement of the intravascular space, various fluorescent markers such as fluorescein isothiocyanate (FITC) labeled dextran, FITC-lectin, FITC-rhodamine are injected via tail vein. When

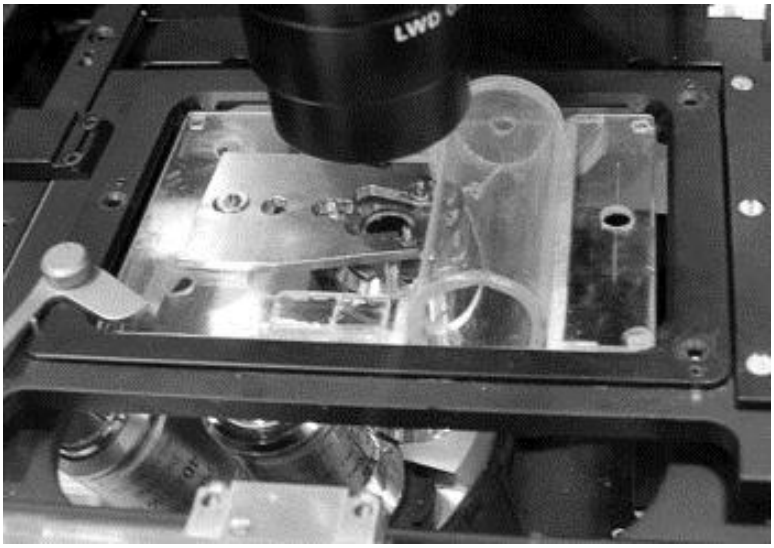

Figure 35 Picture of custom mouse holder with mouse cylinder attached within microscope stage

Plexiglass mouse cylinder attached to the custom mouse holder is pictured within the microscope stage[136].

using multiple fluorescent markers, those that are well separated in emission spectra are chosen to reduce cross-talk.

3.4 Conclusion

In this chapter an MRI compatible rodent dorsal skinfold chamber test-bed designed and used to observe the tumor and therapeutic agent interaction over a prolonged period of time using both optical and MR imaging is described. MRI compatible dorsal skinfold chamber test-bed enables the successful translation of results acquired and cross validated from both optical microscopy and MRI into orthotopic xenograft models. The early investigation and optimization of the therapeutic agent and imaging parameters can be performed in MRI compatible rodent dorsal skinfold chamber and the MRI parameters used in the chamber can be translated into further studies with orthotopic xenograft models. Moreover, by doing so this MRI compatible rodent dorsal skinfold chamber test-bed also aids in the reduction of cost associated with theranostic agent development as well as in the acceleration of the development. In the next phase of experiments, further serial observations of treatment can be carried out in orthotopic xenograft models with MR only.

4 INTRAVITAL IMAGING OF THERANOSTIC NANOPLATFORMS FOR CANCER

4.1 Introduction

In vitro assays have the advantages of being low cost, relatively easy to prepare and easy to examine and image with high resolution for the effects of therapeutic agents. However, while in vitro assays address the pharmacodynamics of the therapeutic agents in a controlled environment, there are fundamental limitations in all in vitro assays that arise from their failure to take into account and/or successfully simulate critical matters such as cell-cell interactions, bioavailability and complex in vivo pharmacodynamics and pharmacokinetics of the therapeutic agents[132]. Moreover, these in vitro assays can lead to erroneous conclusions. In vitro assays are acceptable low cost alternatives for initial proof of concept studies before working on more laborious and costly in vivo models. Though, the results from these in vitro assays still need to be validated with in vivo models especially results pertaining to complicated cases such as interaction between tumor and the therapeutic agents. A good in vivo model candidate for observing the dynamics of interaction between tumor and the therapeutic agent along the duration of treatment with ease and high resolution is dorsal skinfold chamber model. Even though, the dorsal skinfold chamber model is mostly limited with observation of non-orthotopic tumors, there are

no orthotopic xenograft models that allow chronic high resolution observation of tumor and therapeutic agent interaction and the use of MR imaging doesn't change the acute nature of these orthotopic xenograft models.

MRI compatible rodent dorsal skinfold chamber model can be used to simplify and accelerate the development of theranostic nanoplatforms for cancer as it allows the combination and cross validation of the results from optical microscopy and MRI throughout the treatment in a single animal and then the results can be translated into orthotopic xenograft models. In orthotopic xenograft models, usually a separate animal needs to be used for observation of each time point in the duration of the treatment and this greatly increases the cost, duration and complexity of the studies. Furthermore, ortthotopic xenograft models are susceptible to systematic errors due to variance between subjects used for the studies. Once the early investigation and optimization of the therapeutic agent is performed in MRI compatible rodent dorsal skinfold chamber, the MRI parameters used in the chamber can be translated in to imaging of orthotopic xenograft models. In the next phase of experiments, further serial observations of treatment can be carried out in orthotopic xenograft models with MR only.

In this chapter, first we briefly describe the imaging techniques chosen for imaging of theranostic nanoplatforms and then we explain how theranostic nanoplatforms are imaged in MRI compatible rodent dorsal skinfold window chamber. Next, we explain how the results affected the development of the theranostic nanoplatform. Finally, we talk about the imaging of theranostic nanoplatforms in

orthotopic xenograft models and successful translation of rodent dorsal skinfold window chamber results.

4.2 Imaging Of Theranostic Nanoplatforms for Cancer

Nanoplatforms have become an important field of research to diagnose and treat cancer[146, 147]. Especially with new nanomedicine paradigm, highly integrated theranostic nanoplatforms that incorporate multiple functions such as imaging and therapy hold considerable promise in early detection and simultaneous monitoring and treatment of cancer with minimal toxicity[6]. Imaging can aid in tracking nanoparticles systemically, pre-validating appropriate targeting, facilitating external activation and release of therapeutic payload and providing real-time information on tumor response.

Currently, imaging methods such as positron emission tomography (PET) and single photon emission computed tomography (SPECT) offer greater sensitivity compared with other modalities, such as computed tomography (CT), magnetic resonance imaging (MRI) and ultrasound (US). However, CT and especially MRI provide higher-resolution images with anatomical resolution and soft-tissue contrast[6]. Therefore, multimodality imaging is desirable to combine complimentary information from different imaging modalities. We have chosen MRI for its superior soft tissue contrast and anatomical resolution as well as its ability to acquire whole body images within reasonable time frame. Besides with MRI, deep tissue imaging is possible unlike US and optical imaging and subjects are not exposed to radiation during

imaging unlike CT. Next, for validation of MRI results and provide complimentary information we have chosen fluorescence microscopy for its superior resolution compared with other modalities. Though the fluorescence intravital microscopy is not feasible for deep tissue imaging, MRI compatible dorsal skinfold chamber test-bed provided us with the opportunity to take advantage of superior resolution and contrast provided by fluorescence intravital microscopy. Overview of some imaging techniques mentioned is listed in Table 7.

Table 7 Overview of Imaging Systems[148]

Technique	Resolution	Depth	Time	Main small-animal use
MRI	10-100 µm	No limit	Minutes to hours	Versatile imaging modality with high soft tissue contrast
CT	50 µm	No limit	Minutes	Imaging lungs and bone
US	50 µm	cm	Seconds to minutes	Vascular and interventional imaging
PET	1-2 mm	No limit	Minutes to hours	Versatile imaging modality with many tracers
SPECT	1-2 mm	No limit	Minutes to hours	Imaging labeled antibodies, proteins and peptides
Intravital Microscopy	1 µm	<400-800µm	Seconds to hours	All of the above at higher resolution but limited depths and coverage

4.2.1 Magnetic Resonance Imaging (MRI)

Magnetic resonance imaging (MRI) or nuclear magnetic resonance imaging (NMRI) is a noninvasive medical imaging technique used to visualize internal structure and some functions of the body. The MRI employs magnetic fields together with radiofrequency (RF) radiation to produce high-quality images of the human anatomy unlike other imaging modalities which employs harmful dyes or X-rays. Especially, its superior soft tissue contrast without using ionizing radiation compared to CT combined with available contrast agents and the ability to acquire image slices from any part of the body in any direction makes it a technique of first choice in a wide range of clinical problems from joint disorders to defining the extent of tumors.

4.2.1.1 History and Principles of MRI

MRI is based on a physics phenomenon called nuclear magnetic resonance (NMR) in which if a collection of protons in a magnetic field is exposed to an oscillating RF field at their precessional frequency, resonant effect occurs[149]. In 1946 Felix Bloch from Stanford University and Edward Purcell from Harvard University described independently the NMR effect for which they received the Nobel Prize in 1952. Up until 1970s MRI was used for chemical and physical analysis. In 1971, Raymond Damadian, a medical doctor and research scientist, discovered that relaxation times of cancerous tissue and healthy tissues differ, motivating scientist to use MRI for medical diagnosis. Later in 1974 he was granted the first patent issued in the field of MRI. The first MRI equipment in health became available in the beginning

of the 1980s. The first application of MRI was in nervous system in 1980 [150] but now the method is widely applied throughout the body. In 2003 Peter Mansfield, and Paul Lauterbar shared the Nobel Prize in Physiology or Medicine. Peter Mansfield is credited with showing how the radio signals from MRI can be mathematically analyzed and interpreted into a useful image as well as how fast imaging could be possible by developing echo-planar imaging[151]. Paul Lauterbar is credited with idea of introducing the gradients in the magnetic field which allows two-dimensional pictures to be produced. The cutaway of a typical modern MRI machine is shown in Figure 36.

Magnetic resonance refers to the phenomenon whereby the nuclei of certain atoms, which have an odd number of protons and so possess a net charge, absorb and emit energy at a specific frequency called Larmor frequency for the particular nuclei when placed in a magnetic field[149]. When the protons of particular nuclei are placed in a strong uniform magnetic field, they align parallel with the direction of the magnetic field and a net magnetization in the direction of the field is observed. However, since the nuclei are spinning as well, they don't just align with the direction of the magnetic field but rather precess about the external field at Larmor frequency. The frequency of rotation is expressed by Larmor relation:

$$f = \gamma \boldsymbol{B}$$

where $\boldsymbol{B}$ is the magnetic field strength and γ is the Larmor constant also known as "gyromagnetic ratio" or " magnetogyric ratio". For Hydrogen nuclei which are commonly used for imaging for their abundance in human body, γ is 42.58 MHz/T.

If these nuclei in the strong magnetic field are exposed to an oscillating RF field at their precessional frequency, their motion tilt away from the direction of the main field through an angle that depends on the strength and duration of the RF pulse. After the disturbance induced by RF pulses, as the nuclei return to its equilibrium position about the direction of the main field, the change in magnetization induces a small voltage in a receiver coil in accordance with the law of electromagnetic induction. The nuclei recover to its equilibrium position about the direction of main magnetic field (longitudinal field) at a rate determined by its T_1 and this tissue-specific recovery of magnetization is referred to as T_1 relaxation. Similarly, the transverse magnetic field decays at a rate determined by its T_2. . By altering the pattern of RF pulses applied during imaging, the resulting signal can be altered to emphasize a particular characteristic of signal behavior to get T_1 and T_2 weighted images. Most commonly 90º and 180º pulses are used which flip the net magnetization. For instance, 90º pulses convert all longitudinal magnetization to transverse magnetization. However, flip angles smaller than 90º create less transverse magnetization, but they also saturate less of the longitudinal magnetization. The small flip angles become more advantageous in tissues with long T_1 even if the repetition rate (TR) between RF pulses is short. For a tissue with any given T_1 and TR, there is an optimum flip angle, known as Ernst angle:

$$Ernst\ angle = arc\cos(e^{--\frac{TR}{T1}})$$

that yields the maximum MR signal. For acquiring T_1 weighted images, the optimal flip angle must be higher than the Ernst angle. Conversely, for acquiring T_2 weighted

images a flip angle smaller than the Ernst angle must be used. Moreover, T_2 weighted images usually have a long TR, low flip angle and TEs, the time between the end of the RF excitation pulse and the collection of the MR signal, that are comparable to or slightly longer than the T_2s of the tissues of interest. The desired effects can be enhanced favorably by introduction of contrast agents such as gadolinium chelates and super paramagnetic iron oxide particles which act by shortening the relaxation time of water protons that are close to the contrast agent.

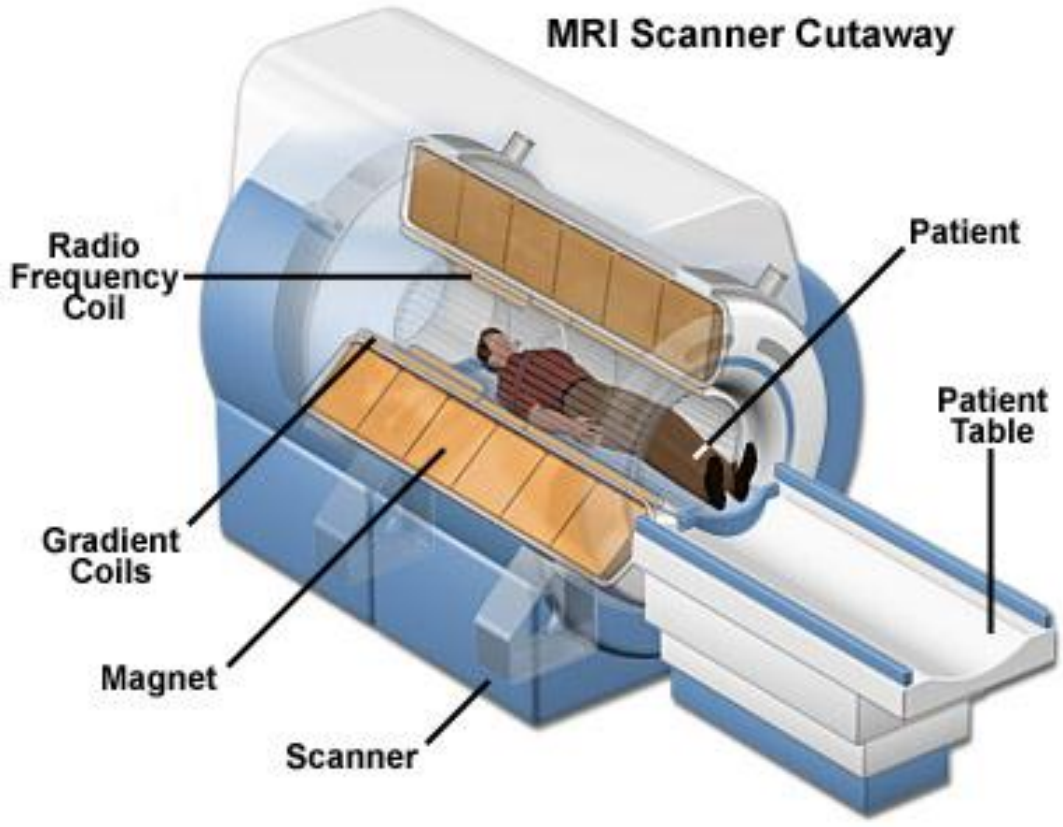

Figure 36 Schematic drawing showing a typical MRI Scanner[152]

To produce images of a region of interest, spatial information is needed. Since the resonant frequency of the nuclei depends on the field strength indicated by Larmor relation, by appropriate use of field gradients generated by gradient coils, different volume elements (voxels) can be labeled by having different resonant frequency. As a result, by calculating the strength of the MR signal at each frequency, the signal strength at each location is identified. During the imaging process a matrix of numbers is generated in K space and the Fourier transformation of this data in K space give rise to the MR image.

In summary, MR images are the result of the medial application of complex physical phenomenon called nuclear magnetic resonance observed some sixty years ago. With the development of better machines, pulse sequences and contrast agents MRI has become the technique of first choice for many medical conditions concerning disorders in joints, nervous system and cancer for its superior contrast especially in soft tissues compared to any other noninvasive imaging modality.

4.2.2 Confocal Microscopy

Confocal microscopy is an optical imaging technique developed to visualize fluorescent molecules in a single plane of focus to create a sharp cross sectional image. It provides several advantages over conventional optical microscopy including elimination or reduction of bleed through away from focal plane and capability to collect serial optical sections to create 3-D images. Especially, non-invasive confocal

optical sectioning techniques enable the examination of living subjects under a variety of conditions with enhanced definition and contrast.

4.2.2.1 History and Principles of Confocal Microscopy[153, 154]

The basic concept of confocal microscopy was originally developed by Marvin Minsky around 1955 while he was trying to image neural networks in unstained preparations of brain tissue of at Harvard University. However, lack of intense light sources and modern computers at the time limited its success. In 1973, M. David Egger published first recognizable images of cells using a mechanically scanned confocal laser microscope. Later in the late 1970s and the 1980s advancements in laser technology and digital manipulation algorithms led to growing interest in confocal microscopy. The first commercial instruments appeared in 1987 and since then laser scanning confocal microscopes have become completely integrated electronic imaging systems composed of optical microscope, electronic detectors, a computer, several laser systems combined with wavelength selection devices and a beam scanning assembly.

Confocal imaging aims to overcome some limitations of the traditional wide-field fluorescence imaging. In traditional wide-field epi-fluorescence microscope a large volume of the specimen is flooded uniformly and simultaneously with a wide cone of illumination from a mercury arc lamp and the emitted fluorescence is detected which includes emitted background light and autofluorescence originating from above and below the focal plane. The confocal microscope uses point illumination, with

pinhole in an optically conjugate plane (confocal) with a scanning point on the specimen, to illuminate a very small spot (0.25-0.8 μm in diameter and 0.5-1.5 μm deep) at the focal plane and the emitted fluorescence is detected through a second pinhole, which limits the collection of the emitted background and auotofluorescence originating from above and below the focal plane, in front of the detector. The typical character and geometry of specimen illumination utilized for wide-field epi-fluorescence and confocal microscope is shown in Figure 37 and the optical configuration of a typical epi-fluorescence confocal laser scanning microscope is shown in Figure 38. Confocal laser scanning microscopes scan the specimen using galvanometer based raster scanning mirrors while spinning disk (Nipkow disk) confocal systems utilize a spinning disk with an array of pinholes to form the image. The confocal laser scanning microscopes provide superior contrast and definition but it suffers from long imaging times and fluorescence bleaching, the limited number of excitation wavelengths available with common lasers and harmful nature of high-intensity laser radiation. The spinning disk confocal systems provide inferior contrast and definition compared to confocal laser scanning microscopes but are able to acquire images in milliseconds and low dose of multiple excitation beams reduce fluorescence bleaching and laser radiation damage to specimen[155].

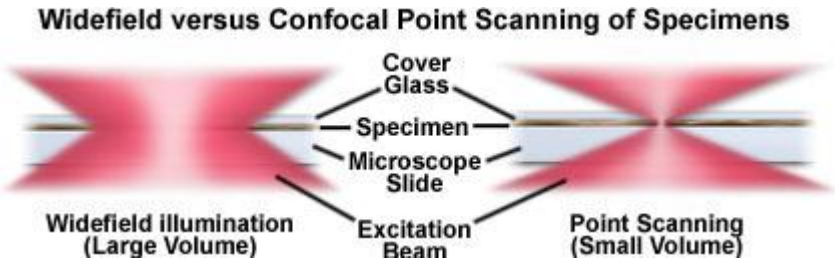

Figure 37 Typical specimen illumination utilized by Wide-field vs. Confocal Microscopy[154]

4.2.3 Two-photon Excitation Microscopy

Two-photon excitation microscopy is an optical imaging technique developed to visualize fluorescent molecules up to about 1 mm depth to create a sharp cross sectional image. It provides several advantages over conventional optical microscopy including elimination or reduction of background signal and deeper tissue penetration. Especially, non-invasive two-photon excitation imaging techniques enable the examination of living subjects under a variety of conditions with enhanced penetration and contrast.

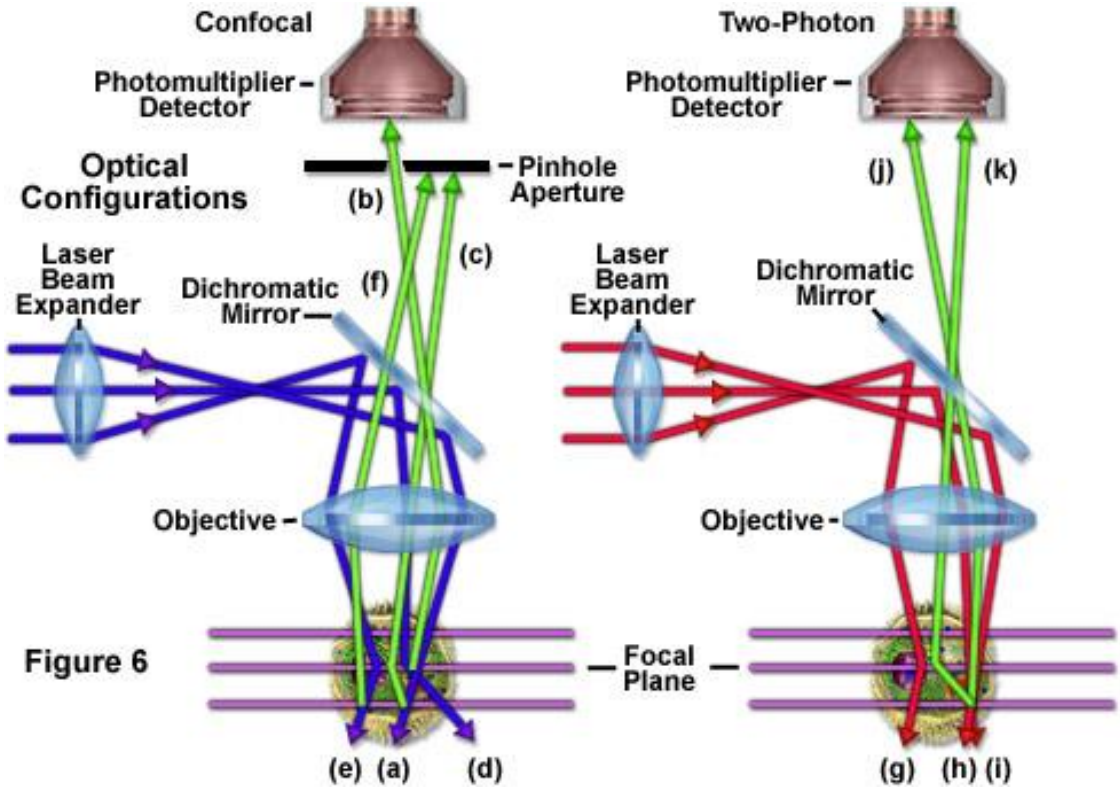

Figure 38 Laser Scanning Confocal Microscope Optical Configuration vs. Two-Photon Laser Scanning Microscope Optical Configuration[156]

4.2.3.1 History and Principles of Two-photon Excitation Microscopy

The theoretical basis of two-photon excitation was first proposed by Maria Goppert-Mayer in her doctoral dissertation in 1931 and was verified in 1961 by Kaiser and Garret[157]. While the possibility of nonlinear excitation for microscopy was recognized in 1978[158], the two-photon excitation microscopy was not demonstrated until 1990[159]. In 1990 Winfried Denk pioneered two-photon excitation microscopy by combining the idea of two-photon absorption with the use of a laser scanner[160].

Two-photon excitation microscopy is an alternative to confocal microscopy with distinct advantage in three-dimensional imaging. The common fluorescence process involves excitation of fluorophore by a single photon usually in the ultraviolet or blue/green spectral range. However, the same excitation process can be achieved by simultaneous absorption of two less energetic photons usually in the infrared spectral range under sufficiently intense laser illumination. If the sum of the energies of the two photons is greater than the energy gap between the fluorophore's ground and excited states, excitation results in the subsequent emission of a fluorescence photon. Because two-photon excitation depends on simultaneous absorption of two photons, the photon density must be about one million times that required for one-photon absorptions in order to produce a significant number of two-photon absorption events. This can be achieved with focusing continuous-wave laser but the high-average laser power concerns favor the use of high repetition rate femtosecond or picosecond lasers such as titanium-sapphire and Nd-YLF lasers with higher peak power and low average power[161]. Typically, laser excites the specimen via epiluminescence and the excitation light is reflected by a dichroic mirror to the microscope objective and the emitted light is detected as depicted in Figure 38. Compared to confocal laser scanning microscope, in laser scanning two-photon excitation microscope, more of the excitation light photons reach the desired specimen level, the red and infrared light used for excitation scatters less and scattering is less detrimental. Consequently, with two-photon excitation microscopy deeper tissue can be imaged with better contrast and less phototoxicity and bleaching compared to confocal at the cost of lower resolution.

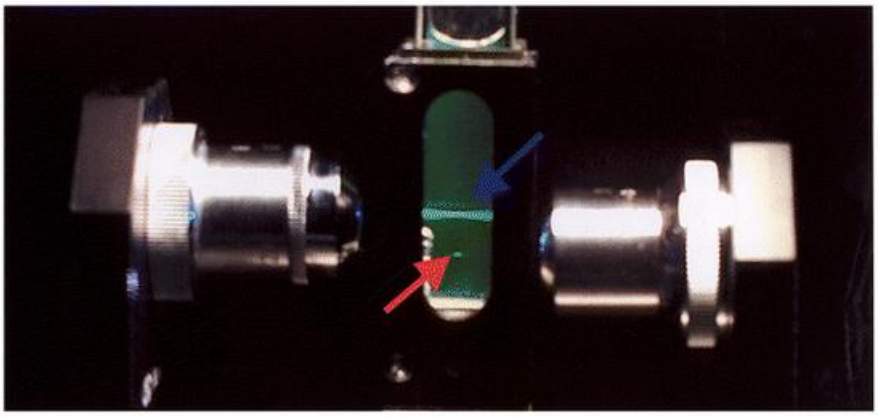

Figure 39 A demonstration of the localization of two-photon excitation[161]

Fluorescein solution is excited by one-photon excitation (blue arrow) via a 0.1 numerical aperture objective; fluorescence excitation is observed throughout the path of the laser beam. For two-photon excitation using a second objective with the same numerical aperture (red arrow), fluorescence excitation occurs only from a 3D localized spot.

4.3 MRI Compatible Rodent Dorsal Skinfold Chamber Model Studies Of Theranostic Nanoplatforms

MRI compatible rodent dorsal skinfold chamber model is an attractive model to study and observe the interaction between therapeutic agent and tumor as it allows noninvasive chronic observation of a single animal in the duration of treatment with high resolution as well as the combination and cross validation of results from optical microscopy and MRI. Especially with new nanomedicine paradigm, highly integrated theranostic nanoplatforms that incorporate multiple functions such as imaging and therapy are creating new possibilities for intravital models such as MRI compatible

rodent dorsal skinfold chamber. While MRI compatible chamber model is mostly limited to the study of non-orthotopic tumors, it is a valuable bridge to orthotopic xenograft model studies to simplify and accelerate the development of theranostic nanoplatforms. Unlike the studies with orthotopic xenograft models, a single animal is used throughout the treatment and observations are made on a single animal instead of a separate animal for each observation point as is the case for orthotopic xenograft models. Once the necessary refinements are made on theranostic agents and imaging parameters based on the results of MRI compatible rodent dorsal skinfold chamber studies, further studies can be translated into orthotopic xenograft models.

4.3.1 Preparation and Implantation of Chamber and Tumor Cells

Lewis Lung Carcinoma (LLC) cell lines are cultured as described in Preparation and Implantation of Tumor Cells section of 3.3. The tumor cell lines are transfected to express Discosoma sp. Red fluorescent protein (DsRed-2). Once the cells reach 80% confluency, they are prepared for implantation. First, they are washed with sterile phosphate buffered saline (PBS), and then are treated with trypsin for about 2 minutes at 37ºC. Following the trypsin treatment, they are washed off the dishes with medium, and then are centrifuged for about 5 minutes at 3000 rpm. The resultant pellet is resuspended in PBS, and the cell density is counted with a hemocytometer. The final pellet is resuspended in PBS at a concentration of 200,000 cells/µl. The MRI compatible rodent dorsal skinfold chamber assemblies described in 3.3 are implanted on nude mice as described in surgery section of 3.3 following the

protocols approved by University of California San Diego IACUC committee. After the surgery, the chambers are checked for successful implantation based on the criteria outlined in post-surgery section of 3.3. After 1 to 2 days of recovery time, subject with successful chamber implantation is injected with 5 μl of tumor cell suspension (about 1,000,000 cells) prepared as described previously, into the outer portion of the retractor muscle, between two major vessels near the top of the window. The chamber is sealed with a fresh, sterile glass coverslip and attention is paid to avoid and expel air bubbles within the chamber. The subject is removed from the mouse cylinder and returned to its cage to recover.

4.3.2 Preparation of Theranostic Nanoplatforms

The liposomal theranostic nanoplatform is based on dextran core to accept a multitude of agents, including iron oxide for magnetic resonance imaging (MRI) contrast, fluorescent marker BODIPY for optical imaging and therapeutic agents. Once super paramagnetic iron oxide (SPIO) nanoparticles are coated with dextran, they are treated with doxorubicin hydrochloride dissolved in phosphate buffered saline (PBS) for 24 hours. Then, the core structure is purified using G25 size exclusion chromatography. The purified core structure solution at 1-5 mg/ml in PBS is added to the lipid film formed by evaporation of nanoshell mixture described in XXX. High-energy sonication is applied and the resultant mixture is extruded through 400 nm, 200 nm and 100 nm polycarbonate membranes sequentially. The solution is exposed to ultraviolet (UV) radiation for 3 to 5 minutes under mercury arc lamp in order to

crosslink acetylene groups. Average particle size of the final solution is measured using dynamic light scattering and once the average size is verified to be within the expected range, it is stored at 4ºC. Before imaging of the subjects, the core solution is taken out of the cold storage and kept on ice until the injection via tail-vein.

4.3.3 MR Imaging

MR images are acquired in 7.0 T small animal scanner (21 cm bore Bruker Avance II) at Center for Functional MRI of University of California, San Diego. Nude mouse with Lewis Lung Carcinoma (LLC) growing in their MRI compatible dorsal skinfold chamber is anesthetized with 1.5% isoflurane and placed within the holding cradle shown in Figure 34. A custom surface coil with 1.5 cm diameter is positioned next to the chamber glass coverslip and MR images are acquired using T2 weighted RARE sequence (field of view = 2.5 mm, Mx = 256x256, TR = 7151 ms, TE = 56.7 ms, Slice Thickness = 1.5 mm) before and after injection of the dextran-iron oxide core theranostic nanoparticles via the tail vein. The MR images of the chamber acquired using the T2 weighted RARE sequence before and 24 hours after the injection of nanoparticles with their corresponding gray level histograms are shown in Figure 40. Regions of interest sections and major feeding vessels segments of the

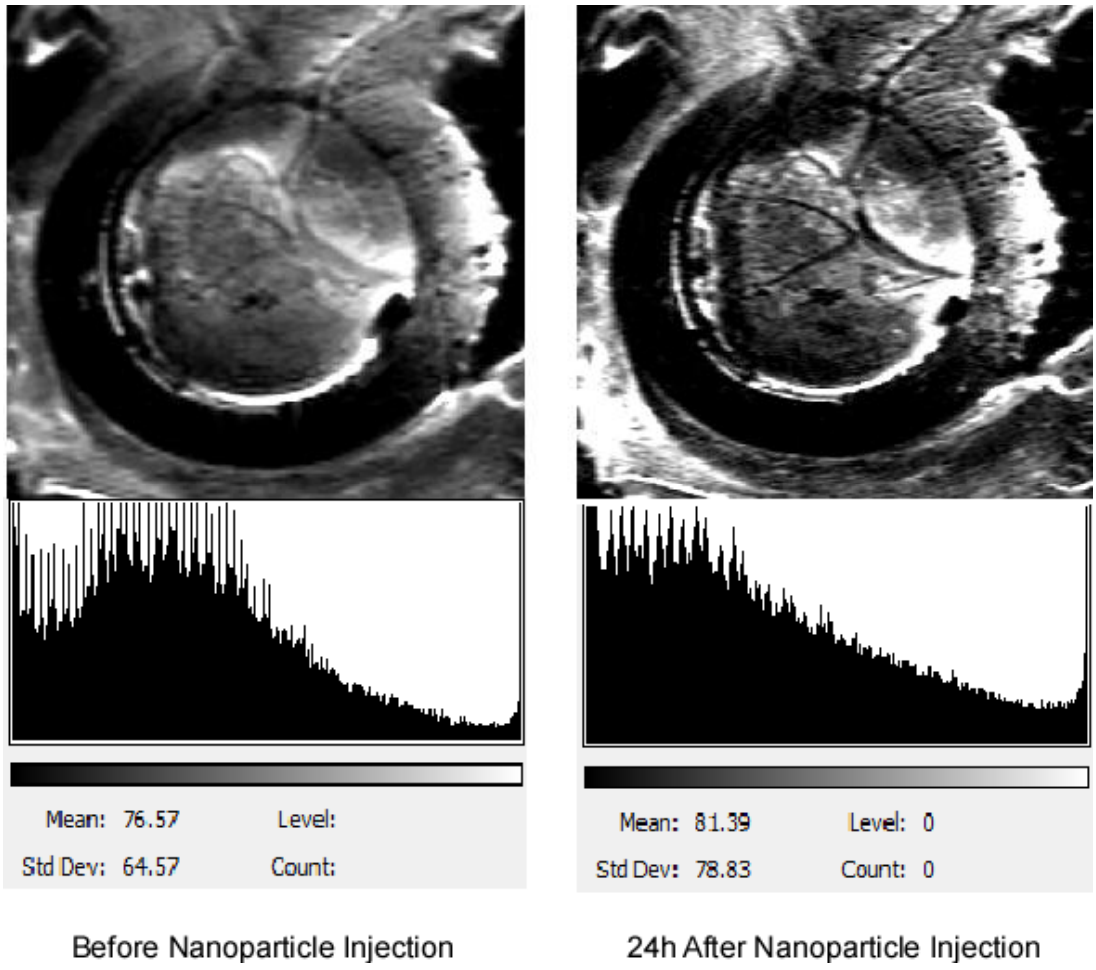

Figure 40 Comparison of MR images acquired in 7T Bruker before and 24 hours after injection of dextran-iron oxide core theranostic nanoparticles.

MR images are acquired using T2 weighted RARE sequence (field of view = 2.5 mm, Mx = 256x256, TR = 7151 ms, TE = 56.7 ms, Slice Thickness = 1.5 mm) before and after injection of the dextran-iron oxide core theranostic nanoparticles via tail-vein. Corresponding gray level histograms are shown at the bottom of MR images. The lower mean value indicates a darker image.

chamber MR images from Figure 40 are shown in Figure 41 with their corresponding gray level histograms next to them.

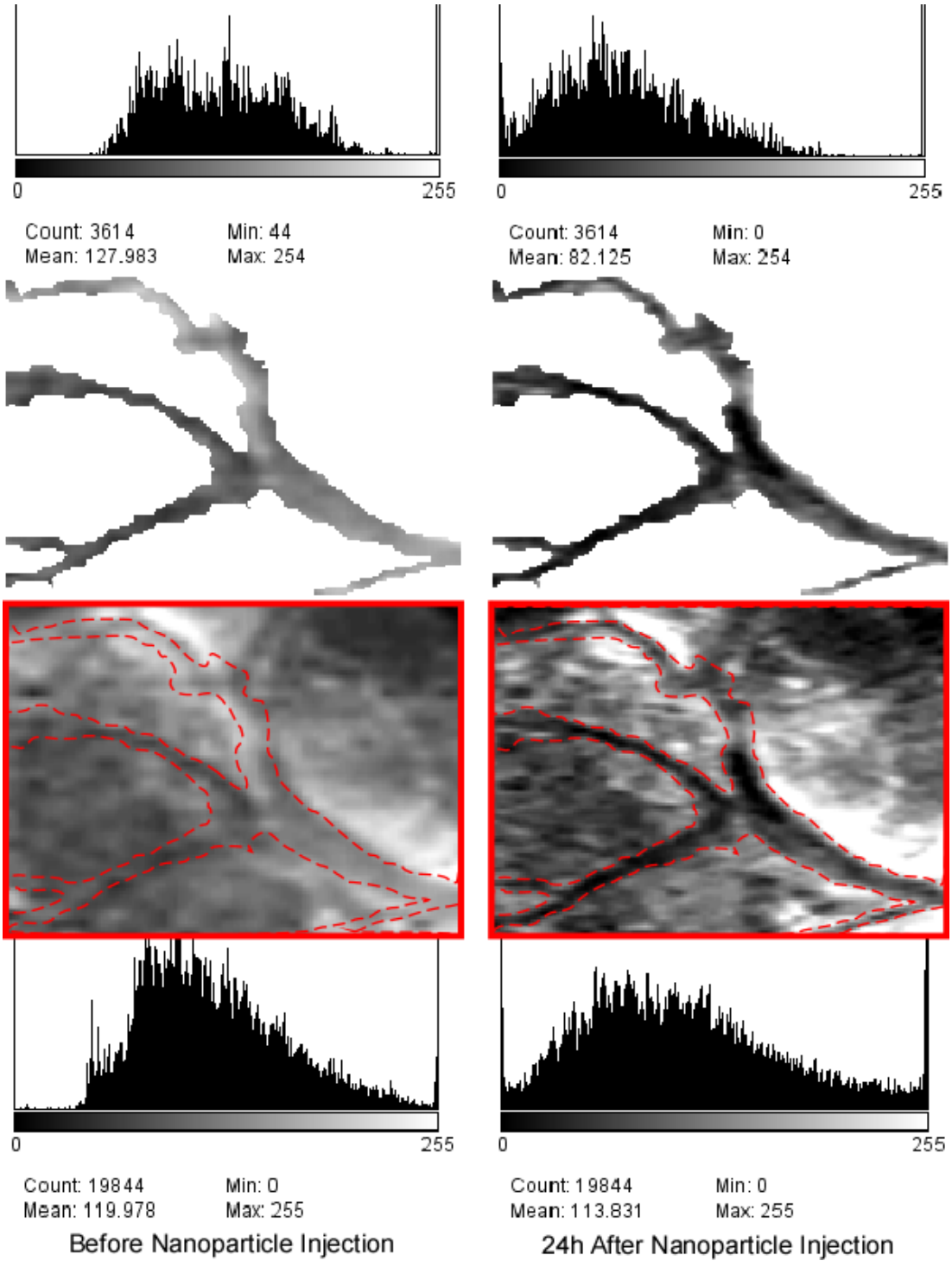

Figure 41 Comparison of MR images acquired in 7T Bruker before and 24 hours after injection of dextran-iron oxide core theranostic nanoparticles.

4.3.4 Optical Imaging

To validate the MRI findings, dorsal skinfold chamber with LLC tumor cell lines transfected to express DsRed-2 is imaged right after MR image acquisitions with a standard brightfield-fluorescence microscope and a laser-scanning two-photon microscope. The mouse was injected with fluorescently labeled theranostic nanoparticles intravenously via tail vein during the MR image acquisitions. The subject is secured within transparent mouse cylinder, is attached to the custom mouse holder that is shown in Figure 35 and is imaged using both epi-illuminated brightfield and fluorescence at 1x, 4x. Next, the subject is imaged at 20x using two-photon microscope. The two-photon microscope images of the chamber sections are shown in Figure 42.

4.3.5 Results

The MR images acquired in 7T Bruker small animal system using T2 weighted RARE sequence revealed darkening in the vessels and tumor area after the injection of dextran-iron oxide core theranostic nanoparticles compared to the images acquired before injection. While the mean values of the gray level histograms of the before and after injection MR images shown in Figure 40 are not indicating any darkening, the mean values of the gray level histograms of regions of interest of the same chamber shown in Figure 41 indicate significant darkening especially within the major feeding vessels outlined and segmented out in same figure. The ratios of mean value of gray scale histograms before and after injection are tabulated in Table 8. In this table, a

bigger ratio of mean gray value of before injection to after injection indicates a better contrast agent potential and more theranostic nanoparticle accumulation. Based on the before and after injection mean gray value ratios calculated in Table 8, the darkening is not an artifact observed over the entire MR image but rather a local event confined within the major feeding blood vessels and theranostic nanoparticles can be detected in vivo with MRI and they accumulate within major feeding vessels. The optical images acquired to validate MRI results show heavy accumulation of BODIPY labeled theranostic particles around DSRed-2 labeled tumor as blue staining in Figure 42. The theranostic particles could be imaged at 24 hours after injection as well. This indicated that the particles survived within the circulation and accumulated intact in the tumor.

Table 8 Efficacy of Theranostic Nanoparticles on MR Image Contrast in MRI Compatible Dorsal Skinfold Chamber Model

Figure	Before Injection Mean Gray Level	After Injection Mean Gray Level	Before Injection / After Injection
Chamber	76.57	81.39	0.94
Regions of Interest	119.98	113.83	1.05
Feeding vessels	127.98	82.12	1.56

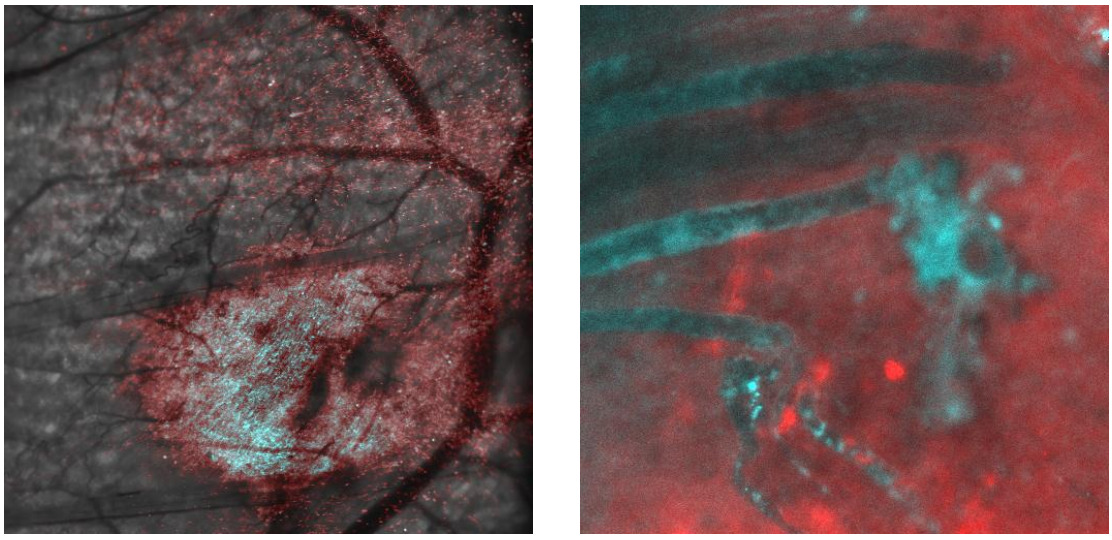

Figure 42 Optical Images of Nanoparticle Accumulation at Tumor Site

The left panel is a 2-Photon acquisition with only the blue laser and the blue channel active (Blue staining is due to the BODIPY-labeled nanoparticles). The right panel shows a red channel acquisition at 10x blended with the blue channel acquisition (Note the extensive blue staining of tumor blood vessels and stroma)

4.4 Orthotopic Xenograft Model Studies of Theranostic Nanoplatforms

The MRI compatible rodent dorsal skinfold chamber model is an excellent model for studying the interaction between theranostic agents and tumors. However, the non-orthotopic natures of tumors that are observed in dorsal skinfold chamber models, limit the successful translation of the results into clinical trials. Therefore, another model is needed to link and further verify the results acquired in MRI compatible dorsal skinfold chamber models. Recently there have been great debates on which mouse models of cancer should be used to screen new drugs before they enter clinical trials. Thirty years of experience with subcutaneous xenografts, human

tumors implanted under the skin of the mouse, proved that so many successful treatments that cure cancer in these mice fail to demonstrate same results on human subjects[162]. Orthotopic xenograft mouse model, human tumors implanted to the equivalent mouse organ, and transgenic mouse model, genetically engineered mice with genetic defects that give rise to mouse tumors, are two alternatives to subcutaneous xenografts. Intact immune system, native tumor microvasculature and microenvironment and gradual development of cancer are major advantages of the cancer transgenic or genetically engineered model (GEM) over subcutaneous xenografts. However, GEM tumors are often structurally different than human tumors due to physiological and genetic differences and they develop tumors at different times. Better simulation of the tumor microenvironment and ability of cancer cells to metastasize are the major advantages of the orthotopic xenografts over subcutaneous xenografts. However, unlike GEMs the mice are immune compromised and the tumor is not native to the animal. There is no conclusive evidence to demonstrate one model's superiority over the other but the structural differences of GEM tumors are a major concern and orthotopic xenograft mouse model is a better and more compatible test-bed to translate results acquired in MRI compatible rodent dorsal skinfold chamber models. Therefore, orthotopic xenograft model is used for further studies of interaction between theranostic nanoparticles refined using MRI compatible chamber models and tumor.

4.4.1 Preparation and Orthotopic Implantation of Tumor Cells

Typically human pancreatic carcinoma cell line (MIA PaCa-2) is cultured in 95% air and 5% CO_2 at 37ºC using Dulbecco modified Eagle medium (DMEM) with 10% fetal calf serum (FCS), 1% penicillin and streptomycin[144, 145]. The tumor cell lines are transfected to express Discosoma sp. Red fluorescent protein (DsRed-2). Once the cells reach 80% confluency, they are prepared for implantation. First, they are washed with sterile phosphate buffered saline (PBS), and then are treated with trypsin for about 2 minutes at 37ºC. Following the trypsin treatment, they are washed off the dishes with medium, and then are centrifuged for about 5 minutes at 3000 rpm. The resultant pellet is resuspended in PBS, and the cell density is counted with a hemocytometer. The final pellet is resuspended in PBS at a concentration of 100,000 cells/µl and kept on ice until the surgery.

Before the surgery, the nude mice are checked for overall health status and then are anesthetized by subcutaneous injections of 100mg/kg of ketamine and 250 to 500 mcg/kg of medetomidine. The abdomen is then washed with saline and Betadine antiseptic is applied, cleaned with 70% ethanol swabs. Then left lateral laparotomy is performed and 1 µl tumor cell suspension (about 100,000 cells) is injected in the tail of the pancreas using a 5 µL gas tight glass syringe fitted with a 28 gauge needle. The flank is reapproximated and sutured and the animal is returned to its cage to recover.

4.4.2 Preparation of Theranostic Nanoplatforms

The liposomal theranostic nanoplatform is based on dextran core to accept a multitude of agents, including iron oxide for magnetic resonance imaging (MRI) contrast, fluorescent marker BODIPY for optical imaging and therapeutic agent doxorubicin hydrochloride. The theranostic nanoplatform suspension is prepared as described in previous section 4.3.2. Average particle size of the final solution is measured using dynamic light scattering and once the average size is verified to be within the expected range, it is stored at 4ºC. Before imaging of the subjects, the core solution is taken out of the cold storage and kept on ice until the injection via tail-vein.

4.4.3 MR Imaging

MR images are acquired in 7.0 T small animal scanner (21 cm bore Bruker Avance II) at Center for Functional MRI of University of California, San Diego. Nude mouse with human pancreatic carcinoma (MIA PaCa-2) implanted orthotopically is anesthetized with 1.5% isoflurane and placed within the holding cradle shown in Figure 34. A birdcage type of coil is used to acquire MR images using T2 weighted RARE sequence (field of view = 2.5 mm, Mx = 256x256, TR = 7151 ms, TE = 56.7 ms, Slice Thickness = 1.5 mm) before and after injection of the dextran-iron oxide core theranostic nanoparticles intravenously via the tail vein. The MR images of the animal's entire abdomen acquired using the T2 weighted RARE sequence before and 24 hours after the injection of nanoparticles with their corresponding gray level histograms are shown in Figure 43. Regions of interest of the whole abdomen MR

images are delineated with red squares and close up views of regions of interest are shown in Figure 44 with their corresponding gray level histograms next to them.

4.4.4 Optical Imaging

To validate the MRI findings, orthotopic xenograft mouse model with human pancreatic carcinoma tumor cell lines (MIA PaCa-2) transfected to express DsRed-2 is imaged after MR image acquisitions with a standard brightfield-fluorescence microscope and a laser-scanning two-photon microscope. The subject was injected with fluorescently labeled theranostic nanoparticles intravenously via tail vein during the MR image acquisitions. The mouse is euthanized and pancreas is removed. Then the pancreas and tumor is imaged using two photon microscope at 20x. The two-photon image of removed tumor and theranostic nanoparticles is shown in Figure 45.

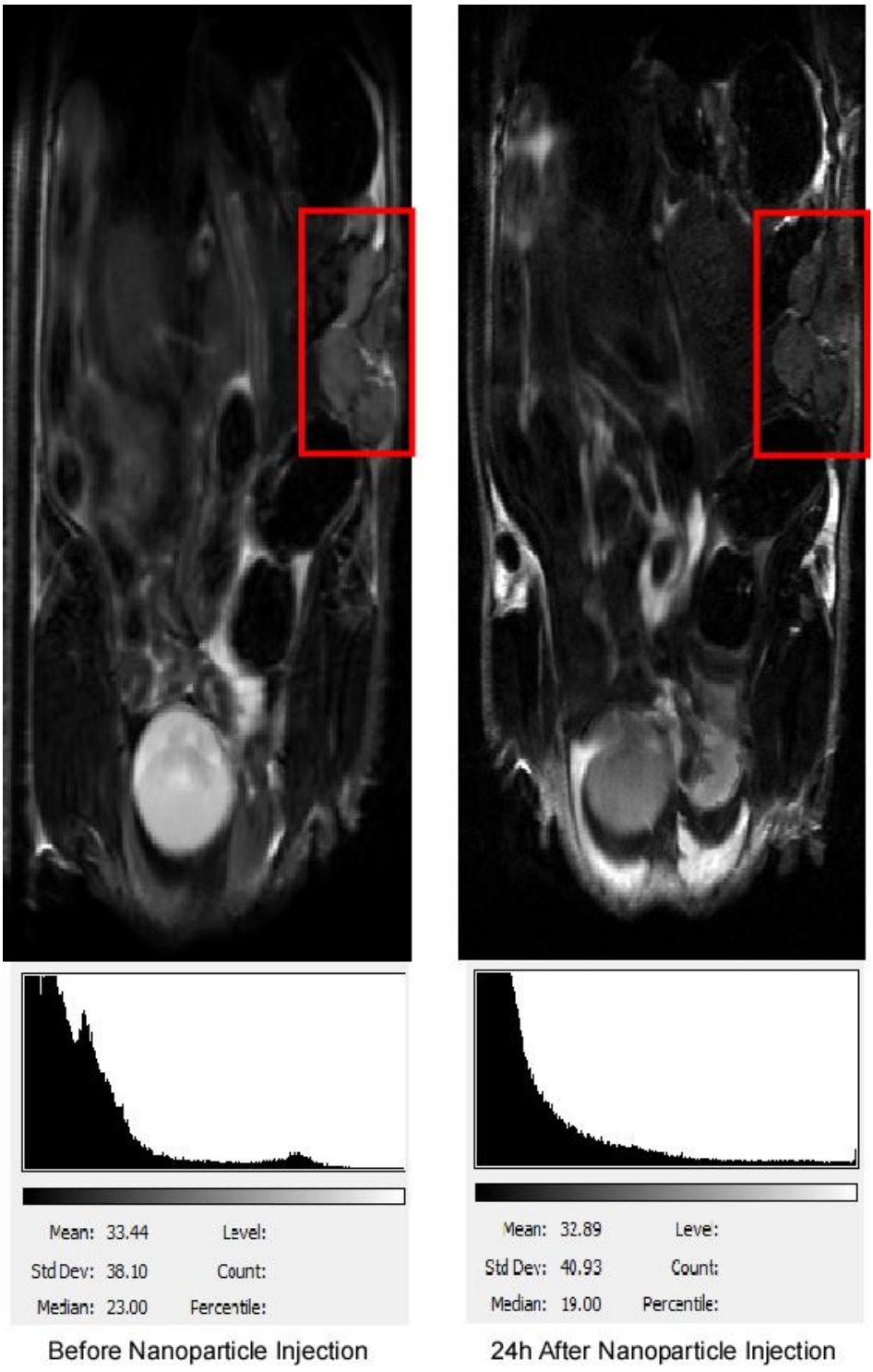

Figure 43 Comparison of MR images of orthotopic MIA PaCa-2 tumor and abdomen acquired in 7T Bruker before and 24 hours after injection of dextran-iron oxide core theranostic nanoparticles.

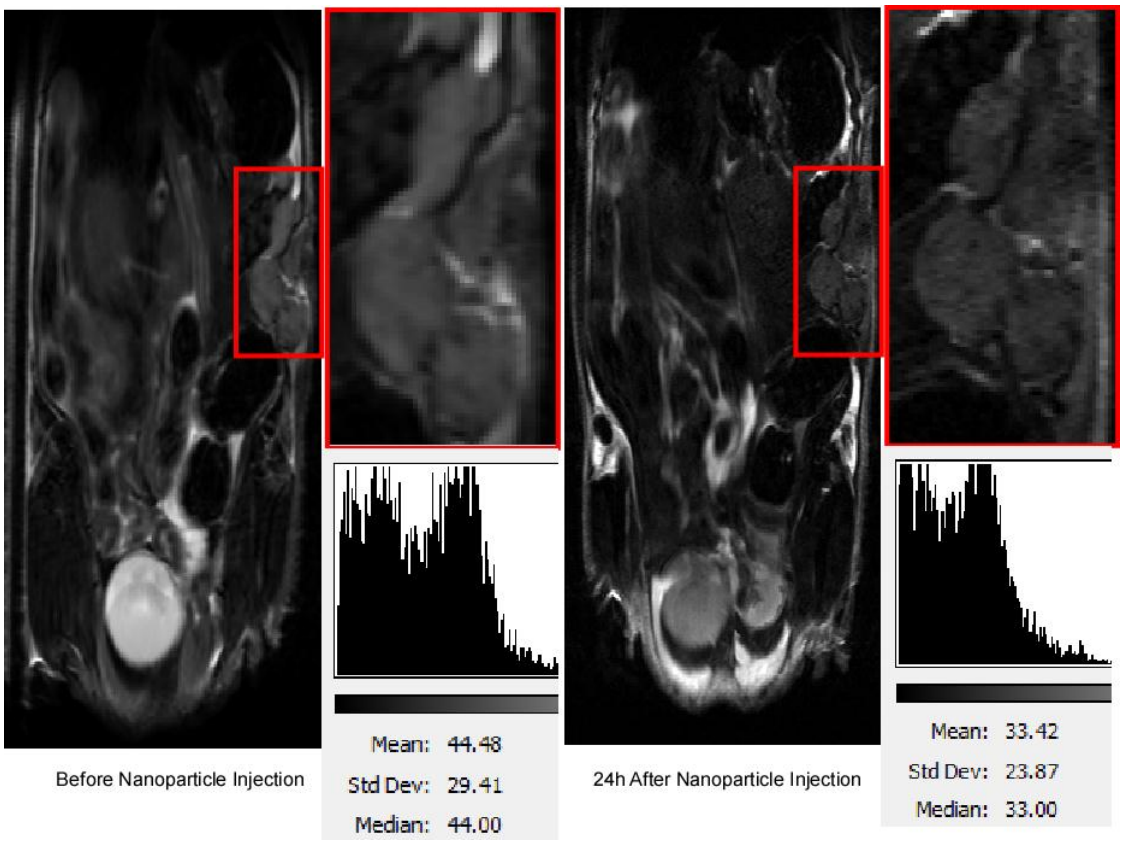

Figure 44 Comparison of MR images of ROIs of orthotopic MIA PaCa-2 tumor acquired in 7T Bruker before and 24 hours after injection of dextran-iron oxide core theranostic nanoparticles.

MR images are acquired using T2 weighted RARE sequence (field of view = 2.5 mm, Mx = 256x256, TR = 7151 ms, TE = 56.7 ms, Slice Thickness = 1.5 mm) before and after injection of the dextran-iron oxide core theranostic nanoparticles via tail-vein. Regions of interest are delineated with red squara and close up views are shown next to the whole abdomen images. Corresponding gray level histograms of regions of interest are shown at the bottom of MR images. The lower mean value indicates a darker image.

Figure 45 Two-photon image of the removed orthotopic MIA PaCa-2 Tumor

Two-photon image of BODIPY labeled theranostic nanoparticles shown in the tumor vessels and extravasating into the surrounding tissue of removed orthotopic MIA PaCa-2 tumor.

4.4.5 Results

The MR images acquired in 7T Bruker small animal system using T2 weighted RARE sequence revealed darkening in the pancreas and body wall of MIA PaCa-2 tumors after the injection of dextran-iron oxide core theranostic nanoparticles compared to the images acquired before injection. While the mean values of the gray level histograms of the before and after injection MR images shown in Figure 43 are not indicating any darkening, the mean values of the gray level histograms of regions of interest of the same chamber shown in Figure 44 indicate significant darkening

especially within the tumor and associated vasculature. The ratios of mean value of gray scale histograms before and after injection are tabulated in Table 9. In this table, a bigger ratio of mean gray value of before injection to after injection indicates a better contrast agent potential and more theranostic nanoparticle accumulation. Based on the before and after injection mean gray value ratios calculated in Table 9, the darkening is not an artifact observed over the entire MR image but rather a local event confined within the tumor and its microvasculature and theranostic nanoparticles can be detected in vivo with MRI and they accumulate within tumor area, as was also the case with acquired MR images of dorsal skinfold chamber model. The whole body MR images acquired 24 hours after injection of theranostic nanoparticles also indicate darkening in spleen, kidney and urinary bladder.

Table 9 Efficacy of Theranostic Nanoparticles on MR Image Contrast in Orthotopic Xenograft Model

Figure	Before Injection Mean Gray Level	After Injection Mean Gray Level	Before Injection / After Injection
Whole Abdomen	33.44	32.89	1.02
Regions of Interest	44.48	33.42	1.33

The optical images acquired to validate MRI results show heavy accumulation of BODIPY labeled theranostic particles around DSRed-2 labeled tumor as blue staining in Figure 45. The theranostic particles could be imaged at 24 hours after

injection as well. This indicated that the particles survived within the circulation and accumulated intact in the tumor.

4.5 Conclusions

The feasibility of a dextran-iron oxide core theranostic nanoparticle and the function of MRI compatible dorsal skinfold chamber in its development is demonstrated. Theranostic particles are first imaged in animals with MRI compatible dorsal skinfold chamber implanted on with LLC tumor growing within. Based on the chamber imaging results, the amount of iron-oxide and fluorescence content is adjusted to improve contrast in MRI and visibility in optical microscopy. The MRI compatible dorsal skinfold chamber is used to verify the MR images with optical microscopy. We were able to image the nanoparticles within the chamber around tumor using two-photon microscopy even 24 hours after the injection of the nanoparticles via tail vein. This also allowed us to deduce the integrity of the particles as the fluorescent markers were on the surface of the particles while the iron-oxide was at the core. Next, after the optimization of the theranostic nanoplatform formulations and dosage in MRI compatible dorsal skinfold chamber test-bed, theranostic nanoparticles are imaged in orthotopic xenograft models with MIA PaCa-2 tumors. The MR imaging results in orthotopic xenograft models revealed darkening effect similar to the images acquired with MRI compatible rodent dorsal skinfold chamber in terms of contrast enhancement. Next, the MR results are validated in

orthotopic xenograft models as well with imaging via two-photon microscope. The accumulation of nanoparticles within the tumor area and tumor microvasculature is imaged and the integrity of nanoparticles is demonstrated. The MRI results from orthotopic xenograft models also revealed accumulation of nanoparticles within bladder, kidney and spleen. However, this can be avoided using targeting moieties in the next formulation of the theranostic nanoplatforms. The next generation of theranostic nanoplatforms might be activated at a specifc time and location externally to release their payloads by externally applied ultrasound or light as well to reduce morbidity.

Ultimately, theranostic nanoplatforms that can be tracked with MRI have enormous clinical potential and MRI compatible dorsal skinfold chamber provides a shortcut in the development of these theranostic nanoplatforms.

Acknowledgement:

This chapter, in part, is a reprint of the material as it appears in : A. Erten, W. Wrasidlo, M. Scadeng, S. Esener, R. Hoffman, M. Bouvet and M. Makale, “Magnetic resonance and fluorescence imaging of doxorubicin-loaded nanoparticles using a novel in vivo model”, submitted to Nanomedicine: Nanotechnology, Biology and Medicine. The dissertation/thesis author was the primary investigator and author of this paper.

5 CONCLUSION

5.1 Dissertation Summary and Original Contributions

This dissertation addressed the design, fabrication and testing of two novel multifunctional nanoplatforms; a liposome containing dextran hydrogel and iron oxide, and a liposome containing perfluorocarbon (PFC) gas microbubble. The dextran hydrogel liposome design was derived from conventional and well-established liposome technology and expanded in terms of its capabilities. The micro-bubble containing liposome was of a more experimental nature, and represented an exploration of the fabrication of a new platform for multifunctional nano-medicine. A key limitation of nanoengineering in medicine is the lack of practical *in vivo* models, so that many nanoplatforms, while creatively engineered, are not biologically useful. In order to address this deficiency, this dissertation also extensively discussed the development and implementation of an *in vivo* test-bed. This system was designed to facilitate optical and MR imaging of nanoplatforms within a tumor and its blood vessels.

The original contributions of this work are summarized below:

- Development of a novel multifunctional liposomal nanoplatform containing iron oxide for MR contrast, a dextran hydrogel core for efficient drug loading, PEG to avoid opsonization, and BODIPY for optical detection.
- Development of a microfluidic system for fabrication of a novel multifunctional liposomal platform containing a microbubble for US contrast and the capacity for disintegration by externally applied US to release a therapeutic agent.
- Development of a cryogenic etching process for fabrication of hybrid SU8-Silicon Micronozzles for a micronozzle based system for large-scale monodisperse microparticle and emulsion fabrication.
- Development of a silicon micronozzles based system for large-scale monodisperse microparticle and emulsion fabrication.
- Development of a novel and practical *in vivo* test-bed that allows optical and MR imaging of labeled nanoplatforms within a live tumor and its blood vessels.
- *In vivo* demonstration of the multifunctional potential of a liposomal nanoplatform containing iron oxide for MR contrast, BODIPY for optical imaging, and good drug loading. This point to the feasibility of using multifunctional nanoparticles to combine MRI with fluorescence imaging via an endoscope for accessible body structures such as the GI tract, bronchi, and bladder.
- Validation of the MR contrast potential of a multifunctional liposomal nanoplatform containing iron oxide both *in vitro* and *in vivo* in comparison to Ferridex. I.V.

5.2 Future Research

This dissertation summarizes research on two novel multifunctional nanoplatforms, and the development of a novel test-bed for *in vivo* validation of nanoplatforms. This research should be seen as a first step in a more clinically relevant multifunctional nanoparticle development scheme with *in vivo* multimodal cross-validation of a candidate nanoplatform in terms of its functionality. Below we will outline some of the exciting opportunities for innovation arising from the work described here.

In terms of nanoplatform fabrication, monodispersity is a desired but not readily achieved aspect for many proposed structures. Usually batch processes meet the demand for large-scale fabrication. However, they lack the tight size distribution which is crucial for many nanoplatforms such as microbubbles, where microbubble diameter determines the resonance frequency of a microbubble and in case of broad size distribution only a small portion of the microbubble population can respond to the limited bandwidth of ultrasound transducer which results in reduced sensitivity of the imaging system. Recently, microfluidic techniques provided researchers with devices capable of producing highly monodisperse microparticles and possibly nanoparticles. Unfortunatelly, microfluidic systems are limited to research labs due to the problems in scalability of product fabrication volume to meet the demand in a clinical setting. Silicon micronozzle based fabrication scheme can be a potential candidate to meet the monodispersity requirements as well as the large-scale fabrication. This structure can

be scaled up and the fabricated particle size can be scaled down relatively easily as long as current semiconductor fabrication techniques permit.

In terms of nanoplatform functional validation, while the *in vivo* multimodality test-bed is capable of chronic observation of the therapeutics and tumor interaction, the UCSD regulations limited this observation window to 24 hours. This platform would show its real potential in a therapeutic study expanding to 2-3 weeks. Also the externally triggered (via magnetic field, ultrasound, light) rupture of multifunctional liposomes can be observed with high resolution with this readily developed system. Moreover, other external triggering mechanisms can be investigated with minor modifications to the developed test-bed. The developed test-bed has great potential in future development of multifunctional nanoplatforms and can become a standard tool.

Targeting of the iron oxide containing nanoplatform is another functionality that should be explored in future work, and the utility of imaging to reveal non-specific washout over time with bound platforms remaining in target tissue is very relevant to potential clinical use. The efficacy in terms of tumor response needs to be characterized in this context. Moreover, the ability to detect very small metastatic foci with targeted iron oxide containing platforms needs to be characterized to ascertain detection limits with MRI and perhaps CT as well.

Microbubble containing liposomes are a promising set of particles with unique acoustic properties but their stability and preparation schemes need to be improved for them to be a real contender as a theranostic platform and should be subject of a future

research. They hold the advantage of potentially be able to distintegrate under external ultrasound beams to release payloads, enzymes and to activate pro-drugs.

In summary, this thesis demonstrated the feasibility of a multifunctional nanoplatform that can be imaged in the body. In addition, an in vivo test-bed was successfully implemented and may serve as a valuable tool for the validation and optimization of nanoplpatforms for in vivo use.

REFERENCES

1. Shimkin,M.B. *Contrary to Nature*1977).

2. American Cancer Society. Cancer Facts and Figures 2010. 2010. Ref Type: Online Source

3. World Cancer Report 2008. eds. Boyle, P. & Levin, B. 2010. IARC Publications.
Ref Type: Online Source

4. The Lifetime Probability of Developing and Dying from Cancer. 2010. American Cancer Society.
Ref Type: Online Source

5. Grobmyer,S.R. & Moudgil,B.M. *Cancer nanotechnology methods and protocols*(Humana Press, New York, 2010).

6. Sumer,B. & Gao,J. Theranostic nanomedicine for cancer. *Nanomedicine. (Lond)* 3, 137-140 (2008).

7. Alexis,F. *et al.* New frontiers in nanotechnology for cancer treatment. *Urol. Oncol.* 26, 74-85 (2008).

8. Blanco,E., Kessinger,C.W., Sumer,B.D., & Gao,J. Multifunctional micellar nanomedicine for cancer therapy. *Exp. Biol. Med. (Maywood.)* 234, 123-131 (2009).

9. Heath,J.R. & Davis,M.E. Nanotechnology and cancer. *Annual Review of Medicine* 59, 251-265 (2008).

10. Green,M.R. *et al.* Abraxane((R)), a novel Cremophor((R))-free, albumin-bound particle form of paclitaxel for the treatment of advanced non-small-cell lung cancer. *Annals of Oncology* 17, 1263-1268 (2006).

11. Ellerhorst,J.A. *et al.* Phase II trial of doxil for patients with metastatic melanoma refractory to frontline therapy. *Oncology Reports* 6, 1097-1099 (1999).

12. Fassas,A. & Anagnostopoulos,A. The use of liposomal daunorubicin (DaunoXome) in acute myeloid leukemia. *Leukemia & Lymphoma* 46, 795-802 (2005).

13. Wang,Y.X., Hussain,S.M., & Krestin,G.P. Superparamagnetic iron oxide contrast agents: physicochemical characteristics and applications in MR imaging. *Eur. Radiol.* 11, 2319-2331 (2001).

14. Matsuura,N. & Rowlands,J.A. Towards new functional nanostructures for medical imaging. *Medical Physics* 35, 4474-4487 (2008).

15. Vijayaraghavalu,S., Raghavan,D., & Labhasetwar,V. Nanoparticles for delivery of chemotherapeutic agents to tumors. *Current Opinion in Investigational Drugs* 8, 477-484 (2007).

16. Yu,M.K. *et al.* Drug-loaded superparamagnetic iron oxide nanoparticles for combined cancer imaging and therapy in vivo. *Angewandte Chemie-International Edition* 47, 5362-5365 (2008).

17. Ito,A., Shinkai,M., Honda,H., & Kobayashi,T. Medical application of functionalized magnetic nanoparticles. *J. Biosci. Bioeng.* 100, 1-11 (2005).

18. Lu,A.H., Salabas,E.L., & Schuth,F. Magnetic nanoparticles: synthesis, protection, functionalization, and application. *Angew. Chem. Int. Ed Engl.* 46, 1222-1244 (2007).

19. Lanza,G.M. *et al.* Magnetic resonance molecular imaging with nanoparticles. *J. Nucl. Cardiol.* 11, 733-743 (2004).

20. Harisinghani,M.G. *et al.* Noninvasive detection of clinically occult lymph-node metastases in prostate cancer. *New England Journal of Medicine* 348, 2491-24U5 (2003).

21. Kohler,N. *et al.* Methotrexate-immobilized poly(ethylene glycol) magnetic nanoparticles for MR imaging and drug delivery. *Small* 2, 785-792 (2006).

22. Hwu,J.R. *et al.* Targeted Paclitaxel by Conjugation to Iron Oxide and Gold Nanoparticles. *Journal of the American Chemical Society* 131, 66-+ (2009).

23. Veiseh,O. *et al.* Optical and MRI multifunctional nanoprobe for targeting gliomas. *Nano Letters* 5, 1003-1008 (2005).

24. Jain,T.K., Morales,M.A., Sahoo,S.K., Leslie-Pelecky,D.L., & Labhasetwar,V. Iron oxide nanoparticles for sustained delivery of anticancer agents. *Mol. Pharm.* 2, 194-205 (2005).

25. Kohler,N., Sun,C., Wang,J., & Zhang,M.Q. Methotrexate-modified superparamagnetic nanoparticles and their intracellular uptake into human cancer cells. *Langmuir* 21, 8858-8864 (2005).

26. Nasongkla,N. *et al.* Multifunctional polymeric micelles as cancer-targeted, MRI-ultrasensitive drug delivery systems. *Nano Letters* 6, 2427-2430 (2006).

27. Martina,M.S. *et al.* Generation of superparamagnetic liposomes revealed as highly efficient MRI contrast agents for in vivo imaging. *Journal of the American Chemical Society* 127, 10676-10685 (2005).

28. Lee,J.H. *et al.* All-in-One Target-Cell-Specific Magnetic Nanoparticles for Simultaneous Molecular Imaging and siRNA Delivery. *Angewandte Chemie-International Edition* 48, 4174-4179 (2009).

29. Medarova,Z., Pham,W., Farrar,C., Petkova,V., & Moore,A. In vivo imaging of siRNA delivery and silencing in tumors. *Nature Medicine* 13, 372-377 (2007).

30. Pradhan,P. *et al.* Targeted temperature sensitive magnetic liposomes for thermo-chemotherapy. *Journal of Controlled Release* 142, 108-121 (2010).

31. Alexiou,C. *et al.* Locoregional cancer treatment with magnetic drug targeting. *Cancer Research* 60, 6641-6648 (2000).

32. Nasongkla,N. *et al.* Multifunctional polymeric micelles as cancer-targeted, MRI-ultrasensitive drug delivery systems. *Nano Letters* 6, 2427-2430 (2006).

33. Jain,T.K. *et al.* Magnetic nanoparticles with dual functional properties: Drug delivery and magnetic resonance imaging. *Biomaterials* 29, 4012-4021 (2008).

34. Yu,M.K. *et al.* Drug-loaded superparamagnetic iron oxide nanoparticles for combined cancer imaging and therapy in vivo. *Angewandte Chemie-International Edition* 47, 5362-5365 (2008).

35. Martina,M.S. *et al.* Generation of superparamagnetic liposomes revealed as highly efficient MRI contrast agents for in vivo imaging. *Journal of the American Chemical Society* 127, 10676-10685 (2005).

36. Chengli,Y. *et al.* Nanoimmunoliposome delivery of superparamagnetic iron oxide markedly enhances targeting and uptake in human cancer cells in vitro and in vivo. Nanomedicine : the official journal of the American Academy of Nanomedicine 4[4], 318-329. 2008.
Ref Type: Abstract

37. Cheng,K., Peng,S., Xu,C.J., & Sun,S.H. Porous Hollow Fe3O4 Nanoparticles for Targeted Delivery and Controlled Release of Cisplatin. *Journal of the American Chemical Society* 131, 10637-10644 (2009).

38. Neuberger,T., Schopf,B., Hofmann,H., Hofmann,M., & von Rechenberg,B. Superparamagnetic nanoparticles for biomedical applications: Possibilities and limitations of a new drug delivery system. ***Journal of Magnetism and Magnetic Materials*** **293, 483-496 (2005).**

39. Ito,A., Shinkai,M., Honda,H., & Kobayashi,T. Medical application of functionalized magnetic nanoparticles. ***Journal of Bioscience and Bioengineering*** **100, 1-11 (2005).**

40. Tai,L.A. ***et al.*** **Thermosensitive liposomes entrapping iron oxide nanoparticles for controllable drug release.** ***Nanotechnology*** **20, (2009).**

41. Yuan,J.P., Guo,W.W., Yang,X.R., & Wang,E. Anticancer Drug-DNA Interactions Measured Using a Photoinduced Electron-Transfer Mechanism Based on Luminescent Quantum Dots. ***Analytical Chemistry*** **81, 362-368 (2009).**

42. Park,J.H., vonGÇàMaltzahn,G., Ruoslahti,E., Bhatia,S., & Sailor,M. Micellar Hybrid Nanoparticles for Simultaneous Magnetofluorescent Imaging and Drug Delivery. ***Angewandte Chemie International Edition*** **47, 7284-7288 (2008).**

43. Yezhelyev,M.V., Qi,L., OGÇÖRegan,R.M., Nie,S., & Gao,X. Proton-Sponge Coated Quantum Dots for siRNA Delivery and Intracellular Imaging. ***Journal of the American Chemical Society*** **130, 9006-9012 (2008).**

44. Derfus,A.M., Chen,A.A., Min,D.H., Ruoslahti,E., & Bhatia,S.N. Targeted Quantum Dot Conjugates for siRNA Delivery. ***Bioconjugate Chemistry*** **18, 1391-1396 (2007).**

45. Samia,A.C.S., Chen,X., & Burda,C. Semiconductor Quantum Dots for Photodynamic Therapy. ***Journal of the American Chemical Society*** **125, 15736-15737 (2003).**

46. Daniel,M.C. & Astruc,D. Gold Nanoparticles:GÇë Assembly, Supramolecular Chemistry, Quantum-Size-Related Properties, and Applications toward Biology, Catalysis, and Nanotechnology. ***Chemical Reviews*** **104, 293-346 (2003).**

47. Hu,M. ***et al.*** **Gold nanostructures: engineering their plasmonic properties for biomedical applications.** ***Chem. Soc. Rev.*** **35, 1084-1094 (2006).**

48. Murphy,C.J. ***et al.*** **Anisotropic Metal Nanoparticles:GÇë Synthesis, Assembly, and Optical Applications.** ***The Journal of Physical Chemistry B*** **109, 13857-13870 (2005).**

49. Wang,C., Hu,Y., Lieber,C.M., & Sun,S. Ultrathin Au Nanowires and Their Transport Properties. *Journal of the American Chemical Society* 130, 8902-8903 (2008).

50. Gibson,J.D., Khanal,B.P., & Zubarev,E.R. Paclitaxel-Functionalized Gold Nanoparticles. *Journal of the American Chemical Society* 129, 11653-11661 (2007).

51. Prabaharan,M., Grailer,J.J., Pilla,S., Steeber,D.A., & Gong,S. Gold nanoparticles with a monolayer of doxorubicin-conjugated amphiphilic block copolymer for tumor-targeted drug delivery. *Biomaterials* 30, 6065-6075 (2009).

52. Lu,W. *et al.* Tumor site-specific silencing of NF-kappaB p65 by targeted hollow gold nanosphere-mediated photothermal transfection. *Cancer Res.* 70, 3177-3188 (2010).

53. Chen,J. *et al.* Gold Nanocages as Photothermal Transducers for Cancer Treatment. *Small* 6, 811-817 (2010).

54. Lindner,J.R., Song,J., Jayaweera,A.R., Sklenar,J., & Kaul,S. Microvascular rheology of Definity microbubbles after intra-arterial and intravenous administration. *J. Am. Soc. Echocardiogr.* 15, 396-403 (2002).

55. Sirsi,S. & Borden,M. Microbubble Compositions, Properties and Biomedical Applications. *Bubble. Sci. Eng Technol.* 1, 3-17 (2009).

56. Sirsi,S. & Borden,M. Microbubble Compositions, Properties and Biomedical Applications. *Bubble. Sci. Eng Technol.* 1, 3-17 (2009).

57. Unger,E.C., McCreery,T.P., Sweitzer,R.H., Caldwell,V.E., & Wu,Y. Acoustically active lipospheres containing paclitaxel: a new therapeutic ultrasound contrast agent. *Invest Radiol.* 33, 886-892 (1998).

58. Tartis,M.S. *et al.* Therapeutic effects of paclitaxel-containing ultrasound contrast agents. *Ultrasound in Medicine & Biology* 32, 1771-1780 (2006).

59. Hettiarachchi,K., Zhang,S., Feingold,S., Lee,A.P., & Dayton,P.A. Controllable microfluidic synthesis of multiphase drug-carrying lipospheres for site-targeted therapy. *Biotechnol Progress* 25, 938-945 (2009).

60. Unger,E.C., Hersh,E., Vannan,M., Matsunaga,T.O., & McCreery,T. Local drug and gene delivery through microbubbles. *Prog. Cardiovasc. Dis.* 44, 45-54 (2001).

61. Unger,E.C. *et al.* Therapeutic applications of lipid-coated microbubbles. *Adv. Drug Deliv. Rev.* 56, 1291-1314 (2004).

62. Kheirolomoom,A. *et al.* Acoustically-active microbubbles conjugated to liposomes: Characterization of a proposed drug delivery vehicle. *Journal of Controlled Release* 118, 275-284 (2007).

63. Vandenbroucke,R.E., Lentacker,I., Demeester,J., De Smedt,S.C., & Sanders,N.N. Ultrasound assisted siRNA delivery using PEG-siPlex loaded microbubbles. *J. Control Release* 126, 265-273 (2008).

64. Seemann,S., Hauff,P., Schultze-Mosgau,M., Lehmann,C., & Reszka,R. Pharmaceutical evaluation of gas-filled microparticles as gene delivery system. *Pharm. Res.* 19, 250-257 (2002).

65. Hauff,P. *et al.* Evaluation of gas-filled microparticles and sonoporation as gene delivery system: feasibility study in rodent tumor models. *Radiology* 236, 572-578 (2005).

66. Lentacker,I. *et al.* Ultrasound-responsive polymer-coated microbubbles that bind and protect DNA. *Langmuir* 22, 7273-7278 (2006).

67. Christiansen,J.P., French,B.A., Klibanov,A.L., Kaul,S., & Lindner,J.R. Targeted tissue transfection with ultrasound destruction of plasmid-bearing cationic microbubbles. *Ultrasound Med. Biol.* 29, 1759-1767 (2003).

68. Haag,P. *et al.* Microbubble-enhanced ultrasound to deliver an antisense oligodeoxynucleotide targeting the human androgen receptor into prostate tumours. *J. Steroid Biochem. Mol. Biol.* 102, 103-113 (2006).

69. Teupe,C. *et al.* Vascular gene transfer of phosphomimetic endothelial nitric oxide synthase (S1177D) using ultrasound-enhanced destruction of plasmid-loaded microbubbles improves vasoreactivity. *Circulation* 105, 1104-1109 (2002).

70. Frenkel,P.A., Chen,S., Thai,T., Shohet,R.V., & Grayburn,P.A. DNA-loaded albumin microbubbles enhance ultrasound-mediated transfection in vitro. *Ultrasound Med. Biol.* 28, 817-822 (2002).

71. Bekeredjian,R., Chen,S., Grayburn,P.A., & Shohet,R.V. Augmentation of cardiac protein delivery using ultrasound targeted microbubble destruction. *Ultrasound Med. Biol.* 31, 687-691 (2005).

72. Kaneko,Y. *et al.* Use of a microbubble agent to increase the effects of high intensity focused ultrasound on liver tissue. *European Radiology* 15, 1415-1420 (2005).

73. Owens,D.E. & Peppas,N.A. Opsonization, biodistribution, and pharmacokinetics of polymeric nanoparticles. *International Journal of Pharmaceutics* 307, 93-102 (2006).

74. Minchinton,A.I. & Tannock,I.F. Drug penetration in solid tumours. *Nature Reviews Cancer* 6, 583-592 (2006).

75. Stern,S.T. & Mcneil,S.E. Nanotechnology safety concerns revisited. *Toxicological Sciences* 101, 4-21 (2008).

76. Vonarbourg,A., Passirani,C., Saulnier,P., & Benoit,J.P. Parameters influencing the stealthiness of colloidal drug delivery systems. *Biomaterials* 27, 4356-4373 (2006).

77. Luck,M., Paulke,B.R., Schroder,W., Blunk,T., & Muller,R.H. Analysis of plasma protein adsorption on polymeric nanoparticles with different surface characteristics. *Journal of Biomedical Materials Research* 39, 478-485 (1998).

78. Klibanov,A.L., Maruyama,K., Torchilin,V.P., & Huang,L. Amphipathic polyethyleneglycols effectively prolong the circulation time of liposomes. *FEBS Lett.* 268, 235-237 (1990).

79. Senior,J., Delgado,C., Fisher,D., Tilcock,C., & Gregoriadis,G. Influence of surface hydrophilicity of liposomes on their interaction with plasma protein and clearance from the circulation: studies with poly(ethylene glycol)-coated vesicles. *Biochim. Biophys. Acta* 1062, 77-82 (1991).

80. Smith,A.M. & Nie,S. Minimizing the hydrodynamic size of quantum dots with multifunctional multidentate polymer ligands. *Journal of the American Chemical Society* 130, 11278-+ (2008).

81. Nie,S.M. Understanding and overcoming major barriers in cancer nanomedicine. *Nanomedicine* 5, 523-528 (2010).

82. McCarthy,J.R. The future of theranostic nanoagents. *Nanomedicine* 4, 693-695 (2009).

83. McCarthy,J.R. The future of theranostic nanoagents. *Nanomedicine* 4, 693-695 (2009).

84. McCarthy,J.R. & Weissleder,R. Multifunctional magnetic nanoparticles for targeted imaging and therapy. *Adv. Drug Deliv. Rev.* 60, 1241-1251 (2008).

85. Kuhl,C. *et al.* Prospective multicenter cohort study to refine management recommendations for women at elevated familial risk of breast cancer: the EVA trial. *J. Clin. Oncol.* 28, 1450-1457 (2010).

86. Schellinger,P.D., Meinck,H.M., & Thron,A. Diagnostic accuracy of MRI compared to CCT in patients with brain metastases. *J. Neurooncol.* 44, 275-281 (1999).

87. Pitton,M.B. *et al.* MRI versus 64-row MDCT for diagnosis of hepatocellular carcinoma. *World J. Gastroenterol.* 15, 6044-6051 (2009).

88. Bonnemain,B. Superparamagnetic agents in magnetic resonance imaging: physicochemical characteristics and clinical applications. A review. *J. Drug Target* 6, 167-174 (1998).

89. Bradbury,M. & Hricak,H. Molecular MR imaging in oncology. *Magn Reson. Imaging Clin. N. Am.* 13, 225-240 (2005).

90. Funovics,M.A. *et al.* MR imaging of the her2/neu and 9.2.27 tumor antigens using immunospecific contrast agents. *Magn Reson. Imaging* 22, 843-850 (2004).

91. Harisinghani,M.G. *et al.* Noninvasive detection of clinically occult lymph-node metastases in prostate cancer. *N. Engl. J. Med.* 348, 2491-2499 (2003).

92. Montet,X., Montet-Abou,K., Reynolds,F., Weissleder,R., & Josephson,L. Nanoparticle imaging of integrins on tumor cells. *Neoplasia.* 8, 214-222 (2006).

93. LaConte,L., Nitin,N., & Bao,G. Magnetic nanoparticle probes. *Materials Today* 8, 32-38 (2005).

94. Wang,Y.X., Hussain,S.M., & Krestin,G.P. Superparamagnetic iron oxide contrast agents: physicochemical characteristics and applications in MR imaging. *Eur. Radiol.* 11, 2319-2331 (2001).

95. Casadei,M.A. *et al.* Solid lipid nanoparticles incorporated in dextran hydrogels: a new drug delivery system for oral formulations. *Int. J. Pharm.* 325, 140-146 (2006).

96. Kim,I.S., Jeong,Y.I., & Kim,S.H. Self-assembled hydrogel nanoparticles composed of dextran and poly(ethylene glycol) macromer. *Int. J. Pharm.* 205, 109-116 (2000).

97. Lopez,E., O'Brien,D.F., & Whitesides,T.H. Effects of membrane composition and lipid structure on the photopolymerization of lipid diacetylenes in bilayer membranes. *Biochim. Biophys. Acta* 693, 437-443 (1982).

98. O'Brien,D.F., Klingbiel,R.T., Specht,D.P., & Tyminski,P.N. Preparation and characterization of polymerized liposomes. *Ann. N. Y. Acad. Sci.* 446, 282-295 (1985).

99. Lasic,D.D. *Liposomes in gene delivery*(CRC Press, Boca Raton, FL, 1997).

100. Rohrer,M., Bauer,H., Mintorovitch,J., Requardt,M., & Weinmann,H.J. Comparison of magnetic properties of MRI contrast media solutions at different magnetic field strengths. *Investigative Radiology* 40, 715-724 (2005).

101. Wei,K. & Kaul,S. Recent advances in myocardial contrast echocardiography. *Curr. Opin. Cardiol.* 12, 539-546 (1997).

102. Forsberg,F., Liu,J.B., Merton,D.A., Rawool,N.M., & Goldberg,B.B. Parenchymal enhancement and tumor visualization using a new sonographic contrast agent. *J. Ultrasound Med.* 14, 949-957 (1995).

103. Blomley,M.J., Cooke,J.C., Unger,E.C., Monaghan,M.J., & Cosgrove,D.O. Microbubble contrast agents: a new era in ultrasound. *BMJ* 322, 1222-1225 (2001).

104. Apfel,R.E. & Holland,C.K. Gauging the likelihood of cavitation from short-pulse, low-duty cycle diagnostic ultrasound. *Ultrasound Med. Biol.* 17, 179-185 (1991).

105. Madanshetty,S.I., Roy,R.A., & Apfel,R.E. Acoustic microcavitation: its active and passive acoustic detection. *J. Acoust. Soc. Am.* 90, 1515-1526 (1991).

106. Price,R.J., Skyba,D.M., Kaul,S., & Skalak,T.C. Delivery of colloidal particles and red blood cells to tissue through microvessel ruptures created by targeted microbubble destruction with ultrasound. *Circulation* 98, 1264-1267 (1998).

107. Jain,R.K. Delivery of molecular medicine to solid tumors: lessons from in vivo imaging of gene expression and function. *J. Control Release* 74, 7-25 (2001).

108. Schutt,E.G., Klein,D.H., Mattrey,R.M., & Riess,J.G. Injectable microbubbles as contrast agents for diagnostic ultrasound imaging: the key role of perfluorochemicals. *Angew. Chem. Int. Ed Engl.* 42, 3218-3235 (2003).

109. Stride,E. & Edirisinghe,M. Novel microbubble preparation technologies. *Soft Matter* 4, 2350-2359 (2008).

110. Stride,E. & Edirisinghe,M. Novel preparation techniques for controlling microbubble uniformity: a comparison. *Medical & Biological Engineering & Computing* 47, 883-892 (2009).

111. Garstecki,P., Fuerstman,M.J., Stone,H.A., & Whitesides,G.M. Formation of droplets and bubbles in a microfluidic T-junction - scaling and mechanism of break-up (vol 6, pg 437, 2006). *Lab on A Chip* 6, 693 (2006).

112. Nisisako,T., Torii,T., & Higuchi,T. Droplet formation in a microchannel network. *Lab Chip* 2, 24-26 (2002).

113. Thorsen,T., Roberts,R.W., Arnold,F.H., & Quake,S.R. Dynamic pattern formation in a vesicle-generating microfluidic device. *Phys. Rev. Lett.* 86, 4163-4166 (2001).

114. Garstecki,P. *et al.* Formation of monodisperse bubbles in a microfluidic flow-focusing device. *Applied Physics Letters* 85, 2649-2651 (2004).

115. Hettiarachchi,K., Talu,E., Longo,M.L., Dayton,P.A., & Lee,A.P. On-chip generation of microbubbles as a practical technology for manufacturing contrast agents for ultrasonic imaging. *Lab on A Chip* 7, 463-468 (2007).

116. Xia,Y.N. & Whitesides,G.M. Soft lithography. *Annual Review of Materials Science* 28, 153-184 (1998).

117. Weibel,D.B., DiLuzio,W.R., & Whitesides,G.M. Microfabrication meets microbiology. *Nature Reviews Microbiology* 5, 209-218 (2007).

118. Lindroos,V. Handbook of silicon based MEMS materials and technologies. 1st ed, (2010).

119. Andersson,H., van der Wijngaart,W., Enoksson,P., & Stemme,G. Micromachined flow-through filter-chamber for chemical reactions on beads. *Sensors and Actuators B-Chemical* 67, 203-208 (2000).

120. Dussart,R. *et al.* Passivation mechanisms in cryogenic SF6/O-2 etching process. *Journal of Micromechanics and Microengineering* 14, 190-196 (2004).

121. Mellhaoui,X. *et al.* SiOxFy passivation layer in silicon cryoetching. *Journal of Applied Physics* 98, (2005).

122. Suni,N.M. *et al.* Selective surface patterning with an electric discharge in the fabrication of microfluidic structures. *Angew. Chem. Int. Ed Engl.* 47, 7442-7445 (2008).

123. Ferrara,K.W., Borden,M.A., & Zhang,H. Lipid-shelled vehicles: engineering for ultrasound molecular imaging and drug delivery. *Acc. Chem. Res.* 42, 881-892 (2009).

124. SANDISON,J.C. A New Method for the Microscopic Study of Living Growing Tissues by the Introduction of a Transparent Chamber in the Rabbit's Ear. *The American Journal of the Medical Sciences* 174, (1927).

125. Algire,G.H. An adaptation of the transparent chamber technique to the mouse. *Journal of the National Cancer Institute* 4, 1-11 (1943).

126. Goodall,C.M., Feldman,R., Sanders,A.G., & Shubik,P. Vascular Patterns of 4 Transplantable Tumors in Hamster (Meso Cricetus Auratus). *Angiology* 16, 622-& (1965).

127. Endrich,B., Asaishi,K., Gotz,A., & Messmer,K. Technical report--a new chamber technique for microvascular studies in unanesthetized hamsters. *Res. Exp. Med. (Berl)* 177, 125-134 (1980).

128. Hobbs,J.B., Chusilp,S., Hua,A., Kincaid-Smith,P., & McIver,M.A. The pathogenesis of hypertensive vascular changes in the rat: microscopic and ultrastructural correlation in vivo. *Clin. Sci. Mol. Med. Suppl* 3, 73s-75s (1976).

129. Arfors,K.E., Jonsson,J.A., & McKenzie,F.N. A titanium rabbit ear chamber: assembly, insertion and results. *Microvasc. Res.* 2, 516-518 (1970).

130. Branemark,P.I., Breine,U., & Aspegren,K. Microcirculatory Studies in Man by High Resolution Vital Microscopy. *Angiology* 15, 329-& (1964).

131. Lehr,H.A., Leunig,M., Menger,M.D., Nolte,D., & Messmer,K. Dorsal skinfold chamber technique for intravital microscopy in nude mice. *Am. J. Pathol.* 143, 1055-1062 (1993).

132. Huang,Q. *et al.* Noninvasive visualization of tumors in rodent dorsal skin window chambers. *Nat. Biotechnol.* 17, 1033-1035 (1999).

133. Padhani,A.R. Dynamic contrast-enhanced MRI in clinical oncology: current status and future directions. *J. Magn Reson. Imaging* 16, 407-422 (2002).

134. Yamaura,H., Suzuki,M., & Sato,H. Transparent Chamber in Rat Skin for Studies on Microcirculation in Cancer Tissue. *Gann* 62, 177-& (1971).

135. Papenfuss,H.D., Gross,J.F., Intaglietta,M., & Treese,F.A. A transparent access chamber for the rat dorsal skin fold. *Microvasc. Res.* 18, 311-318 (1979).

136. Makale,M. Intravital imaging and cell invasion. *Methods Enzymol.* 426, 375-401 (2007).

137. Menger,M.D., Jager,S., Walter,P., Hammersen,F., & Messmer,K. A novel technique for studies on the microvasculature of transplanted islets of Langerhans in vivo. *Int. J. Microcirc. Clin. Exp.* 9, 103-117 (1990).

138. Menger,M.D., Laschke,M.W., & Vollmar,B. Viewing the microcirculation through the window: some twenty years experience with the hamster dorsal skinfold chamber. *Eur. Surg. Res.* 34, 83-91 (2002).

139. Dupont Product and Properties Guide - Delrin. 2010. Ref Type: Online Source

140. RTI International Metals Inc. Titanium Alloy Guide. 2010. Ref Type: Online Source

141. ASM Material Data Sheet- Aluminum. 2010. Ref Type: Online Source

142. Leunig,M. & Messmer,K. Skin Fold Chamber Models in *Tumor angiogenesis and microcirculation* 143-154 2001).

143. Makale,M.T. *et al.* Tissue window chamber system for validation of implanted oxygen sensors. *Am. J. Physiol Heart Circ. Physiol* 284, H2288-H2294 (2003).

144. Katz,M.H. *et al.* Selective antimetastatic activity of cytosine analog CS-682 in a red fluorescent protein orthotopic model of pancreatic cancer. *Cancer Res.* 63, 5521-5525 (2003).

145. Katz,M.H. *et al.* A novel red fluorescent protein orthotopic pancreatic cancer model for the preclinical evaluation of chemotherapeutics. *J. Surg. Res.* 113, 151-160 (2003).

146. Ferrari,M. Cancer nanotechnology: opportunities and challenges. *Nat. Rev. Cancer* 5, 161-171 (2005).

147. Peer,D. *et al.* Nanocarriers as an emerging platform for cancer therapy. *Nat. Nanotechnol.* 2, 751-760 (2007).

148. Weissleder,R. & Pittet,M.J. Imaging in the era of molecular oncology. *Nature* 452, 580-589 (2008).

149. Worthington,B.S. *Magnetic Resonance Imaging*(John Wiley & Sons, Ltd,2001).

150. Hawkes,R.C., Holland,G.N., Moore,W.S., & Worthington,B.S. Nuclear magnetic resonance (NMR) tomography of the brain: a preliminary clinical assessment with demonstration of pathology. *J. Comput. Assist. Tomogr.* 4, 577-586 (1980).

151. Wikipedia: Peter Mansfield. 2010. Ref Type: Online Source

152. MRI: A guided tour. 2010. Ref Type: Online Source

153. Molecular Expressions: Marvin Lee Minsky. 2010. Ref Type: Online Source

154. Confocal Microscopy. 2010. Ref Type: Online Source

155. Nakano,A. Spinning-disk confocal microscopy -- a cutting-edge tool for imaging of membrane traffic. *Cell Struct. Funct.* 27, 349-355 (2002).

156. Multiphoton Microscopy. 2010. Ref Type: Online Source

157. Kaiser,W. & Garrett,C.G.B. 2-Photon Excitation in Caf2 - Eu2+. *Physical Review Letters* 7, 229-& (1961).

158. Sheppard,C.J.R. & Kompfner,R. Resonant Scanning Optical Microscope. *Applied Optics* 17, 2879-2882 (1978).

159. Denk,W., Strickler,J.H., & Webb,W.W. 2-Photon Laser Scanning Fluorescence Microscopy. *Science* 248, 73-76 (1990).

160. Wikipedia: Two-photon Excitation Microscopy. 2010. Ref Type: Online Source

161. So,P.T. *Two-photon Fluorescence Light Microscopy*(John Wiley & Sons, Ltd,2001).

162. Garber,K. Realistic rodents? Debate grows over new mouse models of cancer. *J. Natl. Cancer Inst.* 98, 1176-1178 (2006).